

**Structure, morphology, thermodynamic stability and properties of  
isotactic polypropylene with nodular nano-domains**

**Dissertation**

**zur Erlangung des akademischen Grades  
Doktor-Ingenieur (Dr. -Ing.)**

**genehmigt durch das  
Zentrum für Ingenieurwissenschaften  
der Martin-Luther-Universität Halle-Wittenberg**

**von**

**Herrn M. Sc. -Ing. Qamer Zia  
Geboren am 10.12.1978 in D.G. Khan–Pakistan**

**Gutachter**

- 1. Prof. Dr. -Ing. habil. Hans-Joachim Radsch**
- 2. Prof. Dr. rer. nat. habil. Christoph Schick**

**Tag der Verteidigung 18.12.2009**

## ***Acknowledgements***

*I deem it a rare privilege and pleasure to express my cordial gratitude to my supervisors, Prof. Dr. H.-J. Radusch and PD Dr. R. Androsch for their enthusiastic and keen interest throughout my thesis work. I am greatly thankful to them for their continued support to visit several conferences and institutes. I further extend my special thanks to PD Dr. R. Androsch for his persistent guidance, invaluable suggestions and skilled advices. He is a great teacher, who has helped me to develop in various disciplines.*

*I deeply acknowledge the help and support of Prof. S. Piccarolo and his group, at the University of Palermo (Italy), in preparation of samples, density measurement, and also for making my stay in Palermo possible.*

*I pay my sincere thanks to Dr. A. Wutzler for his kind assistance in the use of various instruments and for his suggestions to improve the discussion of results, and to Dr. I. Kolesov for his help to perform DMA tests and for the discussion of results.*

*I specially thank Dr. E. Ingolič at the Graz University of Technology (Austria) for providing TEM-images.*

*I appreciate the assistance of Dr. J. K. Hobbs and Dr. K. Lekshmi, at the University of Sheffield (United Kingdom), to perform in situ AFM experiments.*

*I thank Ms. C. Seidel and Dr. M. Dubiel at the Martin-Luther-University Halle-Wittenberg for their assistance to perform UV/VIS measurements.*

*I express my deep gratitude to the friendly and loving behavior of all my colleagues.*

*I thank my family for their untiring support and encouragement throughout my thesis.*

## Contents

<b>1.</b>	<b>Introduction</b>	<b>1</b>
<b>2.</b>	<b>Structure and morphology formation of semicrystalline polymers</b>	<b>3</b>
2.1.	Crystal nucleation and growth	3
2.2.	Conditions of formation of structure and morphology	6
2.3.	Isotactic polypropylene	14
2.3.1.	Crystal polymorphs of isotactic polypropylene: The $\alpha$ -, $\beta$ - and $\gamma$ -forms	15
2.3.2.	Mesomorphic isotactic polypropylene	20
<b>3.</b>	<b>Properties of semicrystalline polymers in relation to structure, morphology and crystallization conditions</b>	<b>26</b>
<b>4.</b>	<b>Material and instrumentation</b>	<b>37</b>
4.1.	Material	37
4.2.	Cooling device and sample preparation	37
4.3.	Instrumentation	38
<b>5.</b>	<b>Structure and morphology formation on melt-crystallization</b>	<b>42</b>
5.1.	Density and X-ray structure	42
5.2.	Crystal morphology and superstructure	43
<b>6.</b>	<b>Thermodynamic stability of lamellar and nodular crystals</b>	<b>49</b>
6.1.	Mesomorphic-to-monoclinic phase transition	49
6.2.	Reorganization of crystal morphology	55
6.3.	Crystal morphology and phase fractions	62
6.4.	Annealing kinetics – correlation of AFM and DSC data	63
6.5.	Thermodynamic stability of nodular crystals	69
<b>7.</b>	<b>Structure – property relations</b>	<b>73</b>
7.1.	Thermal and dynamic-mechanical properties	73

7.1.1.	Effect of crystallinity and crystal morphology on rigid amorphous fraction	73
7.1.2.	Effect of crystal morphology and phase fractions on the mobility of mobile amorphous fraction	77
7.1.3.	Effect of crystallinity and crystal morphology on dynamic-mechanical behavior	79
7.2.	Mechanical properties	84
7.2.1.	Effect of crystal morphology and crystallinity on tensile deformation	84
7.2.2.	In situ atomic force microscopy observations of the deformation behavior	85
7.2.3.	Effect of crystal morphology and density on modulus of elasticity and yield stress	89
7.3.	Effect of structure at micrometer and nanometer scale on light transmission	94
<b>8.</b>	<b>Nodular morphology – A general phenomenon in semicrystalline polymers</b>	<b>100</b>
<b>9.</b>	<b>Summary</b>	<b>103</b>
	<b>Symbols and abbreviations</b>	<b>106</b>
	<b>References</b>	<b>107</b>

## 1. Introduction

Isotactic polypropylene (iPP) is a polymorphic semicrystalline homopolymer. The importance of iPP as a commodity thermoplastic is its wide area of applications, particularly in the fields of packaging, automotive and household products. The low cost, favorable properties and ability to be processed by most industrial methods, like injection molding, blow molding and extrusion, contribute to its increasing demand [1].

iPP can crystallize into monoclinic  $\alpha$ -structure, hexagonal  $\beta$ -structure, triclinic  $\gamma$ -structure and a mesomorphic structure. The macromolecules, in all of these forms, adopt a  $3_1$ -helical conformation. Formation of different polymorphic forms can be controlled by the conditions of crystallization and/or by the addition of special nucleating agents. In detail, slow cooling of the quiescent melt allows the formation of monoclinic  $\alpha$ -structure, whereas the presence of special nucleating agents or crystallization at high pressure produces hexagonal  $\beta$ -structure or triclinic  $\gamma$ -structure, respectively. The mesomorphic form of iPP can be obtained either by rapid melt-crystallization or by the crystallization from the glassy state [2-4]. The characteristic feature of the mesomorphic form of iPP is the formation of non-lamellar domains, whereas  $\alpha$ ,  $\beta$  and  $\gamma$  polymorphs are related to the typical lamellar crystal morphology. The structure and morphology of iPP obtained as a function of the conditions of crystallization can be further modified by annealing. In summary, a range of crystal structures and morphologies of iPP can be obtained by the variation of the conditions of crystallization and annealing, which, in turn, allow to control the properties in a wide range. In this respect the mesomorphic form of iPP is of great practical importance, since high cooling rates favor its formation in a variety of industrial processes, such as injection molding, blow molding and cast-film production.

The formation of mesomorphic nodules, in contrast to monoclinic lamellae, is expected to yield a highly constrained interface between the crystal and the amorphous regions of iPP. This can lead to the restriction of the mobility of the amorphous part of iPP, thus the properties. This effect has been reported for a number of semicrystalline polymers, such as poly(ethylene terephthalate) (PET) [5,6] and isotactic polybutene (iPB) [7]. Furthermore, the absence of lamellae and spherulites in a mesomorphic iPP may result in optical and mechanical performance that is superior in comparison to iPP with lamellae forming spherulites. This work is an attempt to give this well studied polymer a new scientific dimension by replacing lamellae with nodular nano-domains. In this

respect, it is important to analyze the changes in properties of an initially quenched, mesomorphic iPP from the point-of-view of a systematic tailoring of the crystal structure and morphology, by the conditions of annealing. This idea is further extended to other semicrystalline polymers, which show a likelihood of the formation of non-lamellar domains, in order to broaden the field of research of semicrystalline polymers.

This thesis is oriented in a direction to make progress in the fundamental research of semicrystalline iPP with nodular nano-domains. As a prerequisite, it requires a thorough understanding of the formation and reorganization of the structure and morphology of iPP, as result of the conditions of primary melt-crystallization and subsequent annealing. Primary intention of this work is to establish the structure/morphology-property relations of iPP with nodular nano-domains, which, in applications, where an optimum combination of the thermal, mechanical and optical properties is required, can provide an innovative solution. In this study, the structure and morphology of 100  $\mu\text{m}$  thick films of iPP are adjusted by controlled cooling of the melt between  $10^{-1}$  and  $10^3$   $\text{K s}^{-1}$ . Further modification of the structure and morphology was made by the conditions of subsequent annealing. In the next step, selected thermal, mechanical and optical properties, of melt-crystallized and subsequently annealed iPP, are characterized. Finally, a direct effect of the structure and morphology on these properties is analyzed, in order to identify the possible advantages and applications of iPP containing nodular nano-domains in an amorphous structure.

## 2. Structure and morphology formation of semicrystalline polymers

### 2.1. Crystal nucleation and growth

#### *Homogeneous and heterogeneous nucleation*

Polymer crystallization is a transition process in which an ordered phase, i.e., crystal, is formed from a disordered phase, i.e., melt. Crystallization from the quiescent-melt starts at a certain degree of supercooling ( $\Delta T_u$ ), i.e., temperature difference between the equilibrium melting temperature ( $T_m^o$ ) and the crystallization temperature ( $T_c$ ), and is expressed by the following equation [8,9]:

$$\Delta T_u = T_m^o - T_c \quad (1)$$

Homogeneous nucleation occurs by the spontaneous aggregation of polymer chain segments, without involving a pre-existing foreign surface. The first step is the formation of a nucleus, which in its early stages is called an embryo. If a cylindrical shape of an embryo is considered in the melt then the free energy difference between the embryo and the melt can be written as follows:

$$\Delta G_{(v,l)} = -lav\Delta G_v + 2av\sigma_e + Cl\sqrt{av}\sigma_s \quad (2)$$

where  $\sigma_e$  and  $\sigma_s$  are the surface free energies of the top and side plane of embryo, respectively. Number of segments, length of a segment and the cross-sectional area are represented by  $v$ ,  $l$  and  $a$ , respectively. The term  $\Delta G_v$  represents the bulk free enthalpy of crystallization and  $C$  is a constant that represents  $2\sqrt{\pi}$  for a circular cross-section and 4 for a square cross-section [10]. The size of an embryo increases, with the increase of its free energy, until the volume-to-surface ratio becomes large enough that the driving force term  $-lav\Delta G_v$ , favoring the growth of an embryo, dominates the surface terms, favoring the re-dissolution of an embryo. In this case, the embryo becomes a stable nucleus and grows spontaneously [10,11].

The free energy barrier for an embryo to become a stable nucleus can be determined from equation 3, where  $\Delta h_f$  represents the bulk heat of fusion:

$$\Delta G^* = \frac{2(C\sigma_s)^2 \sigma_e (T_m^o)^2}{\Delta h_f^2 (T_m^o - T_c)^2} \quad (3)$$

Heterogeneous nucleation process occurs in presence of existing surfaces, e.g., nucleating agents, which reduce the free enthalpy barrier to form a stable nucleus. Melt-crystallization usually occurs at low supercooling, suggesting that mostly crystallization of macromolecules is the result of heterogeneous nucleation [11].

### ***Primary and secondary crystallization***

Primary crystallization is the first stage of crystallization and can be associated with the undisturbed radial growth of spherulites. In general, it requires supercooling of the isotropic melt, where the crystallization starts by nucleation and growth. Spherulites grow until impingement with other growing spherulites. The process of primary crystallization can be followed by measuring the growth of a spherulite with time, using optical microscopy. During the crystallization process the fractional crystallinity ( $\varphi$ ) increases with time ( $t$ ), which can be approximated by the Avrami equation:

$$\varphi = 1 - \exp(-kt^n) \quad (4)$$

where  $k$  is a growth rate parameter and  $n$  is a nucleation index [12]. Primary crystallization mainly occurs by the lateral growth of crystals, since the growth in chain direction is restricted by the presence of folds and entanglements at the surfaces of a crystal. The growth front moves in lateral direction by the attachment of chain segments at the growth front, with favorable conformation over a length corresponding to the crystal thickness [9]. The growth rate of spherulites is the average growth rate of all radially growing lamellae and is constant at a constant  $T_c$  or  $\Delta T_u$ . The growth rate can be determined over a large range of  $T_c$  or  $\Delta T_u$  and shows a bell-shaped curve, as shown in Figure 1. The maximum rate of spherulitic growth is obtained at an intermediate crystallization temperature between the glass transition temperature ( $T_g$ ) and  $T_m^o$ , where a maximum balance is reached between the chain mobility and the crystal growth. Choosing the crystallization temperature off the peak maximum decreases the spherulitic

growth rate, which approaches to zero at glass transition temperature, due to restricted chain mobility, or at  $T_m^o$ , where the nuclei are destroyed as soon as they are formed.

In case, if the crystallization occurs under high nucleation/growth ratios, the polymer develops small spherulites, whereas a low nucleation/growth ratio generates large spherulites. The temperature at which the maximum growth rate is observed does not depend on the molecular weight, but the maximum crystallization rate decreases with increasing the molecular weight [12,13].

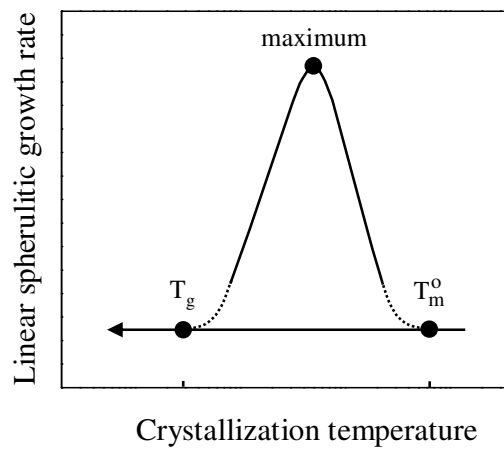


**Figure 1.** Linear spherulitic growth rate as a function of the temperature of crystallization [12,13].

The growth rate data for semicrystalline polymers can be represented as a function of supercooling by using the Vogel–Fulcher equation. The dependence of radial growth rate ( $u$ ) on  $\Delta T_u$  is expressed by the following equation:

$$u \propto \exp \frac{T_A}{T_c - T_v} \exp \frac{B_o}{T_m^o - T_c} \quad (5)$$

where  $T_A$  and  $T_v$  are the activation temperature with typical values in the order of 1000–2000 K and Vogel-temperature related to the glass transition temperature, respectively.

The secondary crystallization involves all processes that lead to an increase of crystallinity ( $X_c$ ), after the primary crystallization process is completed [9,11]. Analysis of the change of crystallinity with time, at a certain degree of supercooling, results in a

sigmoidal shaped curve, in the stage of primary crystallization. The crystallinity, after the primary crystallization process is completed, continues to increase with increasing the time of isothermal crystallization [14] and, in some cases, also during cooling from the temperature of isothermal crystallization, involving a process of secondary crystallization. For instance, in case of low-density polyethylene (LDPE) with 3 % of short-chain branches, primary crystallization yielded only 15 % of crystallinity, which increased to more than three-times during cooling. Similarly, the crystallinity can also increase on annealing by secondary crystallization, which is true for almost all semicrystalline polymers, depending on the history of crystallization [9,11]. The increase of crystallinity after the completion of primary crystallization process, in general, can be separated into at least two processes. There is crystallization of amorphous material, and secondly there is perfection of poorly crystallized macromolecules [11]. The major irreversible phenomenon on heating a solid, semicrystalline polymer is the increase of the thickness of crystals. Different mechanisms are suggested for the increase of crystal thickness, (a) local melting/formation of a less dense metastable phase followed by the readjustment of chains, (b) formation and movement of conformational defects, which transfer the chain segments across the crystal boundary into the liquid phase, and (c) transfer of material from the amorphous phase to the crystalline phase [10].

## **2.2. Conditions of formation of structure and morphology**

### ***Molecular macro-conformation and morphology***

The crystal structure and morphology of semicrystalline polymers can be controlled in a wide range to produce polymeric materials with specific properties. Tailoring the properties of a semicrystalline polymer requires knowledge of controlling the parameters like crystal structure and morphology.

The crystallizing polymer chains adopt a minimum-energy conformation, called the macro-conformation. Based on the proposed models of polymer crystallization, different macro-conformations of polymer chains are possible, as are summarized in Figure 2. In the melt and glassy state, polymer chains are highly disordered and adopt the macro-conformation of a random coil (A). Formation of folded-chain crystals involve a lower positive free-enthalpy barrier to crystallization and are obtained on crystallization from the quiescent melt or from the solution (B). In an extended-chain crystal, macromolecules

are fully stretched over the entire length of a crystal and regularly placed adjacent to each other (C). Crystals with intermediate macro-conformations are entitled as fringed-micelle, where the macromolecules are frequently entering and leaving the crystal basal planes (D) [8].

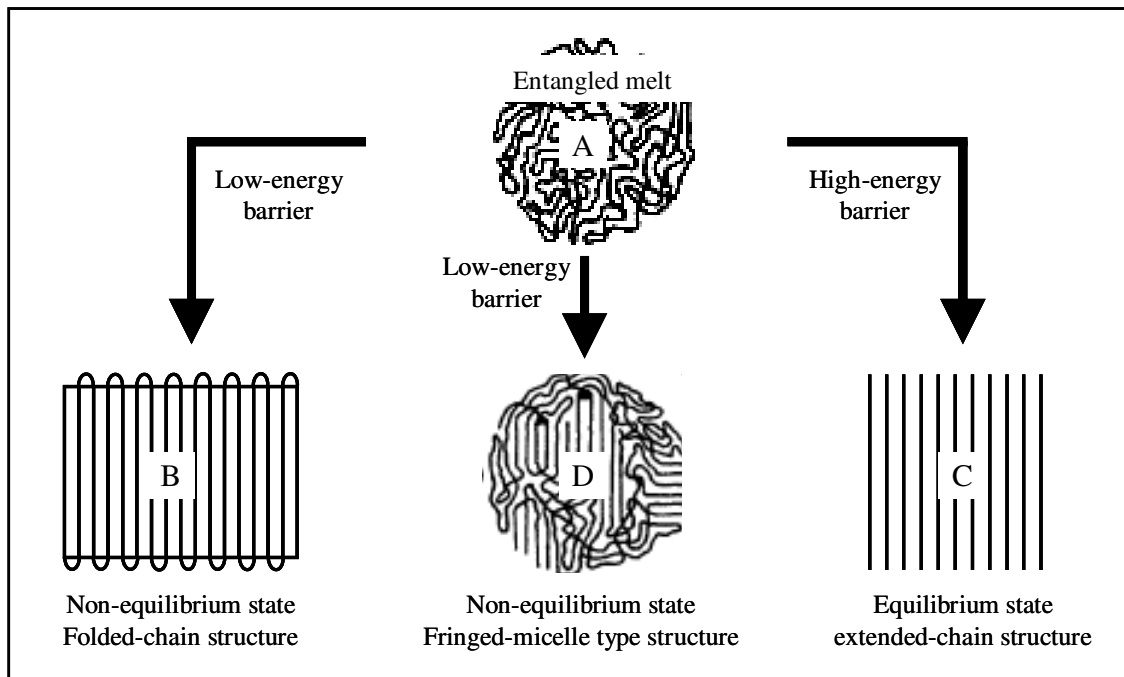


**Figure 2.** Possible macro-conformations of polymer chains [8].

Fringed-micelle description assumed the semicrystalline polymers, a two-phase system, comprising an amorphous phase and a crystalline phase. It was suggested that the segments of polymer chains are precisely aligned over distances corresponding to the size of crystallite and an individual macromolecule contributes to several crystallites through the amorphous region. Figure 3a illustrates an atomic force microscope (AFM) image of the fringed-micelle type crystals of cellulose. The size of crystals is about 100–500 nm in length and about 30-60 nm in width. Fundamentally, the formation of fringed-micelle structure is not expected to exist in highly crystalline polymers, however, with suitable modifications, e.g., by adding the possibility of chain-folds, as illustrated in Figure 2(D), all three limiting macro-conformations are combined, which can be helpful for the description of structure and morphology of semicrystalline polymers [8,15-18]. The

formation of extended-chain crystals in semicrystalline polymers, such as low and ultra-high molecular weight PE, is possible on crystallization at high temperature and pressure. Figure 3b shows a transmission electron microscope (TEM) image of extended-chain crystals of PE obtained at a temperature and pressure of 493 K and 480 MPa, respectively. The chains are extended in the direction of striations [8,17]. In addition to producing the extended-chain crystals, polymers generally crystallize, either from the melt or from the solution, in the form of folded-chain lamellar crystals. The fact that the chains are folded was established about half a century ago based on the observation that the length of extended polymer chain is much larger than the observed thickness of lamellar crystals. Electron diffraction measurements indicated that the polymer chains are oriented normal to the plane of lamellae. Figure 3c shows the folded-chain lamellar crystals of PE, isothermally melt-crystallized at 397.8 K for 3 hours [19].

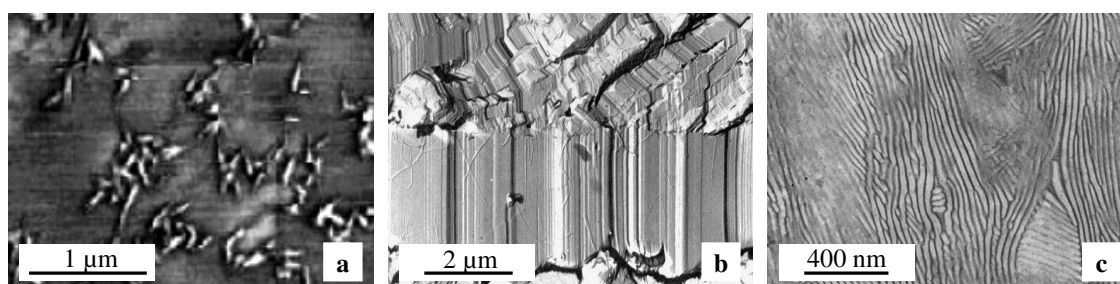


**Figure 3.** (a) AFM-image of fringed-micelle type structure of cellulose [15] and TEM-images of (b) extended-chain [8] and (c) folded-chain lamellar crystals of PE [19].

One of the important issues of the folded-chain crystals is the understanding of possible chain re-entry into the crystal. The regular and adjacent chain folding with immediate re-entry is more favorable in case of polymer single crystals. A considerable molecular disorder exists at the fold surface on melt-crystallization, especially at large  $\Delta T_u$ , which affects the final properties of semicrystalline polymers [5-7,20].

### ***Lamellar and non-lamellar crystal morphology***

Lamellar crystals are observed in almost all crystallizable polymers. The thickness of lamellae strongly depend on the conditions of primary melt-crystallization and

increases with increasing the temperature of crystallization [8,9]. Figure 4a shows the TEM-image of lamellar crystals of thickness of about 23.5 nm, obtained in a sharp fraction of linear PE after isothermal melt-crystallization at a temperature of 397.8 K for 3 hours. The thickness of lamellae was increased to 32 nm on increasing the temperature of isothermal crystallization to 401.3 K and the crystallization time to 65 hours [19]. In addition to the formation of lamellar crystals, semicrystalline polymers can also crystallize, exclusively, into non-lamellar crystals with fringe-micelle type structure, at large  $\Delta T_u$ . Initial observations raised doubts on the existence of nodular morphology [21]. At first, these nodules were considered as representation of the local order existing in the amorphous phase. This idea was not supported by the analysis of small-angle X-ray scattering (SAXS) and small angle neutron scattering (SANS) techniques. Furthermore, it was suggested that such granular appearance could be caused by the defocus fringes in TEM, however, it was later shown that the size of nodules is much larger than the defocus fringes [22]. Later studies confirmed the existence of nodular crystal morphology in several semicrystalline polymers including PE [23], iPP [2], iPB [24], poly(vinylidene fluoride) (PVDF) [25], PET [26], isotactic polystyrene (iPS) and isotactic poly(methyl methacrylate) (iPMMA) [27].

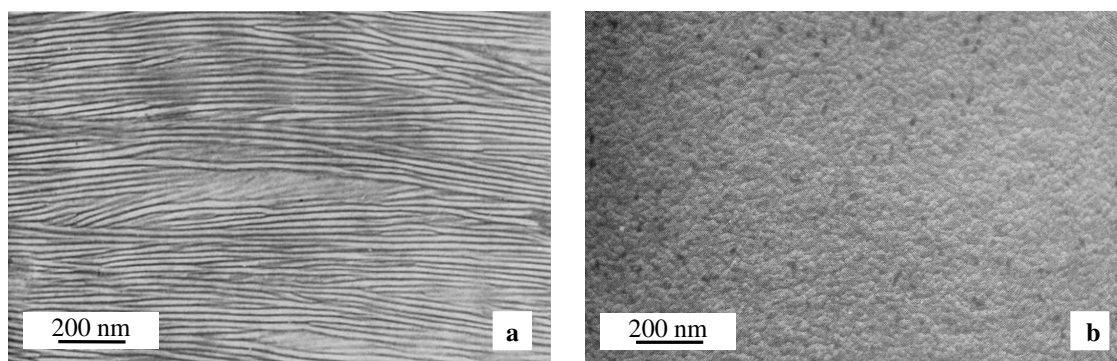


**Figure 4.** (a) Lamellar [19] and (b) nodular [23] crystal morphology of melt-crystallized and glass-crystallized and subsequently annealed PE, respectively.

Further evidence of the existence of nodular domains was provided by annealing experiments. Analysis of an ultra-quenched film of PE of thickness of less than 100 nm, revealed nodules of size of about 10 nm at ambient temperature. Annealing at 373 K for 2

hours resulted in an increased size of nodules from about 10 nm at room temperature to about 20 nm after annealing. Figure 4b shows a bright-field diffraction-contrast image of annealed nodular crystals in PE [23].

### *Spherulitic superstructure*

The most prominent higher-order organization of macromolecules in polymers on a scale larger than lamellae is the formation of spherical aggregates of lamellae, called spherulites. Electron-microscope data show that spherulites are composed of lamellar crystals and amorphous structure. The size of spherulites ranges from several micrometers to a few millimeters in diameter. Spherulites are recognized by their characteristic appearance in the polarizing optical microscope (POM), where they are seen as circular birefringent objects. The birefringence is associated to the molecular orientation inside the lamellar crystals and the specific alignment of lamellae in the spherulite. In addition to the observation of spherulites on melt-crystallization, the formation of spherical objects on crystallization from the glassy state has also been observed [27]. Figure 5 shows the spherulitic morphology of PET, crystallized from the glassy state at 483 K for 10 minutes (left) [5] and crystallized from the melt at 473 K for 30 minutes (right) [28].

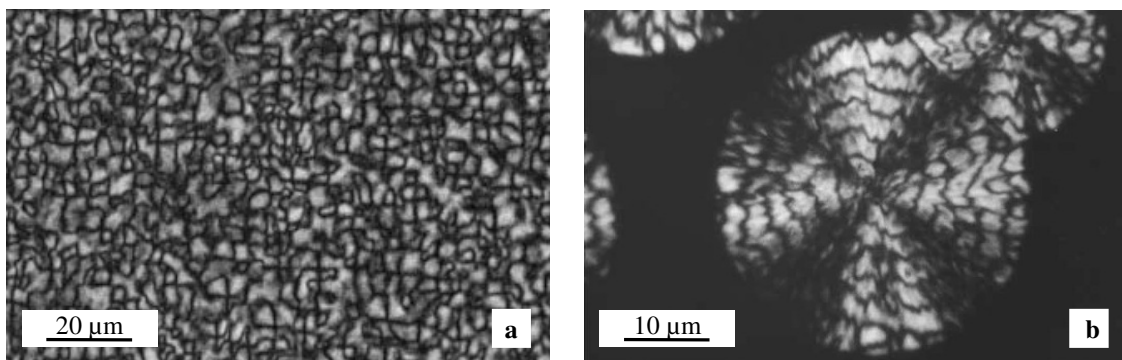


**Figure 5.** Polarizing optical micrographs of the spherulitic superstructure of PET obtained on crystallization (a) from the glassy state [5], and (b) from the melt [28].

Spherulites obtained on melt-crystallization are comparatively larger and show a strong birefringence in comparison to the spherulites obtained on crystallization from the

glassy state. Similar observations were made for polylactic acid (PLA). Formation of large number of embryos during the quenching of the sample was considered as a major reason for the formation of large number of spherulites in glass-crystallized samples [29].

### ***Rigid amorphous fraction***

The description of semicrystalline polymers as a two-phase system, consisting of a mobile amorphous phase and a crystalline phase, do not fully explain their properties, e.g., the change of glass transition temperature of poly(butylene terephthalate) (PBT) as a function of the conditions of crystallization [30]. Therefore, the two-phase model was modified by the introduction of a rigid amorphous fraction (RAF), which can additionally form if an individual macromolecule is present in both the crystalline and amorphous parts. As a result, the mobility of chain segments present at the crystal–amorphous interface is constrained and decreases gradually with increasing the distance from the crystal surface. Figure 6 shows a sketch of a semicrystalline structure including a RAF (gray-region) [31]. In case of no coupling between the crystal and amorphous phases (A), a single glass transition temperature identical to the glass transition temperature of a fully amorphous polymer is observed. On the other hand, a strong coupling between the crystalline and amorphous parts does not allow the RAF to devitrify at the glass transition temperature of the decoupled amorphous phase. In this case, two separate glass transition temperatures are observed, as in case of PET and PBT. In general, a weak coupling exists between the crystalline and amorphous regions in semicrystalline polymers (B) that broadens the glass transition temperature to higher temperatures, as in case of PE [31,32].

A number of semicrystalline polymers, including PET, PBT, PE and iPP, show the presence of RAF [6,32-34]. The phase fractions of mobile amorphous, rigid amorphous and crystalline regions can be determined by monitoring the change of heat capacity  $C_p(T)$  at the glass transition temperature, using a differential scanning calorimetry (DSC) and is expressed by the following equation:

$$C_p(T) = m_c(T)C_{p,c}(T) + m_{maf}(T)C_{p,maf}(T) + m_{raf}(T)C_{p,raf}(T) \quad (6)$$

where subscripts *c*, *maf* and *raf* denote the terms crystalline, mobile amorphous and rigid amorphous fractions, respectively, and *m* is their respective mass fraction. The quantities

used in equation 6 are temperature dependent. The temperature dependencies of the  $C_p$  of the crystalline and amorphous phases are listed in ATHAS Data Bank and can be used together with the experimentally observed heat capacity of a semicrystalline polymer to determine the crystalline, mobile amorphous and rigid amorphous fractions [35].

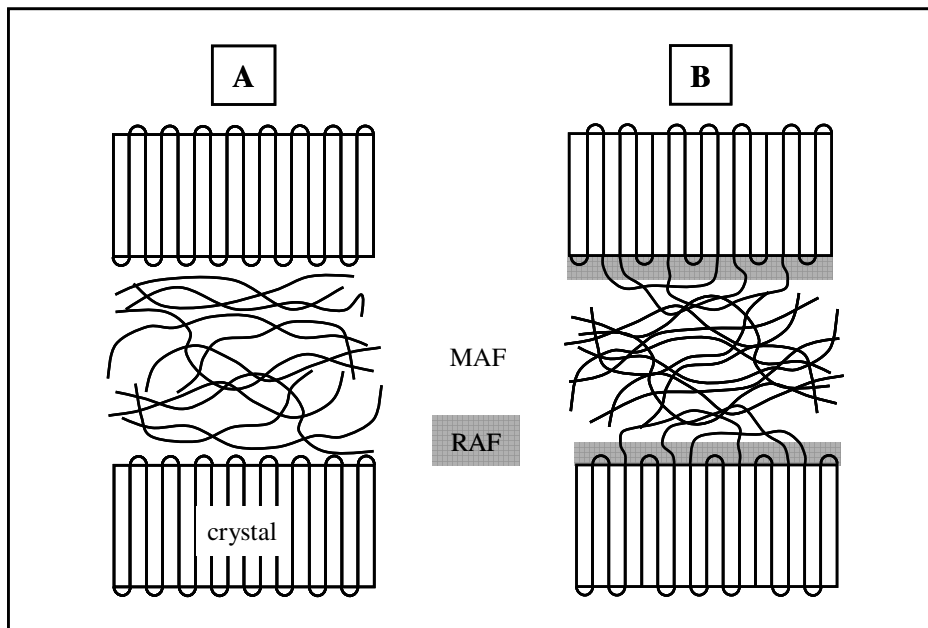


**Figure 6.** Schematic representation of (A) a completely decoupled and (B) a partially coupled crystal-amorphous interface, in a semicrystalline polymer [31].

For a detailed analysis of the determination of the fractions of different phases, as an example, the change of  $C_p(T)$  of a 40 % crystalline polymer is shown in Figure 7. The  $C_p(T)$  of a completely crystalline phase and a liquid phase of the same polymer is shown by the lines 1 and 4, respectively. The supposed experimentally observed heat capacity and the heat capacity of a 40 % crystalline sample (based on the two-phase model with 60 % of devitrified amorphous part) are shown by the lines 2 and 3, respectively. The  $C_p$  of the crystalline phase increases steadily with increasing temperature, whereas the  $C_p$  of the amorphous phase shows a step-like increase at the glass transition temperature, due to the onset of the cooperative mobility of macromolecules in the amorphous phase. The  $C_p$  of the glass is identical or close-to that of the crystal below the glass transition temperature

and above the glass transition temperature the  $C_p$  of amorphous structure is that of the liquid. If the two-phase model is valid then the expected change of the  $C_p$  at the glass transition temperature should meet the dotted line, as represented by an arrow connecting the lines 2 and 3, i.e., indicating the presence of amorphous and crystalline fractions and no RAF. However, the experimental data shows deficiency of the  $C_p$  at the glass transition temperature, indicating the presence of a RAF, which do not mobilize at the glass transition temperature and therefore do not contribute to the increment of the  $C_p$  at the glass transition temperature. The fractions of amorphous, crystalline and rigid amorphous phases can be quantitatively determined from this analysis [31].

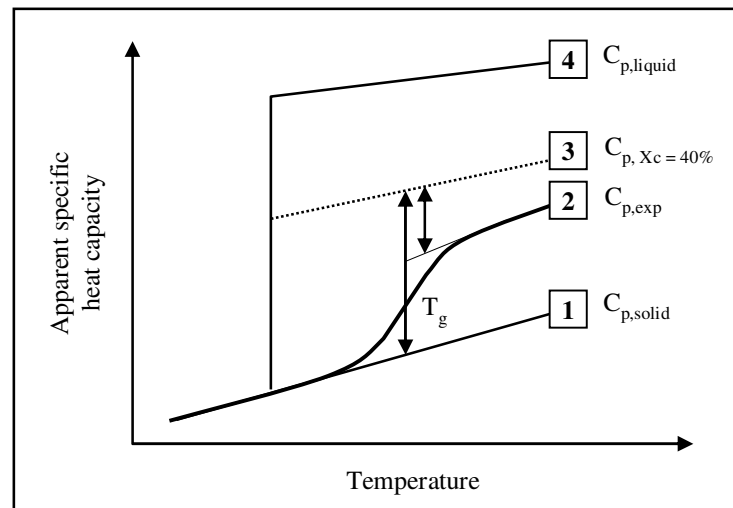


**Figure 7.** Temperature dependence of the heat capacity of a semicrystalline polymer of 40 % crystallinity [31].

### ***Skin-core morphology***

Shear forces and temperature gradients in processed products of semicrystalline polymers result in formation of a skin-core morphology, as shown in figure 8 for iPP [36]. The skin-core structure has three layers, a skin layer formed at the surface of the product, a core layer formed in the center, and a layer of maximum orientation between the skin and the core [4]. During the cooling process, the surface layer of the processed product immediately solidifies as it comes in contact with the mold wall or the cooling medium. This results in the formation of metastable structure at the surface. For instance,

the smectic form of iPP is formed at the surface of cast films, on a chill roll. Similarly, in the inflation film production the smectic form of iPP dominates, if the cooling is performed in water. The complicated effect of shear and elongational forces causes the molecular orientation in the flow direction, which results in the formation of highly orientated structure in the skin-layer. The orientation decreases after passing a maximum just below the surface, across the thickness of the product. The core represents a disoriented part of the molded object. The resolution level of optical microscopy shows that the morphology becomes increasingly spherulitic with increasing distance from the surface towards the core due to decreasing rate of cooling and comparatively strain-free crystallization conditions. This also results in an increase of crystallinity, from the skin to the core layer. A shear-induced layer between the skin and the core exhibits a shish-kebab morphology, which contains two main components, the oriented fibrils and the chain-folded lamellae. The fibrils result from the region of the melt where chains are extended, due to shear forces, whereas the chains which do not attain a high degree of orientation, crystallize epitaxially on the fibrils, forming a chain-folded structure [36,37].

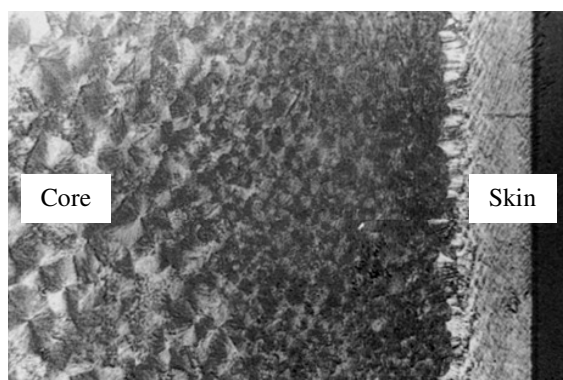


**Figure 8.** Skin-core morphology of injection molded iPP [36].

### **2.3. Isotactic polypropylene**

#### ***An isolated chain of iPP***

Macromolecules in the polymorphic forms of iPP adopt a  $3_1$ -helical conformation, with a repeat distance of 0.65 nm. The helical conformation results due to the presence of asymmetrically substituted methyl groups that cause a rotation of the main chain, involving three monomer units to complete one helical turn. The helical conformation

gives rise to the formation of right-handed (R) and left-handed helices (L), as shown in Figure 9. The terms ‘up’ or ‘down’ indicate that the CH<sub>3</sub>–CH bond has a positive or a negative component along helix axis, respectively. The intra-molecular interactions of all four types of helices are identical, however, their intermolecular interactions with each other depend on their insertion in the crystal lattice [37].

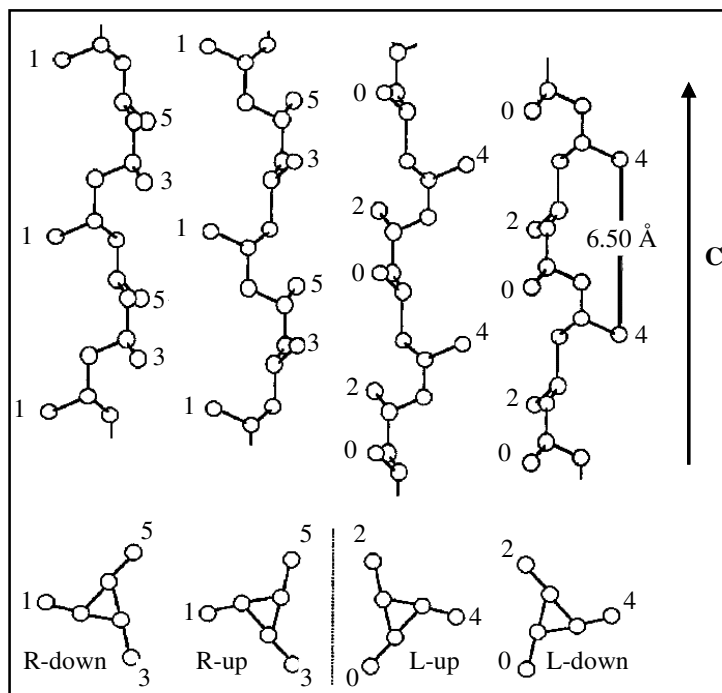


**Figure 9.** The  $3_1$ -helical conformation and four possible ways of insertion of iPP chain in the crystal lattice. R and L denote the Right and left handed helices, respectively [37].

### 2.3.1. Crystal polymorphs of isotactic polypropylene: The $\alpha$ -, $\beta$ - and $\gamma$ -forms

#### *Crystallographic symmetry*

The helical arrangement of macromolecules in the  $\alpha$ -form of iPP results in a monoclinic unit cell, with dimensions  $a = 0.665$  nm,  $b = 2.096$  nm,  $c = 0.65$  nm and  $\beta = 99^\circ 20'$  [38]. Figure 10a shows the packing of left and right handed helices in a monoclinic unit-cell with chain axis parallel to the b-axis. The X-ray diffraction pattern of an un-oriented sample of iPP with typical reflections of the monoclinic  $\alpha$ -structure is shown in Figure 11a. Depending on the thermal and mechanical history of the sample, the  $\alpha$ -form of iPP may show various degrees of disorder in the up and down positioning of the

chains, as the substitution of an up-helix chain by a down-helix chain is possible at the expense of same packing energy. However, the unit-cell dimensions and the ordered arrangement of right and left handed helices within the unit-cell remain substantially unchanged [39].

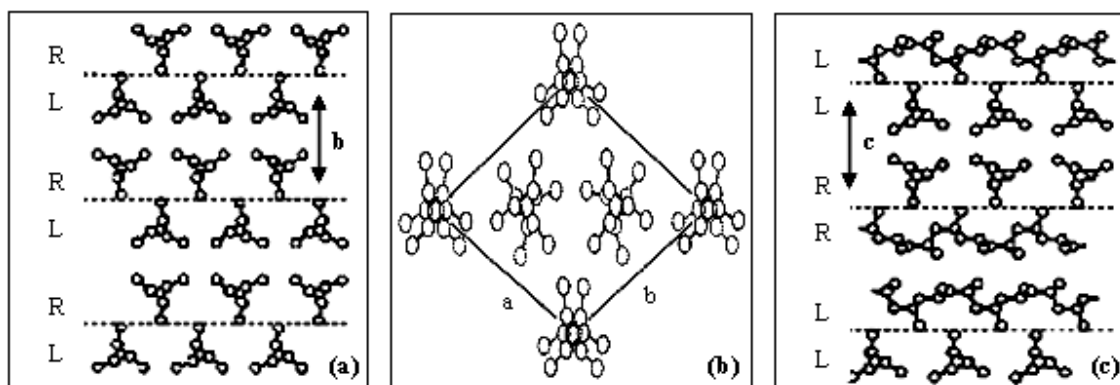


**Figure 10.** Crystal structure of (a) monoclinic  $\alpha$ -form [38], (b) hexagonal  $\beta$ -form [40,41] and (c) triclinic  $\gamma$ -form [44] of iPP. The dashed horizontal lines distinguish bilayers of  $3_1$ -helical chains. L and R denote the left and right handed helices, respectively.

Macromolecules in the  $\beta$ -form of iPP arrange in a hexagonal unit cell, with dimensions  $a = b = 1.101$  nm and  $c = 0.65$  nm, containing three isochiral helices [40, 41]. A unique characteristic of the  $\beta$ -form of iPP is that it is frustrated because of the different arrangement of chains, as shown in Figure 10b, since the corner chains are rotated by about  $180^\circ$  (or, in view of the three fold symmetry of the helices, by about  $60^\circ$ ) relative to the two middle chains [42]. Figure 11b shows the powder X-ray diffraction pattern of the bulk sample of  $\beta$ -iPP, containing only minor amounts of  $\alpha$ -form [43].

The  $\gamma$ -form of iPP is characterized by a triclinic unit cell structure, which is considered as a sub-cell of a much larger face-centered orthorhombic unit cell with parameters  $a = 0.854$  nm,  $b = 0.993$  nm and  $c = 4.241$  nm, where the  $c$ -axis of the smaller cell is parallel to the diagonals of the  $ab$ -plane of the larger cell. The crystal structure of the  $\gamma$ -form of iPP was calculated from the X-ray diffraction data obtained on a slowly cooled powder sample of low molecular weight polypropylene. The structure is characterized by a regular packing along the  $c$ -axis direction of bilayers of chains with axis oriented alternatively along two nearly perpendicular directions. Figure 11c shows

the X-ray diffraction pattern of the pure  $\gamma$ -form of iPP. The basic feature of the  $\gamma$ -iPP is the coexistence of non-parallel chains in the same crystal lattice, as shown in Figure 10c. Qualitative analysis of the  $\gamma$ -form suggests that the crystal is built up of layers of chains in a crossed pattern, where the chains in adjacent layers are tilted at an angle of  $80^\circ$  or  $100^\circ$  to each other [42,44].

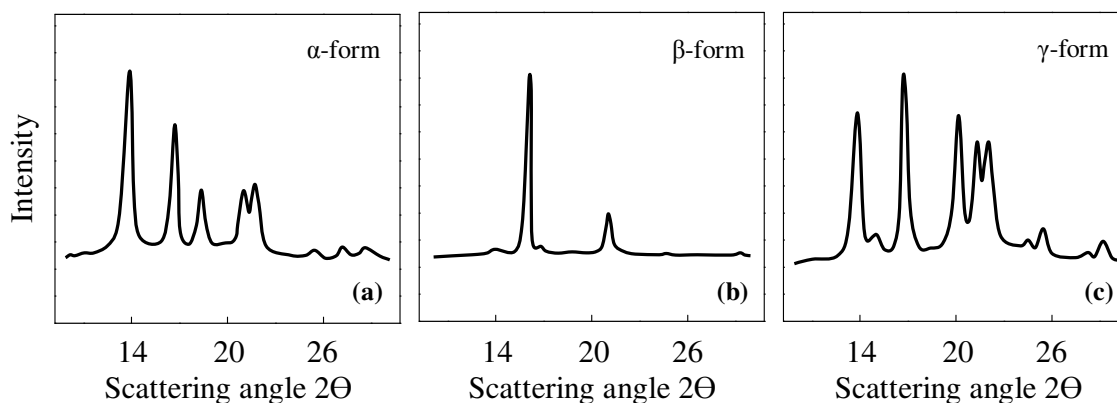


**Figure 11.** X-ray diffraction pattern of (a) monoclinic  $\alpha$ -form, (b) hexagonal  $\beta$ -form and (c) triclinic  $\gamma$ -form of iPP [39].

### ***Lamellar and spherulitic morphology***

Different appearance of spherulitic superstructure and lamellar crystal morphology of iPP, helps in associating them to different polymorphic forms of iPP. The  $\alpha$ -form of iPP can primarily be obtained by slow melt-crystallization, e.g., cooling at  $10 \text{ K min}^{-1}$ , and also by the addition of  $\alpha$ -nucleating agents, like sodium. It forms a cross-hatched lamellar structure, as shown in Figure 12a [45]. The cross-hatched structure is considered as a special case of homoepitaxy, in which the tangential lamellae in a spherulite are grown at the 010-lateral surface of the radial lamellae. The growth of tangential lamellae occurs at an angle of  $80^\circ$  or  $100^\circ$ , with identical handedness of the chains in the radial and tangential lamellae [39,46,47]. Cross-hatching and the thickness of lamellae depend on the crystallization conditions. An increase of the temperature of isothermal melt-crystallization reduces the cross-hatching and increases the thickness of lamellae. For instance, crystallization of a highly isotactic sample of iPP at a temperature of 418 K for a period of 48 hours, produced lamellae of thickness of about 18 nm. Increasing the temperature of melt-crystallization to 439 K and the time of isothermal melt-

crystallization to 180 days increased the thickness of lamellae to 66 nm, whereas no cross-hatching was observed [48,49].

The spherulites associated with the  $\alpha$ -form of iPP are classified as types I, II and mixed. Spherulites of type-I form on melt-crystallization at a temperature of below about 406 K. These spherulites are identified with a well-defined Maltese-cross and a positive optical birefringence, due to increased quantities of the tangential lamellae. Spherulites of type-II appear on melt-crystallization at a temperature of above about 410 K. These spherulites also show a Maltese-cross but with negative birefringence, which is favored in case of increased quantities of radial lamellae. Melt-crystallization between temperatures of about 406 and 410 K results in formation of both types of spherulites with no well-defined Maltese cross pattern [50,51]. The size of  $\alpha$ -spherulites can be controlled by the temperature of isothermal melt-crystallization and by the rate of cooling of the melt [15,48]. Figure 13a shows, as an example, the type-I spherulites of the  $\alpha$ -form of iPP, obtained on melt-crystallization at 393 K [36].

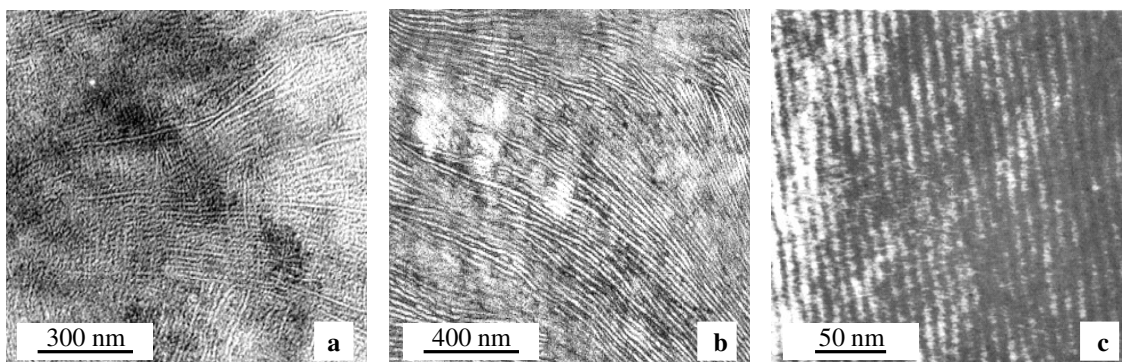


**Figure 12.** TEM-images of (a) cross-hatched lamellar crystal morphology of  $\alpha$ -monoclinic form [45] and non-cross-hatched lamellar crystal morphology of (b)  $\beta$ -hexagonal form [52] and (c)  $\gamma$ -triclinic form [53] of iPP.

The  $\beta$ -form of iPP can predominantly be obtained by the addition of  $\beta$ -nucleating agents, such as  $\gamma$ -quinacridone, and by crystallization under controlled degree of supercooling. The morphology of the  $\beta$ -form of iPP shows stacked lamellae without cross-hatching [54,55]. The growth direction of lamellae within the spherulites is along the crystallographic a-axis of the hexagonal unit cell [56]. Figure 12b shows a TEM

micrograph of lamellar crystal of the  $\beta$ -form of iPP obtained in a  $\beta$ -nucleated polypropylene, after isothermal melt-crystallization at a temperature of 403 K for a period of 30 minutes [52]. Spherulites related to the  $\beta$ -form of iPP are classified as  $\beta_{III}$  and  $\beta_{IV}$  types and are identified by a more pronounced negative birefringence than the  $\alpha$ -form of iPP. The optical classification of the  $\beta$ -spherulites depends on the lamellar microstructure. The  $\beta_{III}$ -type spherulites crystallize from melt below a temperature of about 401 K and exhibit uniform radial birefringence that is linked to the random orientation of lamellar crystals about the radial direction of a spherulite. In contrast,  $\beta_{IV}$ -type spherulites crystallize from the melt between 401 and 405 K and show concentric banding due to the periodic orientation of lamellae about the radial direction of a spherulite [49,56]. Figure 13b shows, as an example, the negative ringed  $\beta_{IV}$ -type spherulites of iPP, obtained on melt-crystallization at 408 K [36].

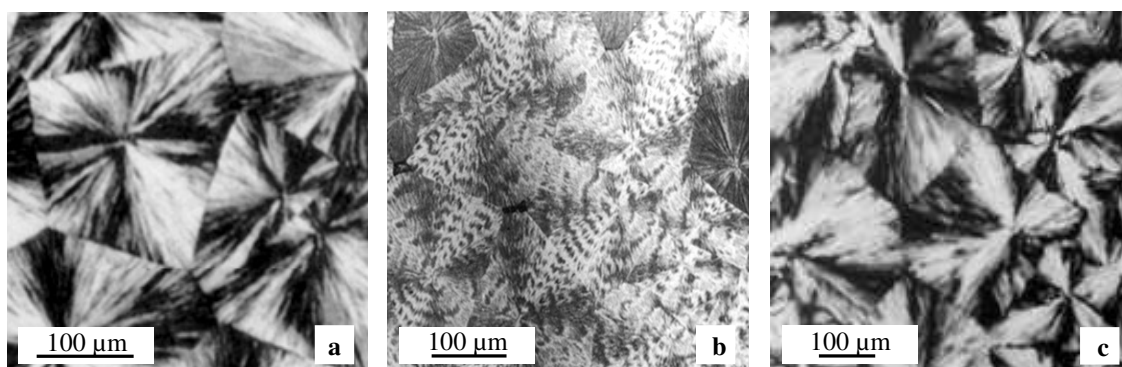


**Figure 13.** Polarizing optical micrographs of (a)  $\alpha$  type-I spherulites (b) negative ringed  $\beta_{IV}$ -spherulites [36] and (c) positively birefringent  $\gamma$ -spherulites [57].

The  $\gamma$ -form of iPP is not generally obtained under typical processing conditions. It was first obtained in a low molecular weight iPP, on slow melt-crystallization. Other ways to obtain the  $\gamma$ -form is the crystallization of high molecular weight iPP at a pressure of about 200 MPa or by the addition of small amounts of co-monomers (4–10 %), such as ethylene [4,37,58]. Figure 12c shows the lamellar crystal morphology of the  $\gamma$ -form of iPP, epitaxially crystallized on benzoic acid [53]. Electron diffraction and electron microscopy experiments on low molecular weight iPP suggested that the  $\gamma$ -form lamellae can nucleate on the (010)-face of the parent  $\alpha$ -form crystal in thin films [56]. Melt-

crystallization at a pressure of 200 MPa, exhibits three distinct classes of  $\gamma$ -spherulites, categorized according to the sign of birefringence. Positively birefringent spherulites are observed at temperatures below 457 K and above 472 K. Negatively birefringent spherulites are observed on melt-crystallization at a temperature between 460 and 471 K. A mixed birefringence is obtained on crystallization at a temperature between 455 and 461 K and between 469 and 473 K. Figure 13c, as an example, shows positively birefringent  $\gamma$ -spherulites obtained on isothermal melt-crystallization at a temperature of 478 K and a pressure of 200 MPa [57].

### 2.3.2. Mesomorphic isotactic polypropylene

#### *Crystallographic symmetry*

The structure of the mesomorphic form of iPP, out of various proposed structures, having a pseudo-hexagonal crystal symmetry with right and left hand helices arranged at random, is shown in Figure 14. The structure is drawn as projecting along the chain axis. The filled and open triangles refer to left and right handed helices, respectively. The height of the methyl groups is expressed in twelfths of the c-axis [59].

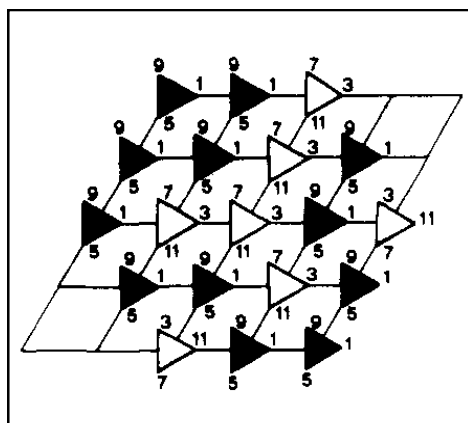


**Figure 14.** Pseudo-hexagonal crystal symmetry of the mesomorphic form of iPP [59].

The structure of mesomorphic iPP, like other polymorphic forms of iPP, is also characterized by a  $3_1$ -helical chain conformation. The chain packing in the mesomorphic phase is less dense due to the existence of disorder in the cross-chain direction. This results in a structure with an intermediate order between the crystalline and amorphous

phases [38]. The mesomorphic form of iPP has frequently been termed as smectic [38], paracrystalline [60], conformationally disorderd crystals [61], fine hexagonal crystals [62] and small monoclinic crystals [63]. The unit cell dimensions of the mesomorphic iPP, consisting of microcrystalline regions of about 10 to 20 nm in size, with proposed monoclinic  $\alpha$ -structure, were found to be about  $a = 0.667$  nm,  $b = 2.089$  nm,  $c = 0.648$  nm and  $\beta = 98^\circ 4$  [64].

### ***Structure and morphology formation***

Mesomorphic iPP results either on rapid melt-crystallization, typically at a cooling rate faster than about  $80 \text{ K s}^{-1}$ , or by heating the amorphous state of iPP to a temperature of above about 300 K [2,65]. The mesomorphic form of iPP can be recognized by two halos in a wide-angle X-ray scattering (WAXS) pattern. The morphology of mesomorphic iPP, at ambient temperature, has consistently been described as nodular. The size of nodules is reported to be between about 3 to 20 nm [66,67]. Figure 15 shows (a) WAXS pattern and (b) the nodular morphology of mesomorphic iPP, at ambient temperature [66,22].

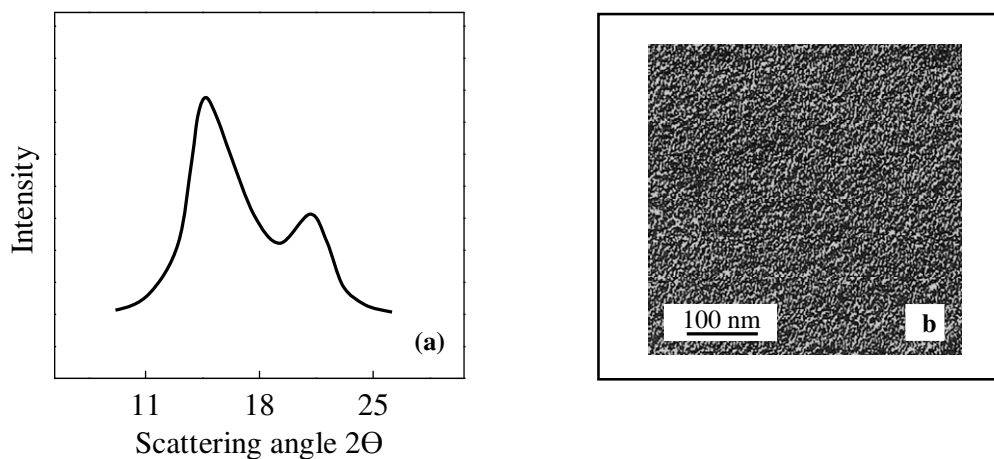


**Figure 15.** (a) WAXS pattern [66] and (b) morphology of mesomorphic iPP [22].

Structure formation on crystallization from the melt and from the glassy state and the morphology of the mesomorphic iPP have been analyzed by using DSC, WAXS and TEM [2,3,68]. Investigation of the melt-crystallization of iPP was performed using a fast-

scanning nano-calorimetry. Figure 16 shows the crystallization temperatures related to the monoclinic and mesomorphic forms of iPP, as a function of cooling rate [3].

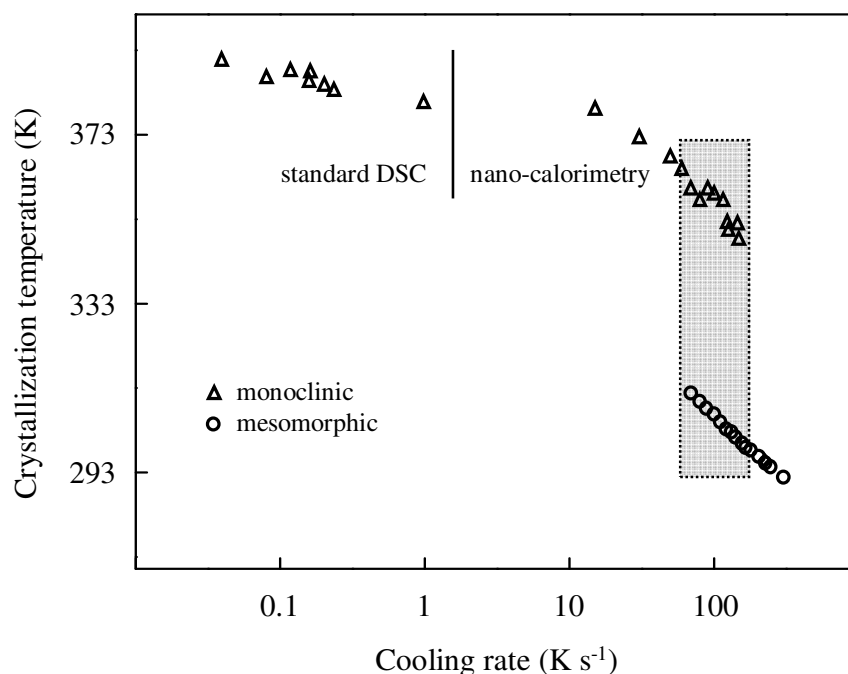


**Figure 16.** Exothermic peak positions as a function of the rate of cooling of the melt. The vertical line separates the data points obtained from standard DSC and from fast nano-calorimetry. The range of cooling rates represented by the gray area, results in the crystallization of monoclinic and mesomorphic forms of iPP in a single cooling scan [3].

Increasing the cooling rate from 0.02 to 120 K s<sup>-1</sup> decreases the crystallization temperature, of monoclinic  $\alpha$ -structure, from about 390 to 350 K, respectively. A second exothermic event at a lower temperature of about 300 K is observed on melt-crystallization at a cooling rate between 90 and 150 K s<sup>-1</sup> (gray-region). Observation of the low temperature exothermic event pointed to the formation of a second crystalline phase, the mesomorphic phase. Further increase of cooling rate to above about 320 K s<sup>-1</sup> completely suppressed the formation of monoclinic  $\alpha$ -structure and revealed only the crystallization of mesomorphic phase. Finally, above the cooling rate of about 1000 K s<sup>-1</sup> only amorphous structure of iPP was obtained, as no exothermic event was observed [3]. Evidence of the formation of completely amorphous structure was also observed by

WAXS analysis on a 80  $\mu\text{m}$  thick film of iPP, initially quenched in isopentane kept at a temperature of about 130 K. WAXS analysis showed a diffuse diffraction pattern similar to the amorphous iPP. Monitoring the evolution of WAXS pattern on heating, from about 130 K to ambient temperature, revealed the formation of mesomorphic phase at a temperature of about 253 K [22]. Further evidence of the formation of mesomorphic phase from the amorphous structure of iPP was obtained from DSC and dynamic-mechanical analysis (DMA). Heating the amorphous iPP in a DSC showed the glass transition temperature at a temperature of about 255 K followed by an exothermic event located at a temperature of about 263 K. Similarly, DMA analysis of the heating of amorphous iPP showed two loss-factor peaks, located at temperatures of 263 and 283 K. The temperature of 263 K, observed as an exothermic event in DSC and the loss-factor peak in DMA, were linked to the formation of mesomorphic phase, being in agreement with WAXS results [2, 68]. It was suggested that an increased mobility of chains in an amorphous iPP, on heating, involves a small number of carbon atoms, which presumably results in the local rotation and improvement in the packing of the chains to form a mesomorphic structure [2].

### ***Reorganization of structure and morphology on annealing***

Independent of the pathway of the formation of mesomorphic iPP, the observed morphology at ambient temperature is nodular. Two important aspects of the nodular, mesomorphic form of iPP have been studied in detail:

1. The structural reorganization of the mesomorphic form on heating.
2. The effect of structural reorganization on the crystal morphology.

Review of the published data, unambiguously, shows that the reorganization process of mesomorphic structure on heating, above the ambient temperature, involves a mesomorphic-to-monoclinic phase transition [2,69]. Figure 17a shows the X-ray structure of initially quenched and subsequently at 423 K annealed iPP [70]. In the quenched state, the mesomorphic iPP is characterized by two broad peaks at  $2\Theta$  angles of about  $14.8^\circ$  and  $21.5^\circ$ . The characteristic X-ray pattern of the monoclinic structure of iPP is observed, if the temperature is raised to about 350 K. Further heating to 423 K results in an increase

of the intensity of crystalline peaks of the monoclinic structure. The monoclinic structure does not change on subsequent cooling to ambient temperature, indicating that the mesomorphic-to-monoclinic phase transition occurs irreversibly [2,70].

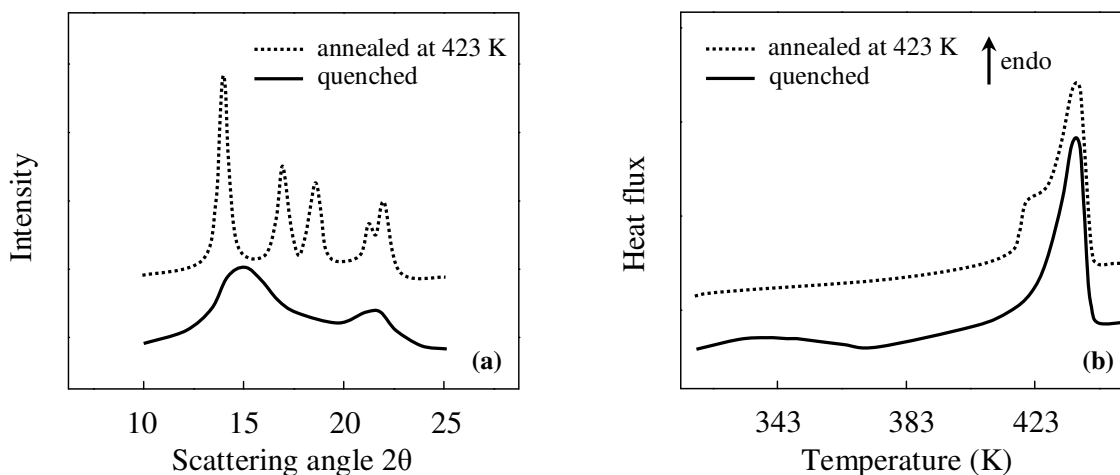


**Figure 17.** (a) WAXS pattern and (b) DSC heating scans of quenched and at 423 K annealed iPP [70].

Further evidence of the phase transition of the mesomorphic phase was obtained from DSC analysis. Figure 17b shows the DSC heating scans of initially quenched and subsequently at 423 K annealed iPP [70]. The initially quenched sample of iPP shows an endothermic event in the temperature range of about 313 to 353 K, with its center located at a temperature of about 330 K, and an exothermic event in the temperature range of about 353 to 400 K, with its center located at a temperature of about 370 K. These events were linked to the melting and re-crystallization of initially formed mesomorphic domains into monoclinic crystals, respectively. These events are absent in the sample annealed at 423 K, the shoulder observed in this preparation was linked to the melting of crystals of low stability [64,69-76]. It was suggested that rewinding of helices leads to a mesomorphic-to-monoclinic phase transition [74,77].

Reports about the effect of mesomorphic-to-monoclinic phase transition on the crystal morphology show the preservation of initially formed nodular morphology as well as the formation of lamellae. Figure 18a shows a TEM-image of the nodular crystal morphology of mesomorphic iPP. The size of nodules ranges between 7 to 10 nm [2].

Figure 18b [2] and 18c [71] show the TEM micrographs, reported by two different groups, after annealing at 393 K for 4 days and for 60 minutes, respectively. Figure 18b shows the preservation of nodular morphology, after annealing at 373 K for an extended period of time. The size of nodules is increased from initially about 10 nm to about 20 nm. Figure 18c, in contrast, shows the formation of lamellae, suggested to be formed via a process of secondary crystallization, after annealing at identical temperature, even though the annealing time is only 60 minutes. These two different reports suggest that to accurately analyze the effect of phase transition on the crystal morphology a more profound method, such as an in situ AFM experiment needs to be performed.

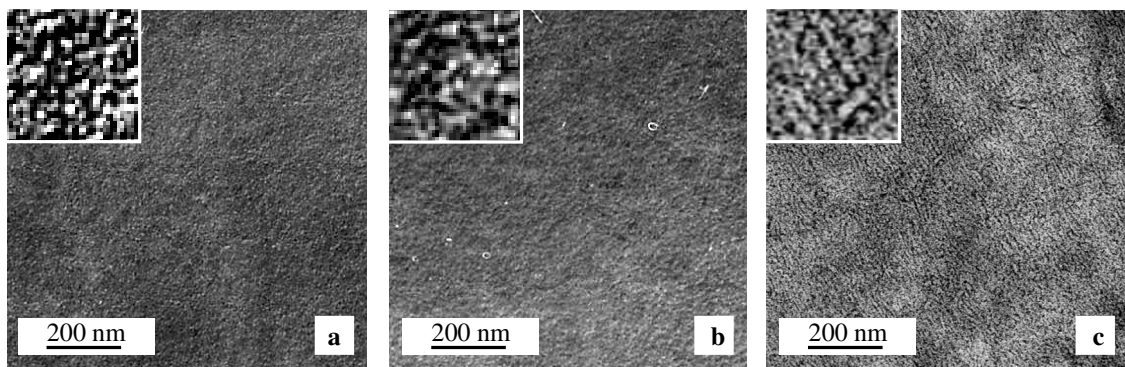


**Figure 18.** TEM-images of initially quenched iPP showing (a) a nodular crystal morphology at room temperature, (b) a nodular crystal morphology after annealing at 373 K for 4 days [2] and (c) a mixed nodular and lamellar crystal morphology after annealing at 373 K for 60 minutes [71]. The size of insets is  $100 \times 100 \text{ nm}^2$ .

### 3. Properties of semicrystalline polymers in relation to structure, morphology and crystallization conditions

Semicrystalline polymers show a strong correlation between the properties and the structure and morphology, formed as a function of the conditions of crystallization. In this section some selected properties of semicrystalline polymers are discussed.

#### *Density/Crystallinity*

The bulk density of semicrystalline polymers changes systematically with the change of structure. In detail, on primary melt-crystallization, a high-density semicrystalline polymer to a low-density mesomorphic or completely amorphous material can be obtained, at ambient temperature. Figure 19 (left) shows a general correlation between the bulk density of a semicrystalline polymer, such as iPP, polyamide 6 (PA 6) or PET, and cooling rate [78-82]. Considering the case of PA 6, the selected WAXS pattern from three different density regions are included in Figure 19 (right) [80].

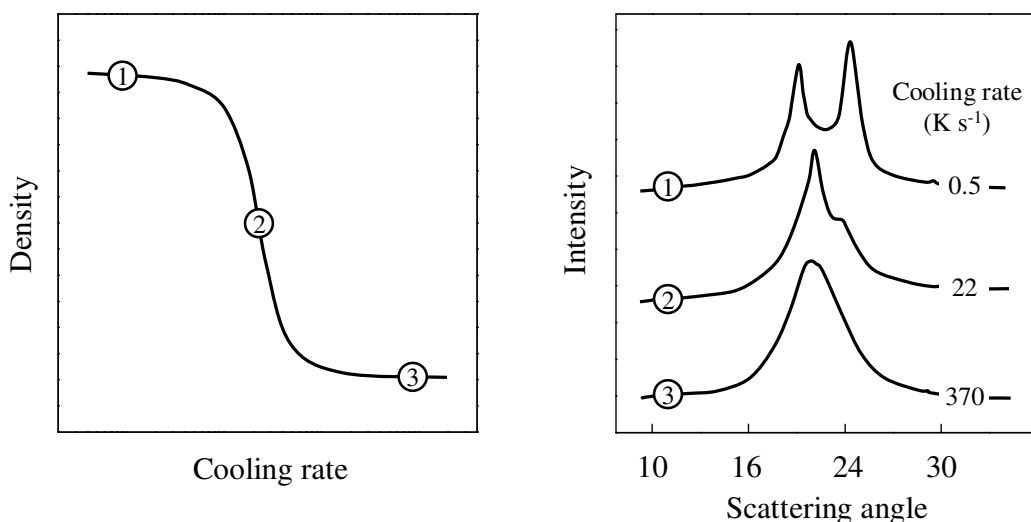


**Figure 19.** Bulk density of a semicrystalline polymer, like PA 6 (right), as a function of cooling rate and selected WAXS pattern (left), obtained at ambient temperature [80].

WAXS analysis shows a systematic change of the structure as the density changes from a high-density plateau to a low-density plateau. For instance, melt-crystallization of PA 6 at 0.5 K s<sup>-1</sup> allows the formation of high-density  $\alpha$ -structure (region 1). The change from a high-density plateau to a low-density plateau completely replaces the  $\alpha$ -structure

by a  $\gamma$ -structure, as indicated by the WAXS pattern of PA 6 melt-crystallized at  $370 \text{ K s}^{-1}$  (region 3). Simultaneously, a decrease of bulk density from about  $1.148$  to  $1.113 \text{ g cm}^{-3}$  was observed. The coexistence of both  $\alpha$  and  $\gamma$  structures of PA 6 was detected at an intermediate rate of cooling of about  $22 \text{ K s}^{-1}$  (region 2).

A similar dependence of bulk density of PET on increasing rate of cooling of melt leads to a change of triclinic structure into a completely amorphous structure. Bulk density of PET decreases from about  $1.39 \text{ g cm}^{-3}$  (region 1) to  $1.337 \text{ g cm}^{-3}$  (region 3) on increasing the cooling rate from about  $0.08$  to  $150 \text{ K s}^{-1}$ , respectively [80]. Independent studies about the crystal morphology of PET, initially slowly cooled or quenched from the melt, have shown lamellar or nodular morphology, respectively [83-85]. However, association of these differently observed morphology of PET to different density regions is speculative, since there exists no systematic correlation between the crystal morphology and bulk density, as a function of the rate of cooling on primary melt-crystallization, which is also true for other semicrystalline polymer.

Density or crystallinity of semicrystalline polymers obtained as a result of primary melt-crystallization can be further adjusted by controlling the conditions of annealing. Figure 20 shows the bulk density of initially mesomorphic iPP, as a function of annealing time at different annealing temperatures [73,86].

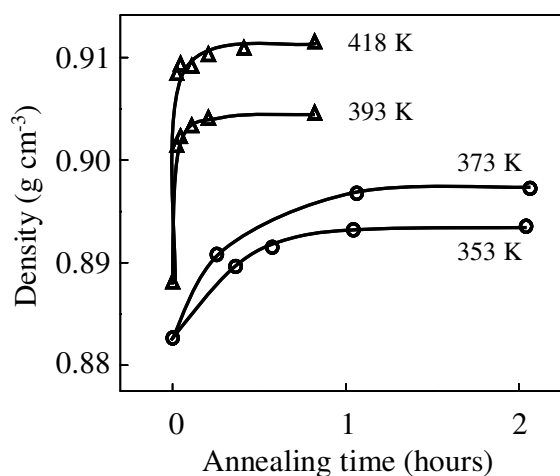


**Figure 20.** Bulk density of initially mesomorphic iPP, as a function of annealing time at different annealing temperatures. The circles and triangles represent the data taken from [73] and [86], respectively.

The observed bulk density of initially mesomorphic iPP, at ambient temperature, was about  $0.885 \text{ g cm}^{-3}$ . The density increases more gradually at annealing temperatures below about 400 K and requires a longer annealing time to reach a plateau value. In contrast, the increase of density is more prominent at annealing temperatures above about 400 K and a maximum effect is reached in shorter annealing time, since the kinetics is fast. Bulk density of iPP is the sum of densities of monoclinic and/or mesomorphic and amorphous structures, which are about  $0.8665$ ,  $0.920$  and  $0.9405 \text{ g cm}^{-3}$ , respectively, at 283 K [87]. It shows that a sample with higher fraction of monoclinic phase will show a higher bulk density and a decrease of the fraction of monoclinic phase will decrease bulk density. Figure 21 shows the fractions of amorphous, mesomorphic and monoclinic phases formed in a  $100 \mu\text{m}$  thick film of iPP, at ambient temperature, as a function of cooling rate on primary melt-crystallization [88].

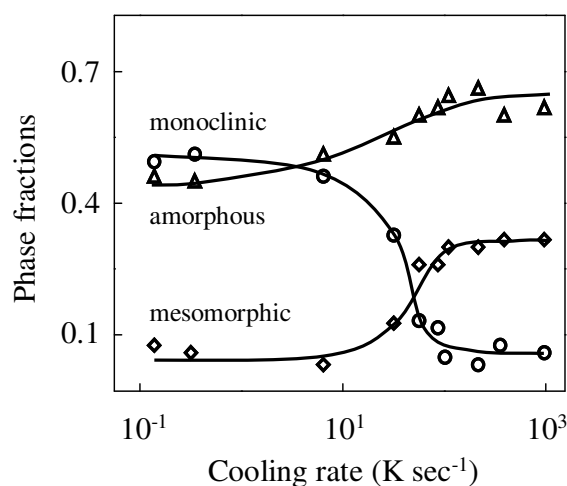


**Figure 21.** Phase fractions formed in a  $100 \mu\text{m}$  thick film of iPP, at ambient temperature, as a function of the rate of cooling on primary melt-crystallization [88].

Analysis of Figure 21 shows that a higher fraction of the monoclinic phase results on slow melt-crystallization, i.e., below about  $10^1 \text{ K s}^{-1}$ . The fraction of monoclinic phase decreases strongly on increasing the cooling rate from about  $10^1$  to  $10^2 \text{ K s}^{-1}$ , whereas the fractions of mesomorphic and amorphous phases increase. The variation of cooling rate between about  $10^2$  to  $10^3 \text{ K s}^{-1}$  do not result in an observable change of the fraction of any phase. The subsequent analysis of the bulk density of these preparations showed a

decrease from about 0.905 to 0.887 g cm<sup>-3</sup> on increasing the cooling rate from 10<sup>-1</sup> to 10<sup>3</sup> K s<sup>-1</sup>, respectively. The decrease of bulk density followed a similar trend as the decrease of the fraction of monoclinic phase, at ambient temperature, as a function of the rate of cooling on primary melt-crystallization.

Figure 22 shows the change of crystallinity of PLA as a function of the temperature of crystallization and the spherulitic superstructure of selected preparations [29]. Melt-crystallization at a temperature of about 400 K produced sample with large spherulites and a crystallinity of about 50 %. The decrease of crystallization temperature decreased the crystallinity and the size of spherulites. In contrast, quenching below the glass transition temperature resulted in a fully amorphous sample without spherulites. The change of crystallinity, in case of glass-crystallization, showed a similar trend, however, much smaller size of spherulites was observed. Figure 22 demonstrates that it is possible to obtain PLA samples of identical crystallinity with different size of spherulites [29].

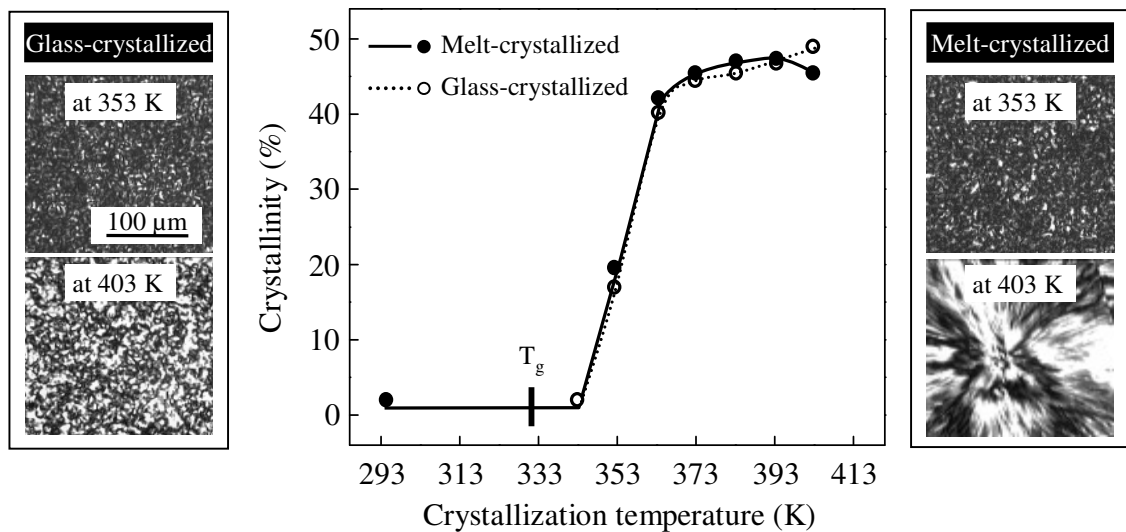


**Figure 22.** Crystallinity and spherulitic superstructure of melt-crystallized (solid line, filled circles) and glass-crystallized (dotted line, open circles) PLA, as a function of the temperature of crystallization. The scale bar is applicable to all images [29].

### **Glass transition temperature**

Glass transition temperature is a property of the amorphous part of a semicrystalline polymer and is linked to the segmental mobility of chains. Figure 23a

shows the temperature dependence of loss factor of initially quenched, mesomorphic iPP and subsequently at 413 K annealed, monoclinic iPP, measured at a frequency of 1 Hz, using a DMA [72]. The loss factor peak of quenched, mesomorphic iPP was located 5 K higher in comparison to annealed, monoclinic iPP. Another example in Figure 23b shows the change of glass transition temperature of initially mesomorphic iPP, measured at a frequency of 10 Hz using a DMA, as a function of annealing temperature [89,90]. The glass transition temperature changes almost linearly with annealing temperature, indicating a systematic increase of the chain mobility of amorphous phase [91].

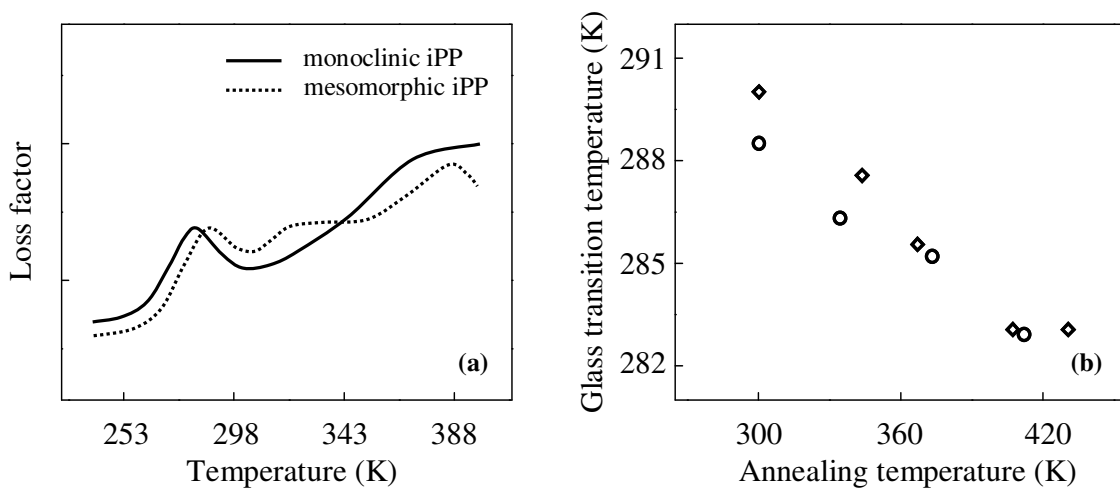


**Figure 23.** (a) Temperature dependence of the loss factor of semicrystalline iPP with mesomorphic and monoclinic structures [72], and (b) the effect of annealing temperature on the glass transition temperature of iPP, diamonds [89] and circles [90].

The rate of cooling on primary melt-crystallization is an important parameter to control the nature of interface between the amorphous and crystalline regions of a semicrystalline polymer, therefore, the glass transition temperature. Figure 24 shows the change of rigid amorphous fraction of poly(ether ether ketone) (PEEK), as a function of the rate of primary melt-crystallization. A linear relationship was observed between the cooling rate and rigid amorphous fraction. The glass transition temperature and crystallinity of two preparations are also included. The data of figure 24 shows that a decrease of crystallinity is directly linked to an increase of rigid amorphous fraction,

which in turn, shifts the glass transition temperature to higher temperatures [8,92]. Similar relationships were also established for other semicrystalline polymers [8,93].

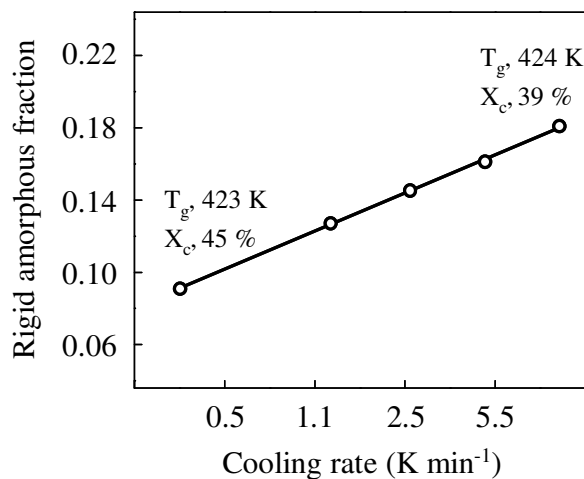


**Figure 24.** The change of rigid amorphous fraction of PEEK, measured at a heating rate of  $10 \text{ K min}^{-1}$  using DSC, as a function of the rate of cooling from the melt [92].

Figure 25a shows the change of RAF on the enthalpy-based crystallinity of cold-crystallized PET.

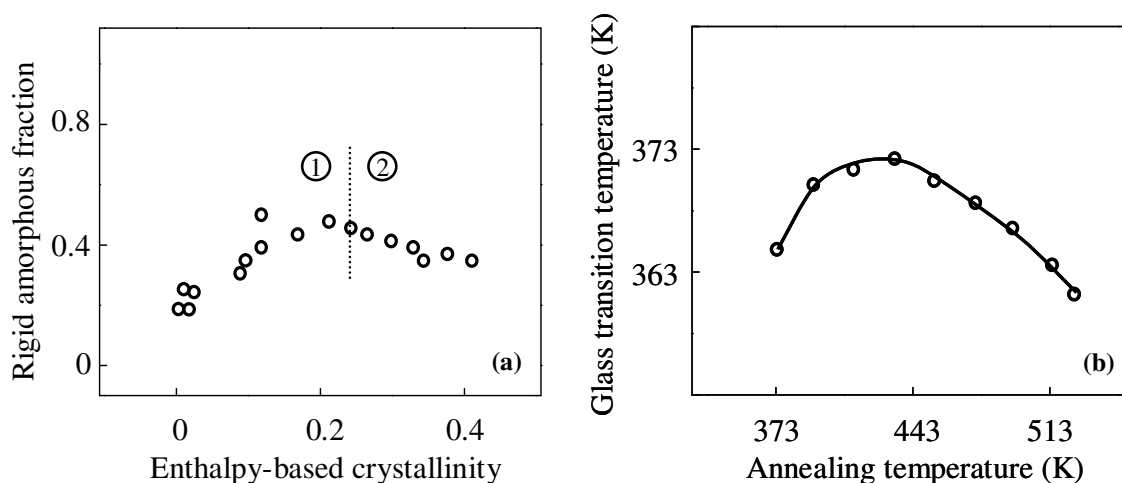


**Figure 25.** (a) Rigid amorphous fraction of PET as a function of the enthalpy-based crystallinity [6], and (b) the glass transition temperature of initially amorphous PET, as a function of the temperature of annealing [94].

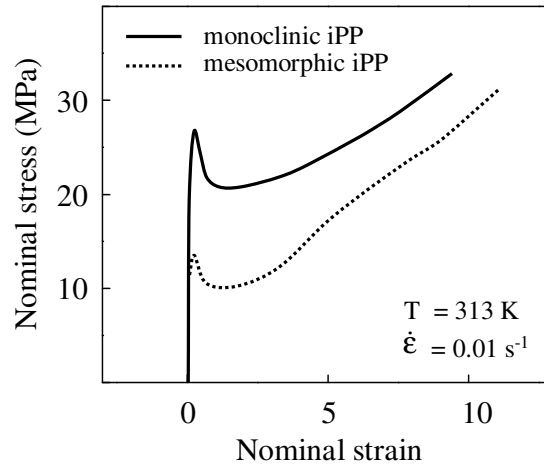
The vertical dotted line at a crystallinity of about 24 % separates the data points obtained on cold-crystallization at 390 K, as a function of time (region 1) and data points obtained by additional annealing at elevated temperatures (region 2) [6]. Isothermal cold-crystallization of PET at a temperature of 390 K increased RAF to a maximum value of 44 %, and a simultaneous increase of the enthalpy-based crystallinity to 24 %. The RAF was decreased on increasing the temperature of annealing, while the crystallinity was still increasing. These two observations were linked to the covalent coupling between the crystalline and amorphous phases and to the degree of crystal perfection, respectively [6]. Figure 25b shows a correlation between the glass transition temperature and the temperature of annealing for initially amorphous PET. The cold-crystallization of PET increased the glass transition temperature from about 364 K to about 372 K on increasing the temperature of isothermal annealing from about 373 K to about 433 K, respectively. A further increase of the annealing temperature resulted in a decrease of the glass transition temperature [94]. The data of Figure 25 obtained from independent studies shows a close correlation between the change of RAF and glass transition temperature.

#### ***Tensile-stress strain behavior, modulus of elasticity and yield stress***

The model of tensile deformation considers that the stress applied to a semicrystalline polymer, at a temperature above the glass transition temperature, primarily deforms the amorphous phase, as it is more disordered and softer than the crystalline phase. In the next stage, the amorphous phase transmits the stress to the crystalline phase, whose plastic deformation by chain-slip or by twinning is governed by the crystal defect concentration. Finally, during necking, the strain-hardening occurs as a result of chain-unfolding and orientation, leading to the formation of fibrils [89].

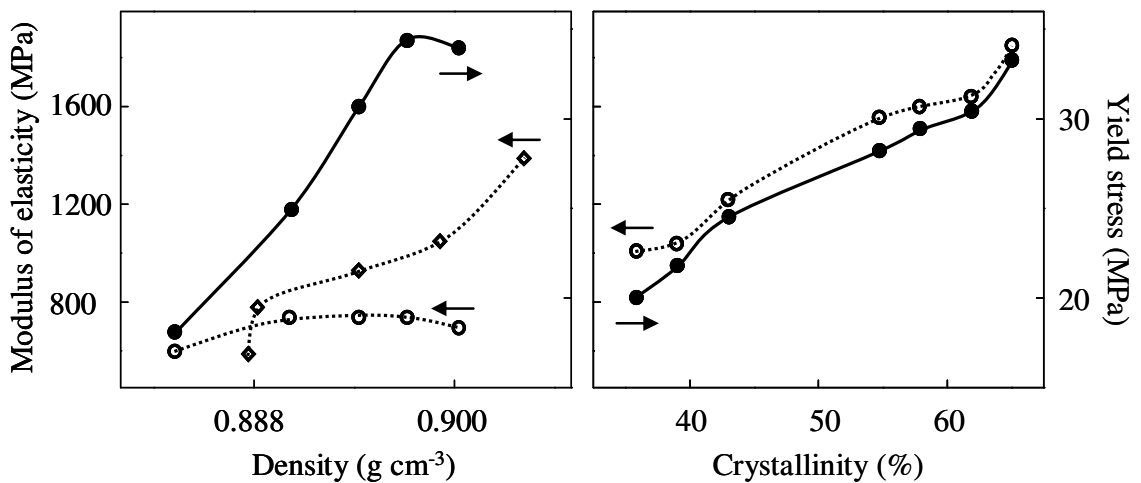
Figure 26 shows the tensile-stress strain behavior of quenched, mesomorphic iPP and subsequently annealed, monoclinic iPP, at a strain rate and temperature of  $1.05 \times 10^{-2} \text{ s}^{-1}$  and 313 K, respectively. Samples of iPP with mesomorphic and monoclinic structures were obtained by quenching a 100  $\mu\text{m}$  thick film on a chill-roll, kept at a temperature of 303 K, and by subsequent annealing at 413 K for 60 minutes, respectively [72]. Both preparations show an increase of stress with increasing strain in the post-yield region and eventually fracture at a nearly identical stress values, however, the mesomorphic iPP could be deformed to large strain values. Furthermore, the mesomorphic iPP

demonstrated a lower modulus of elasticity and yield stress and these values were increased on subsequent annealing [72,95].



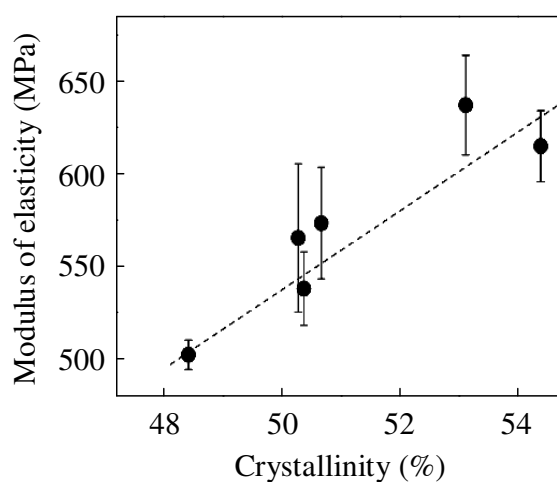
**Figure 26.** Nominal stress-strain curves of quenched, mesomorphic iPP and subsequently annealed, monoclinic iPP [72].

Figure 27 shows the effect of (a) density and (b) crystallinity on the modulus of elasticity and yield stress of initially quenched and subsequently annealed iPP [70,96,97].



**Figure 27.** Modulus of elasticity (open symbols, dotted lines) and yield stress (filled symbols, solid lines) of iPP, as a function of (a) density, open and filled circles from [96], open diamonds from [97], and (b) crystallinity, open and filled circles from [70].

The low density/crystallinity and low order structure formed in an initially quenched, mesomorphic iPP leads to a low modulus of elasticity and yield stress [95]. The increase of density/crystallinity increases the modulus of elasticity and the yield stress. Quantitatively, an increase of crystallinity from about 40 to about 60 % increased the modulus of elasticity and yield stress from about 1000 to 1500 MPa and from about 20 to 30 MPa, respectively. Recently, samples of iPB of different crystallinity were prepared by cooling at various rates from the melt and by the variation of the conditions of subsequent annealing. A linear increase of the modulus of elasticity of iPB was observed as a function of crystallinity, as shown in Figure 28 [7].



**Figure 28.** Modulus of elasticity of iPB, as a function of crystallinity. The straight line represents a linear fit [7].

The modulus of elasticity and yield stress of semicrystalline polymers increase with density/crystallinity [5,7,98], however, to explain the often observed scattering of data requires the knowledge of additional parameters, such as the crystal morphology, particularly the crystal habit. The effect of crystal habit on tensile behavior was reported for random ethylene-hexene copolymers. Tensile-stress strain curves of these copolymers showed a decrease of the yield stress with a decrease of the crystal lateral length, which was achieved by increasing the rate of cooling of the melt. In other words, a higher yield stress was obtained in presence of longer and laterally extended lamellae, which were obtained on melt-crystallization at  $0.4 \text{ K min}^{-1}$ , than a sample with shorter and curved

lamellae, which were obtained on melt-crystallization at  $129 \text{ K min}^{-1}$ . Most striking was the observation of nearly identical crystallinity and the crystal thickness of these preparations [99].

### ***Transparency and haze***

High transparency and low haze values, in films of semicrystalline polymers, are always required for coating and packaging applications, e.g., packaging of drugs and medical substances [100]. For a polymer, the transparency is defined as a fraction of the normally incident light transmitted with deviation from the primary beam direction of less than 0.1 degree. Some polymers, although transparent, may have a cloudy or milky appearance, generally known as haze. It is often measured quantitatively as the amount of light deviating by more than 2.5 degrees from the transmitted beam direction. Haze is often the result of surface imperfections [13,101]. Generally, high transparency is combined with low haze values. In a semicrystalline polymer these properties are controlled by the scattering and reflection of light due to surface roughness, impurities, voids, spherulitic superstructure, crystalline lamellae and the density difference between the crystal and amorphous phases [102].

In a film of uniform thickness, the transparency primarily depends on the spherulitic morphology, since the presence of lamellae in a spherulite has little effect on the scattering of light. This is due to the fact that the dimensions of the internal structure of the spherulites are much smaller than the wavelength of visible light [103]. This simplification of the structural parameters affecting the light transmission property of a polymer, allows to establish a direct correlation between the transparency and the size of spherulites. A polymer appears transparent, if the size of spherulites is below the wavelength of visible light, since spherulites do not hinder the passage of light. This is proven for quenched films of polyethylene. In presence of large spherulites, the light waves are scattered and the transparency is reduced, as observed for thick polyethylene objects. In contrast, polypropylene moldings appear more transparent, due to a small difference between the densities of crystalline and amorphous phases [13,101].

The use of nucleating agents is common in products of iPP, which favors the structure-specific crystallization, i.e., monoclinic  $\alpha$ -structure or hexagonal  $\beta$ -structure. Advantageously, the use of nucleating agents restricts the size of spherulites to well

below the wavelength of visible light, by increasing the rate of crystallization, and improves the transparency. However, the use of nucleating agents can undesirably cause the problem of shrinkage that can alter the dimensional stability of the product [104,105]. The addition of a nucleating agent can decrease the haze value in a 1 mm thick plate of pure iPP, from about 65 % to below about 20 % [106]. A decrease of the thickness of iPP film also decreases the haze and increases the transparency [107]. Figure 29 shows the effect of nucleating agent on haze (left) [104] and on the spherulitic superstructure of iPP (right) [108]. The increase of the amount of nucleating agent decreases the size of spherulites, which parallels the decrease of haze values [104,108]. Since spherulites are the major source of light scattering in semicrystalline polymers, therefore, fast quenching of the melt, which hinders the spherulitic growth, can be used as alternative method for improving the transparency.

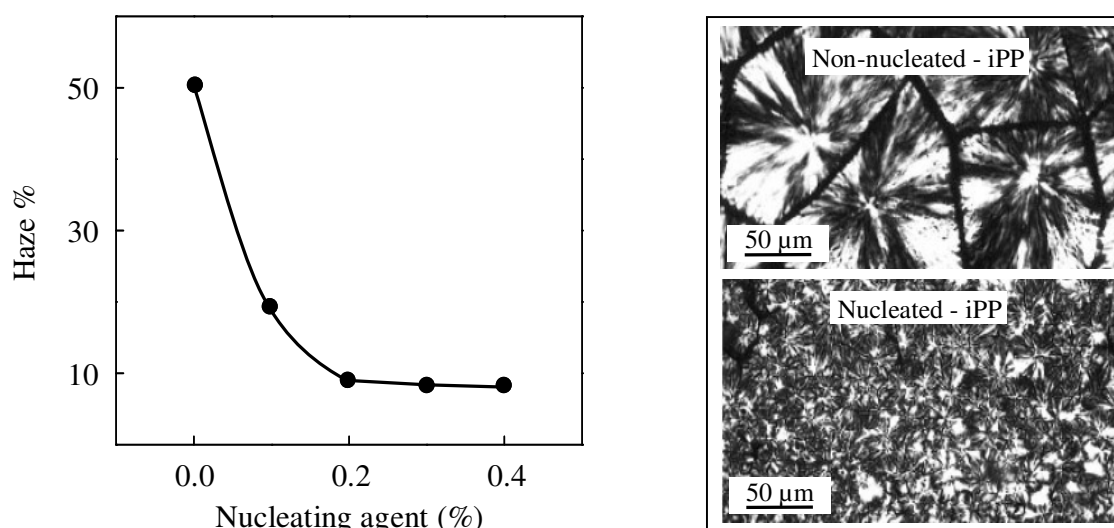


**Figure 29.** Effect of nucleating agent on haze (left) [104] and on the spherulitic superstructure of iPP (right) [108].

## 4. Material and instrumentation

### 4.1. Material

A commercial grade iPP-KF6190H (Montell Polyolefins) with a mass-average molar mass and polydispersity of  $373 \text{ kg mol}^{-1}$  and 6.2, respectively, is used in this work. The melt-flow rate is  $3.3 \text{ g (10 min)}^{-1}$ , determined at 503 K with a load of 2.16 kg.

### 4.2. Cooling device and sample preparation

Films of iPP of  $100 \mu\text{m}$  thickness were melt-crystallized, in a nitrogen-atmosphere, at cooling rates between  $10^{-1}$  to  $10^3 \text{ K s}^{-1}$ , using water as a cooling medium. The cooling rates applied were 0.1, 6, 12, 22, 33, 50, 80, 165, 230, 450, 750 and  $1050 \text{ K s}^{-1}$ . Films of iPP were prepared in two steps. In first step, the pellets were heated in a vacuum assisted compression molding machine to a temperature of 473 K, in order to obtain a pre-film of  $100 \mu\text{m}$  thickness. The holding time and maximum applied pressure were 5 minutes and 80 MPa, respectively. In second step, the  $100 \mu\text{m}$  thick pre-shaped film was re-melted and crystallized at a cooling rate between  $10^{-1}$  to  $10^3 \text{ K s}^{-1}$ , using the cooling device. A sketch of the cooling device is shown in Figure 30 (left) [80].

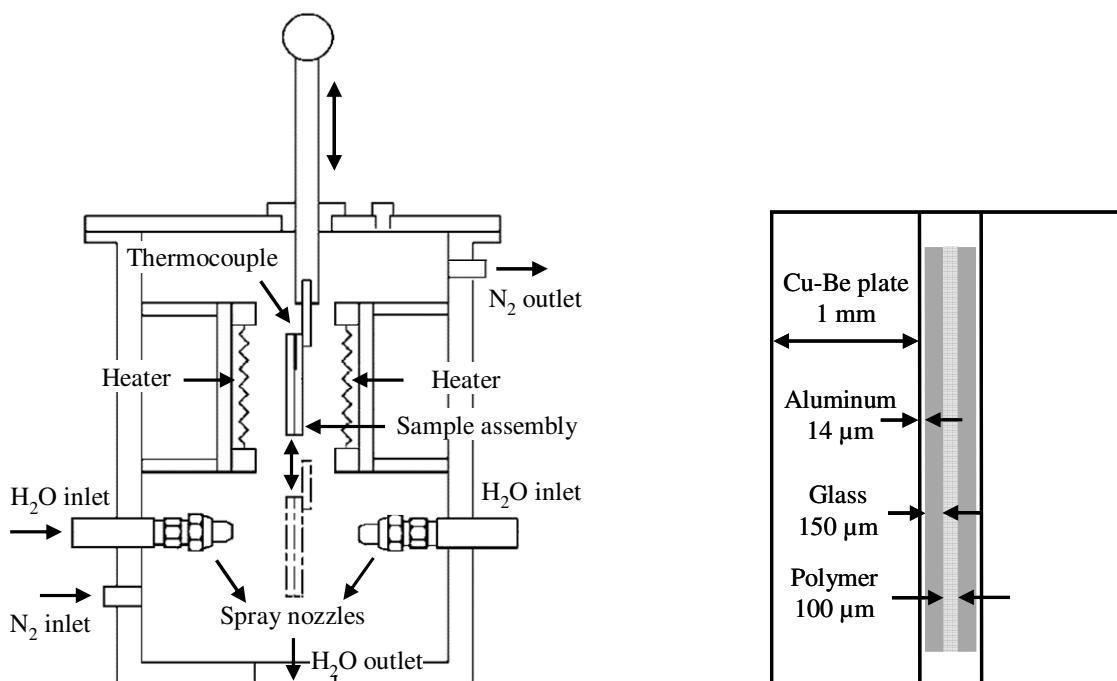


**Figure 30.** Sketch of the cooling device (left) [80], and sample-holder assembly (right).

In detail, at first iPP film was sandwiched between glass slides of about 120  $\mu\text{m}$  thickness, aluminum foil of about 14  $\mu\text{m}$  thickness (to avoid leakage of the melt) and metal plates of 1 mm thickness (for holding the sample assembly), as shown in Figure 30 (right). Next, the sample-holder assembly was heated to a temperature of 473 K in the upper portion of the device. The holding time of 5 minutes was chosen in order to erase the thermal history. Thereafter, the sample-holder assembly was pressed down into the lower portion of the device, where the coolant, i.e., water kept at a temperature of 279 K, was symmetrically sprayed from opposite sides through two identical nozzles. A fast response thermocouple, mounted between the aluminum foil and the metal plates, was used to record the thermal history by a data acquisition system. The cooling rate was estimated at a temperature of 343 K [109]. The rate of cooling on primary melt-crystallization was controlled by the choice of spray-nozzle diameter, water flow-rate and the use of metal plates of different types and thicknesses, e.g., 1 mm thick copper–beryllium alloy (Cu–Be) plates or 4 mm thick steel or copper plates [80].

### 4.3. Instrumentation

#### *Density gradient column*

The density of the initial preparations was measured at a temperature of 288 K with a density gradient column (Ray-Ran and Soffieria Sestese), using a water–ethanol mixture. The minimum and maximum detectable densities, controlling the resolution, were about 0.8840 and 0.9055  $\text{g cm}^{-3}$ , respectively. The density of iPP obtained at 288 K was recalculated to the density at ambient temperature, using equation 7, where,  $\alpha_{thermal}$  is the linear thermal expansion coefficient and  $\Delta T$  is the temperature difference between measured and extrapolated temperature. The value of thermal expansion coefficient used is  $1.05 \times 10^{-4} \text{ K}^{-1}$  [110].

$$\rho(T) = \frac{1}{1 / \rho(T_o) \times (1 + \alpha_{thermal} \Delta T)} \quad (7)$$

#### *Wide-angle X-ray scattering*

WAXS data at ambient temperature were collected on a diffractometer URD-63 (Seifert–FPM), using Nickel-filtered, Cu- $K_{\alpha}$  radiation with a wavelength of 0.154 nm,

and a scintillation counter for registration. Measurements were done in a symmetric transmission mode. A temperature-resolved WAXS analysis was performed at the Beamline–A2 at Hasylab (DESY), using a linear wire-detector for registration. The samples were heated from ambient temperature to 453 K, at a heating rate of 10 K min<sup>-1</sup>. WAXS pattern were collected at a temperature interval of 5.5 K.

### ***Polarizing optical microscopy***

Information about the superstructure of melt-crystallized and annealed samples was gained by polarizing optical microscopy, using a Leica DMRX microscope, equipped with a Leitz hot-stage 1350, and full periphery for automated data acquisition in dynamic experiments, as a function of temperature. Heating of a sample to approach the annealing temperature and subsequent cooling was done at a rate of 20 K min<sup>-1</sup>.

### ***Atomic force microscopy***

Direct analysis of the crystal morphology of initially melt-crystallized and annealed samples was made using a Q-Scope 250 AFM and a Universal Scanning Probe Microscopy (Quesant), equipped with a 40 μm × 40 μm scanner and a 5 μm × 5 μm scanner, respectively, in tapping mode. Annealing was performed in a Leitz hot-stage 1350 at a heating and cooling rate of 20 K s<sup>-1</sup>. Both phase and height mode images were collected simultaneously, at ambient temperature, using standard silicon cantilevers NSC-14 and 16 (MikroMasch), coated with aluminum at the back side, with force constants of about 5 and 40 N m<sup>-1</sup>, respectively. The resonant frequency of both cantilevers was about 170 kHz. In situ analysis of the change of crystal morphology was performed in tapping mode using a Q-Scope 250 AFM, coupled with a heating assembly provided by Quesant. Results obtained were additionally verified by using a Nanoscope IIIa AFM (Digital Instruments), coupled with a Linkam hot-stage [111].

### ***Transmission electron microscopy***

The bulk morphology of iPP films was analyzed using a TEM Tecnai G2 (FEI), operated at 120 kV. Images were collected with a Bioscan CCD Camera, Model 792 (Gatan). Films of 100 μm thickness were embedded in Epofix (Struers), and subsequently contrasted with Rutheniumtetroxide, for a period of about 12 hours [112]. Thin sections

of 75–85 nm thickness of the cross-section of the films were prepared at ambient temperature, using an Ultracut microtome (Leica), equipped with a 45°-diamond knife.

### ***Standard and Temperature-modulated differential scanning calorimetry***

DSC experiments were performed using a power-compensation-based differential scanning calorimeter DSC-7 (Perkin–Elmer). The instrument was operated in conjunction with the cryogenic cooling accessory CCA-7, ensuring a constant temperature of the heat sink at 223 K. The sample and reference furnaces were purged with nitrogen gas at a flow rate of 40 mL min<sup>-1</sup>. Calibration of the sensor temperature and of the heat-flow rate was done according to standard procedures [8], using indium and tin as calibrants. Heat-flow-rate raw-data were corrected for instrumental asymmetry by subtraction of a baseline, measured under identical conditions as the sample run, including matched masses of the aluminum pans, used for encapsulation of the samples. The baseline-corrected heat-flow-rate, finally, was converted into apparent specific heat capacity and calibrated using a comparison of the measured and expected heat capacity of sapphire. Circular and flat samples with a mass of about 1–2 mg were punched from the film and placed in 20 µL aluminum pans (Mettler-Toledo). The rates of heating and cooling were 20 K min<sup>-1</sup>. For the analysis of glass transition temperature, a higher sample mass of about 5–10 mg was used. The heating rate used was 40 K min<sup>-1</sup>. The isothermal annealing process was followed by using the identical instrument and calibration procedures. Samples of mass of about 1–2 mg were encapsulated in 20 µL aluminum pans, and heated to the annealing temperature at a rate of 10 K min<sup>-1</sup>. Subsequent temperature modulation was done using a sawtooth-type temperature profile with a programmed amplitude and period of modulation of 1 K and 120 s, respectively [113,114].

### ***Dynamic-mechanical analysis***

Dynamic-mechanical analysis of iPP of different history of crystallization was performed in threshold-tensile mode using a Mark III measuring head (Rheometric Scientific). The cross-section and the gauge length of the samples were 0.1 × 5 mm<sup>2</sup> and 8 mm, respectively. Samples were subjected to sinusoidally oscillating strain with maximum programmed amplitude of 0.1 % and a constant frequency of 1 Hz. The samples were cooled to a minimum temperature of 223 K, equilibrated for a period of 5

min, and then heated at a constant rate of 2 K min<sup>-1</sup> to a maximum temperature of 433 K. Data were collected during heating. For each preparation 1–2 samples were tested. Modulus of elasticity was determined at room temperature under identical test conditions of amplitude and frequency. For each preparation 4–5 samples were tested.

### ***Tensile testing***

Tensile mechanical behavior was recorded on a miniature tensile testing machine MiniMat-200 (Rheometric Scientific). The distance between the clamps was 8 mm. The strain rate during the initial test period of 10 seconds was 1 mm min<sup>-1</sup> for the determination of modulus of elasticity, and then was increased to 10 mm min<sup>-1</sup>. To ensure deformation of the thin films at a pre-defined position in the sample, two semi-circular notches were introduced at half gauge-length, imitating a shouldered test bar [115]. The cross-section of the films at the position of the notches was 0.1 × 2.2 mm<sup>2</sup>. For each preparation 4–5 samples were tested. For deformation experiments, a home-made stretching device was used. The sample geometry was identical as in macroscopic tensile testing experiments. Images were recorded at constant, stepwise increasing strain, that is, loading/deformation of the samples was discontinuous. The local strain at the position of the AFM tip was estimated using the AMF camera and check marks at the sample surface with an initial distance at zero strain of 0.2 mm. Samples were allowed to relax for a period of about three minutes after each deformation step before collection of the image.

### ***UV/VIS spectroscopy***

The light-transmission of iPP films was determined at ambient temperature over the visible-light wavelength range of 380–750 nm, using UV/VIS/NIR spectrophotometers Lambda-35 and Lambda 900 (Perkin Elmer). A deviation of ± 2 % in light transmission was observed for different samples of identical history of crystallization. The transparency data was normalized to a film thickness of 100 μm, using Lambert–Beer law, using equation 8 [116]. Where  $I_t$ ,  $I_o$ ,  $\tau$  and  $d$  are the intensities of incident and transmitted light, absorbance and the film thickness, respectively.

$$\frac{I_t}{I_o} = \exp(-\tau d) \quad (8)$$

## 5. Structure and morphology formation on melt-crystallization

### 5.1. Density and X-ray structure

Figure 31 shows the density of iPP, at ambient temperature, as a function of cooling rate on primary melt-crystallization (left) and the WAXS pattern of the samples of different density and history of crystallization (right) [117].

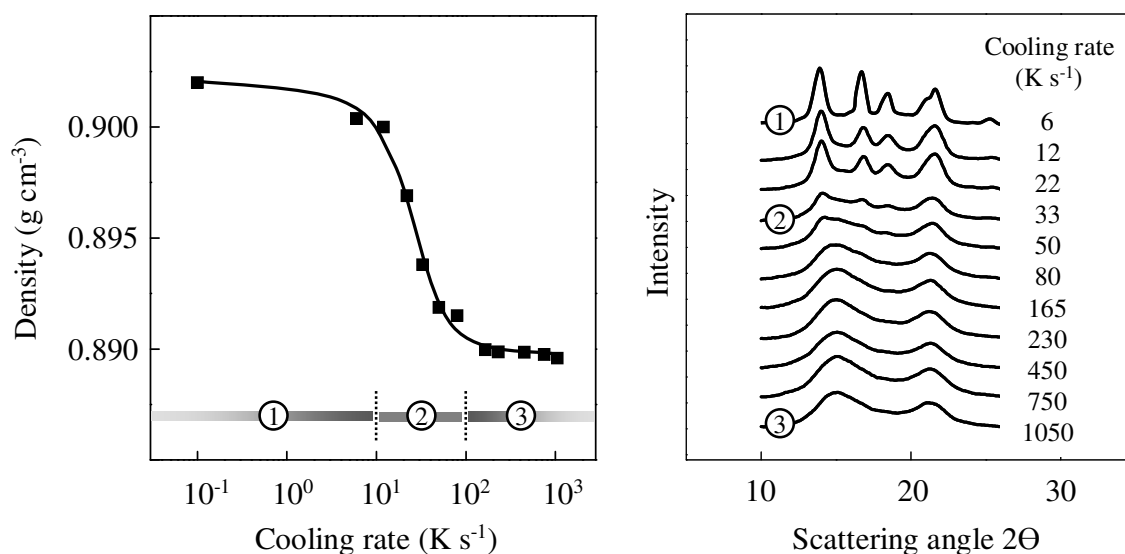


**Figure 31.** Density of iPP, at ambient temperature, as a function of cooling rate on primary melt-crystallization (left) and the corresponding WAXS pattern (right).

The data of Figure 31 allow to establish a correlation between cooling rate, macroscopic density and structure. The density and X-ray structure of samples of different history of crystallization change systematically as a function of cooling rate. Three distinct regions can be identified in the graph of density versus cooling rate (left). The selected X-ray structures representing these three regions are labeled (right). Samples melt-crystallized at a cooling rate between 10<sup>-1</sup> to 10<sup>1</sup> K s<sup>-1</sup>, form a high-density plateau (region 1). In this region, an increase of cooling rate decreases the density of preparations from about 0.902 to 0.900 g cm<sup>-3</sup>. The X-ray data show the presence of monoclinic  $\alpha$ -structure, coexisting with the amorphous phase.

An increase of cooling rate from 10<sup>1</sup> to 10<sup>2</sup> K s<sup>-1</sup>, results in a strong decrease of density from about 0.90 to 0.89 g cm<sup>-3</sup> (region 2). The distinct decrease of density in this region is due to the formation of mesomorphic phase. The simultaneous formation of

monoclinic and mesomorphic structures was detected by quantitative WAXS analysis of iPP, obtained on melt-crystallization at cooling rates between 20 and 130 K s<sup>-1</sup>. Most importantly, the change of the fraction of monoclinic phase paralleled the change of density as a function of cooling rate [88,109]. More recently, the application of fast scanning nano-calorimetry also confirmed the simultaneous formation of monoclinic and mesomorphic structures on melt-crystallization of iPP at cooling rates between 70 and 150 K s<sup>-1</sup>. The crystallization temperatures, linked to the formation of monoclinic and mesomorphic structures, were located at about 360 K and 313 K, respectively, for a sample melt-crystallized at 70 K s<sup>-1</sup>, and were decreasing on increasing the rate of cooling from the melt [3]. It is straightforward to conclude that the decrease of density is primarily linked to the decrease of monoclinic fraction, which is compensated by the simultaneous increase of the fractions of inherently low density amorphous and mesomorphic structures.

Finally, on increasing the cooling rate above 10<sup>2</sup> K s<sup>-1</sup>, a low-density plateau is observed (region 3). Samples show a constant density value of about 0.889 g cm<sup>-3</sup> and exhibit no evidence of monoclinic  $\alpha$ -structure in the X-ray scans. The X-ray data rather show two halos, located at 2 $\Theta$  values of about 15° and 21.3°, typical for mesomorphic iPP. The transition from a monoclinic iPP to a mesomorphic iPP occurs at a cooling rate of about 10<sup>2</sup> K s<sup>-1</sup>, which in the following discussion is termed as a ‘critical cooling rate’.

## 5.2. Crystal morphology and superstructure

In case of iPP, two crystallization regions linked to the heterogeneous and homogeneous nucleation are suggested. The region of heterogeneous nucleation extends to a crystallization temperature of about 350 K, when iPP melt is cooled, which involves the formation of monoclinic  $\alpha$ -structure within a spherulitic morphology. Homogeneous nucleation can occur at a crystallization temperature between about 350 K and the glass transition temperature, which results in formation of mesomorphic phase with a non-spherulitic morphology [3,49,118,119]. Indeed, no direct and detailed morphological analysis was performed in the past, which is completed in the present work and is directly related to the kinetically controlled formation of a monoclinic  $\alpha$ -structure and a mesomorphic structure in semicrystalline iPP.

### ***Spherulitic superstructure***

Figure 32 shows the optical micrographs of iPP obtained on melt-crystallization at a rate of cooling of (a) 0.1, (b) 22, (c) 80, and (d) 750 K s<sup>-1</sup>. The formation of spherulitic superstructure and the size of spherulites are controlled by the rate of primary melt-crystallization. A systematic increase of cooling rate between 10<sup>-1</sup> and 10<sup>3</sup> K s<sup>-1</sup> leads to a transition from a completely spherulitic to a non-spherulitic morphology. In detail, a space-filling spherulitic superstructure is observed on melt-crystallization at a cooling rate lower than about 10<sup>1</sup> K s<sup>-1</sup>, as shown in Figure 32a. The average diameter of spherulites decreases from about 50 μm, at 0.1 K s<sup>-1</sup>, to about 30-40 μm, at 6 K s<sup>-1</sup>. In contrast, melt-crystallization at a cooling rate larger than about 10<sup>2</sup> K s<sup>-1</sup> completely suppresses the formation of spherulites, as shown in Figure 32d. The transition from a completely spherulitic morphology to a non-spherulitic morphology occurs between the rates of cooling of 10<sup>1</sup> to 10<sup>2</sup> K s<sup>-1</sup> and shows non-space filling and isolated spherulites in a weakly birefringent matrix, as shown in Figures 32b and 32c. The diameter of spherulites decreases from about 20 μm to below 10 μm.

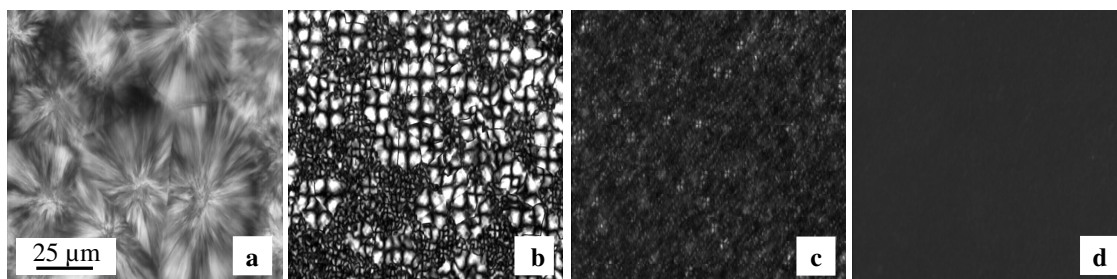


**Figure 32.** Polarizing light micrographs of iPP melt-crystallized at (a) 0.1, (b) 22, (c) 80, and (d) 750 K s<sup>-1</sup>. The scale bar is applicable to all images.

During non-isothermal crystallization of iPP, the increase of cooling rate on primary melt-crystallization lowers the crystallization temperature and increases the number of nuclei and spherulitic growth rate [120]. This phenomenon leads to a decrease of diameter of spherulites, on increasing the cooling rate from 10<sup>-1</sup> to 10<sup>1</sup> K s<sup>-1</sup>. The formation of non-space filling, isolated spherulites, at an intermediate rate of cooling between 10<sup>1</sup> to 10<sup>2</sup> K s<sup>-1</sup>, indicates the arresting of large-scale molecular mobility, due to

less available time for crystallization, which finally leads to a complete absence of spherulitic superstructure, if the cooling rate is larger than the critical cooling rate.

### ***Lamellar and nodular crystal morphology***

The crystal morphology of iPP is systematically analyzed in a large range of cooling rates on primary melt-crystallization. A transition from a cross-hatched lamellar crystal morphology to a nodular crystal morphology is observed, on increasing the cooling rate from  $10^{-1}$  to  $10^3$   $\text{K s}^{-1}$ , respectively. The transition occurs through a region, where both lamellae and nodules are detected. Figure 33 shows phase-mode AFM-images of iPP melt-crystallized at (a) 0.1, (b) 6, (c) 22, (d) 80, (e) 450, and (f) 750  $\text{K s}^{-1}$ .

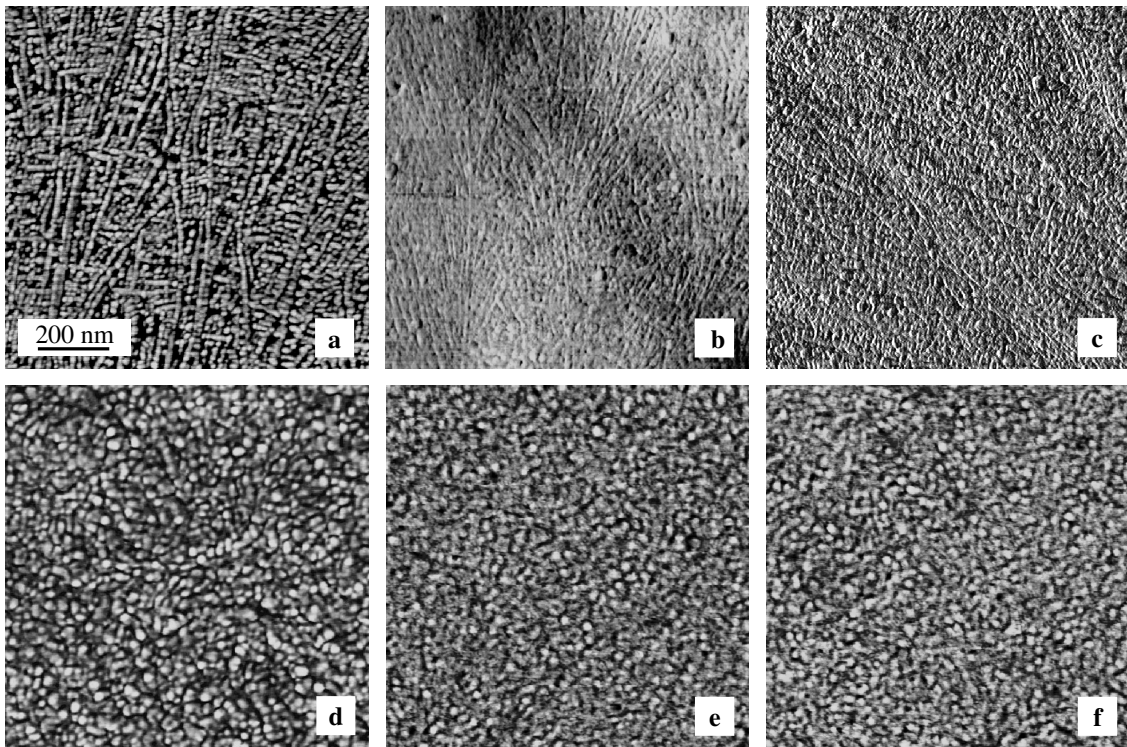


**Figure 33.** Phase-mode AFM-images of iPP melt-crystallized at (a) 0.1, (b) 6, (c) 22, (d) 80, (e) 450, and (f) 750  $\text{K s}^{-1}$ . The scale bar is applicable to all images.

Melt-crystallization at cooling rates between  $10^{-1}$  and  $10^1$   $\text{K s}^{-1}$  triggers the formation of cross-hatched lamellae. Within this range of cooling rates the average thickness of lamellae decreases from about 12 nm at 0.1  $\text{K s}^{-1}$  to about 10 nm at 6  $\text{K s}^{-1}$ . A

cross-hatched lamellar morphology was even detected at a cooling rate less than  $0.1 \text{ K s}^{-1}$ , however, lamellae of thickness larger than 12 nm were observed.

Application of an intermediate rate of cooling, i.e., between  $10^1$  and  $10^2 \text{ K s}^{-1}$ , produces both lamellae and nodules, embedded in an amorphous matrix. The thickness of lamellae decreases to about 8 nm at  $50 \text{ K s}^{-1}$ , whereas the size of nodules of about 20 nm does not change within this range of cooling rates. The coexisting monoclinic lamellae and mesomorphic nodules are the result of two different crystallization events during cooling from the melt. The formation of qualitatively different crystal morphologies by the variation of the rate of melt-crystallization was also observed in a 100 nm thick film of PVDF. Melt-crystallization in air produced lamellar crystals and spherulites [121]. In contrast, replacing of the cooling medium with ice-water or liquid nitrogen produced nodules of size of about 20–30 nm. The coexistence of both nodules and lamellae was detected on quenching in water kept at room temperature. An increase of the size of nodules as well as the thickness of lamellae was observed, if the temperature of the cooling medium, i.e., water, was increased [25].

Finally, melt-crystallization above the critical cooling rate leads to the formation of mesomorphic nodules. Increasing the cooling rate from about  $10^2$  to  $10^3 \text{ K s}^{-1}$  decreases the size of nodules from about 20 nm to about 15 nm, respectively. The instantaneous crystallization of a large number of nodular domains restricts their lateral growth and suggests the formation of a large number of nuclei in a supercooled liquid. It is expected that the instantaneous crystallization results in a random orientation of nodular domains, with respect to each other, in terms of the orientation of main chain axes within nodules.

In order to verify that the surface morphology is not affected by the glass, used as a substrate, iPP films were melt-crystallized between freshly cleaved mica sheets by slow cooling at  $0.1 \text{ K s}^{-1}$  and by quenching in dry ice–ethanol mixture or in liquid nitrogen. Analysis of the crystal morphology by AFM showed a cross-hatched lamellar morphology for a sample melt-crystallized at  $0.1 \text{ K s}^{-1}$  and a nodular crystal morphology for samples either quenched in a dry ice–ethanol mixture or in liquid nitrogen.

### ***Comparison of crystal morphology by AFM and TEM***

In order to collect further evidence that the surface morphology is not affected by the substrate, and to confirm close-to-identical cooling conditions across the film

thickness, a comparison of crystal morphology, obtained by AFM at the surface and by TEM in the bulk, was made. Figure 34 shows the crystal morphology of iPP, melt-crystallized at  $12 \text{ K s}^{-1}$  (top images) and  $750 \text{ K s}^{-1}$  (bottom images). Images in the first and second row were obtained at the surface of iPP films, by using AFM tips of radius of about 10 and 1 nm, respectively, whereas images in the third and fourth row were obtained at the center and near the surface of iPP films, respectively, by TEM, as described in the sketch. The characteristics of an AFM tip (DP 14) of about 1 nm radius (MikroMasch) were identical to that of NSC 14 [122,123].

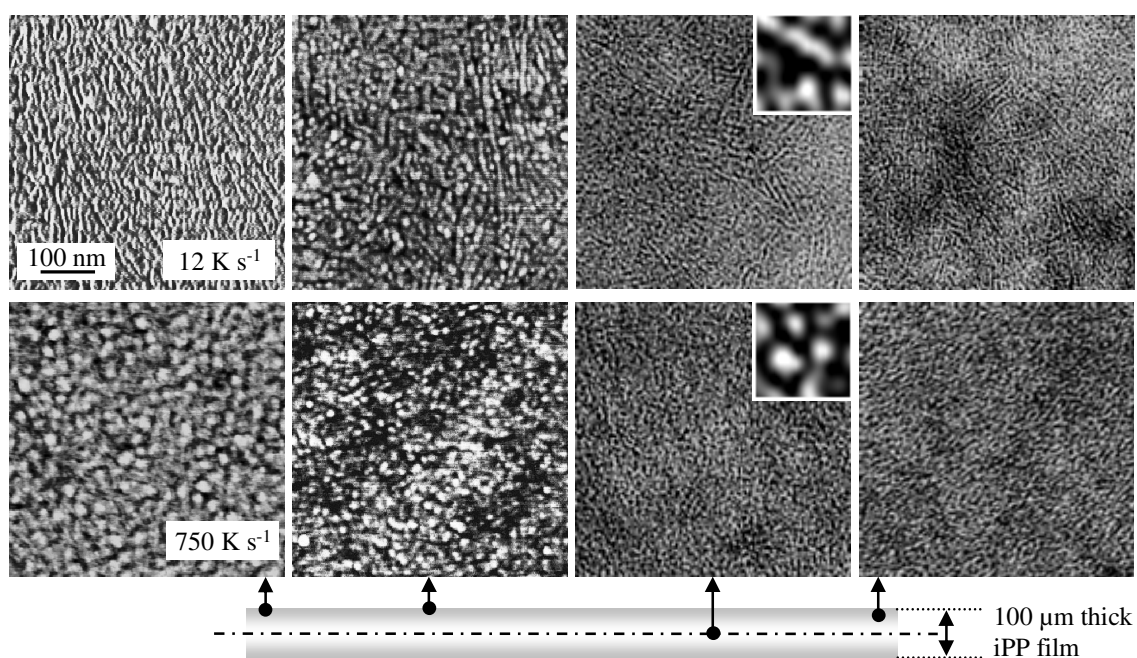


**Figure 34.** Crystal morphology of iPP, melt-crystallized at  $12 \text{ K s}^{-1}$  (top images) and  $750 \text{ K s}^{-1}$  (bottom images). Images in the first and second row were obtained at the surface of iPP films, by using AFM tips of radius of about 10 and 1 nm, respectively, whereas images in the third and fourth row were obtained at the center and near the surface of iPP films, respectively, by TEM, as described in the sketch. Images and insets show an area of  $500 \times 500 \text{ nm}^2$  and  $30 \times 30 \text{ nm}^2$ , respectively.

AFM-image of a sample melt-crystallized at  $12 \text{ K s}^{-1}$  shows lamellae together with few nodules. A similar morphology, i.e., lamellae together with few nodules, was

observed by TEM at center and near the surface of the film. The observed thickness of lamellae of about 5 nm, however, is smaller when analyzed by TEM, in comparison to AFM. Manual estimation of the thickness of lamellae yields values of about 9 and 7–8 nm for AFM tips of radius of about 10 and 1 nm, respectively. Melt-crystallization of an iPP film at  $750 \text{ K s}^{-1}$  resulted in formation of distinctly nodular geometry of the formed domains, in AFM analysis. Similarly, the TEM-images also suggest a nodular geometry of the domains, as can clearly be seen in the inset, independent of the location in the sample. The size of domains is about 15 and 6–8 nm for AFM tips of radius of about 10 nm and 1 nm, respectively, and about 5 nm in TEM micrographs.

Comparison of AFM and TEM-images confirm that the crystal morphology is identical at the surface and in the bulk of an investigated film of thickness of  $100 \mu\text{m}$ , suggesting (a) that the crystallization at the surface is not affected by the use of a glass substrate for preparation, and (b) that the temperature-gradients during primary melt-crystallization of  $100 \mu\text{m}$  thick films are sufficiently small to ensure identical morphology at the surface and in the bulk. AFM suggests a larger size of crystals than TEM, mainly due to two possible reasons, (1) if the absolute size of objects is smaller than the dimensions of the used AFM-tip and (2) due to the presence of RAF that can give an identical mechanical response as that of the crystal, thereby, introducing a larger dimension of the crystal. The use of a smaller AFM tip radius allows to neglect the first reason and, therefore, yields a close-to-identical size of crystals as observed by TEM, since the broadening effect of the tip is minimized in comparison to a tip radius of about less than 10 nm [122,123].

## 6. Thermodynamic stability of lamellar and nodular crystals

### 6.1. Mesomorphic-to-monoclinic phase transition

#### *X-ray structure on heating*

Figure 35 shows the temperature-resolved WAXS pattern of iPP, obtained during heating at  $10 \text{ K min}^{-1}$ , initially melt-crystallized at rates of cooling of (a) 12, (b) 50, and (c)  $750 \text{ K s}^{-1}$ . The curves are shifted for a better visibility. Thick black curves were collected at temperatures of 300, 350, 383 and 432 K.

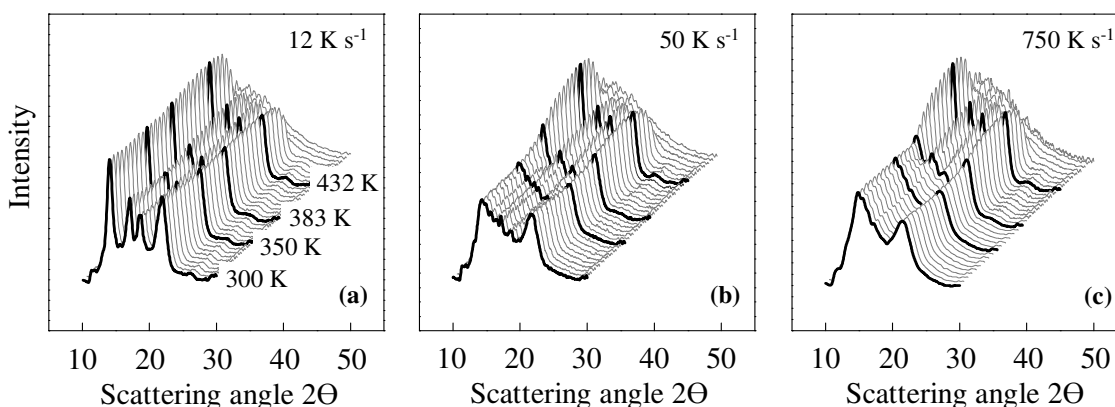


**Figure 35.** Temperature-resolved WAXS of iPP, at a heating rate of  $10 \text{ K min}^{-1}$ , initially melt-crystallized at (a) 12, (b) 50, and (c)  $750 \text{ K s}^{-1}$ .

X-ray scattering at ambient temperature of a sample initially melt-crystallized at  $750 \text{ K s}^{-1}$  is typical of the mesomorphic structure of iPP and shows two halos located at  $2\theta$  values of about  $15^\circ$  and  $21.3^\circ$ . The mesomorphic structure, on heating, starts to convert into monoclinic structure at a temperature of about 350 K, as is evident by the appearance of peaks at  $2\theta$  values of  $16.54^\circ$  and  $18.45^\circ$ , typical of the monoclinic  $\alpha$ -structure. All four peaks are linked to the monoclinic structure, and are well resolved at a temperature of 383 K. The intensity of peaks continues to increase on further heating, due to a considerable reorganization of the structure, indicating an increase of crystallinity. In contrast, melt-crystallization at  $12 \text{ K s}^{-1}$  shows predominantly the crystalline peaks of the monoclinic  $\alpha$ -structure. The crystalline order is well developed in this preparation and as a result of this a major structural reorganization is not detected, at least on heating to a temperature of about 383 K. The reorganization of the structure is only recognized on further heating above the temperature of about 400 K. An intermediate X-ray structure, in

comparison to the structure shown by the samples melt-crystallized at 12 and 750 K s<sup>-1</sup>, is observed on melt-crystallization at 50 K s<sup>-1</sup>. WAXS pattern shows the crystalline peaks of monoclinic structure of iPP but the intensity of peaks is suppressed due to the presence of mesomorphic structure together with amorphous and monoclinic structures.

### ***Thermal analysis by DSC***

The X-ray data is in agreement with the information obtained from DSC analysis of iPP samples of different history of crystallization. Figure 36 (left) shows the change of apparent specific heat capacity of samples melt-crystallized between 6 and 1050 K s<sup>-1</sup> as a function of temperature, during the first heating scan at a rate of 20 K s<sup>-1</sup>. The curves are shifted for a better visibility. The thick black lines represent the heating curves of iPP melt-crystallized at 6 K s<sup>-1</sup> (bottom curve) and 1050 K s<sup>-1</sup> (top curve), with an initial monoclinic and a mesomorphic structure, respectively.

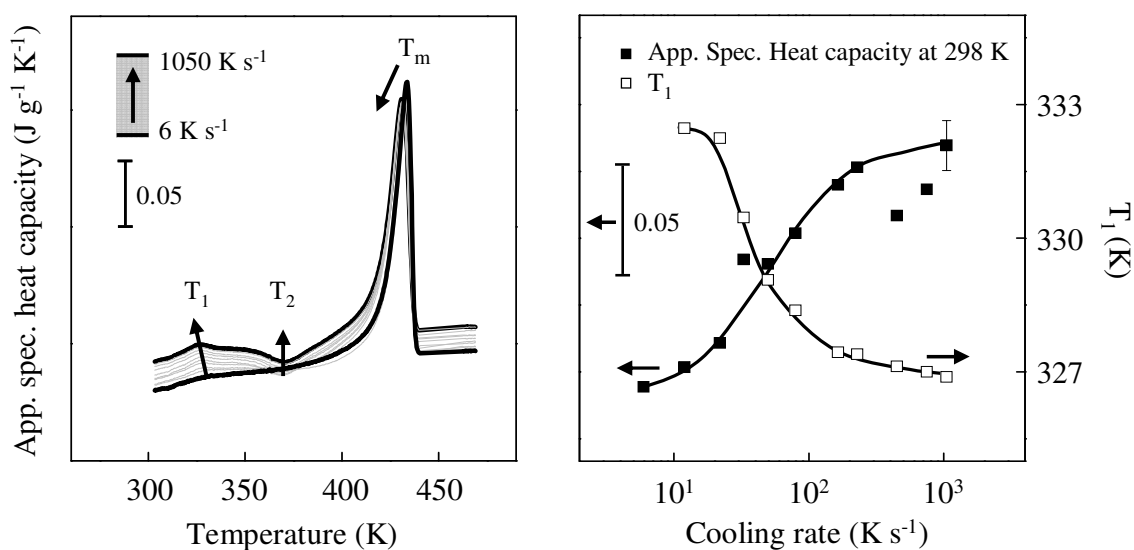


**Figure 36.** Apparent specific heat capacity of iPP of different history of crystallization, as a function of temperature (left) and the change of temperature  $T_1$  (open squares) and of the apparent specific heat capacity, measured at ambient temperature (filled squares), as a function of cooling rate (right).

DSC curve of a monoclinic iPP, obtained on melt-crystallization at 6 K s<sup>-1</sup>, shows the onset of melting above the temperature of 400 K and the final melting peak at a

temperature,  $T_m$ , of about 434 K. In contrast, DSC curve of a mesomorphic iPP, obtained on melt-crystallization at  $1050 \text{ K s}^{-1}$ , shows an endothermic event centered at a temperature,  $T_1$ , of about 327 K, and an exothermic event centered at a temperature,  $T_2$ , of about 370 K. Temperatures  $T_1$  and  $T_2$  are linked to the mesomorphic-to-monoclinic phase transition, in agreement with the previous reports about the DSC analysis of quenched iPP [71,89]. The final melting occurs at about 431 K. The observation of temperatures  $T_1$  and  $T_2$  in iPP, melt-crystallized at a cooling rate larger than about  $10^1 \text{ K s}^{-1}$  confirms the presence of mesomorphic structure.

The temperatures  $T_1$  and  $T_m$  decrease from about 333 to 327 K and from about 434 to 431 K, respectively, with increasing cooling rate, whereas the position of the exothermic peak represented by the temperature  $T_2$  does not change. The cooling run, after first melting, and the subsequent heating run revealed an identical crystallization and melting temperatures of about 112 K and 431 K, respectively, for iPP samples of different initial history of crystallization. In the second heating run, the absence of mesomorphic structure was identified, since temperatures  $T_1$  and  $T_2$  were not observed. The data obtained from WAXS and DSC analysis clearly reveal that the mesomorphic phase changes into monoclinic phase, irreversibly, around a temperature of about 350 K.

The change of temperature  $T_1$  (open squares) and of the apparent specific heat capacity (filled squares) of iPP samples of different history of crystallization, as a function of cooling rate, is shown in Figure 36 (right). The apparent specific heat capacity was determined at 298 K, using a sawtooth-type temperature profile with a programmed amplitude and a period of modulation of 1 K and 120 s, respectively, for a total period of 10 minutes. The change of heat capacity shows an S-shaped curve as a function of cooling rate on primary melt-crystallization. The lowest value of the heat capacity of about  $1.73 \text{ J g}^{-1} \text{ K}^{-1}$  is observed for a sample melt-crystallized at  $6 \text{ K s}^{-1}$ , which increases on increasing the rate of cooling and approaches a maximum value of about  $1.84 \text{ J g}^{-1} \text{ K}^{-1}$  for a sample melt-crystallized at  $1050 \text{ K s}^{-1}$ . The heat capacities of a fully crystalline or a fully amorphous iPP, at a temperature of about 298 K, are about 1.57 or  $2 \text{ J g}^{-1} \text{ K}^{-1}$ , respectively [35]. The experimentally observed values of heat capacities indicate that a completely amorphous or crystalline state of iPP, at ambient temperature, is not possible, within the investigated range of cooling rates. The increase of heat capacity with the increase of cooling rate suggests a decrease of the order of at ambient temperature formed

structure, i.e., a liquid-like structure is approached on increasing the rate of cooling. This also results in a decrease of temperature  $T_l$ . A lower value of temperature  $T_l$  corresponds to a higher value of the apparent specific heat capacity, indicating the onset of mobility of chains within the mesomorphic nodules at lower temperature, i.e., the mesomorphic-to-monoclinic phase transition begins at lower temperature. This observation goes parallel with a lowering of crystallization temperature of mesomorphic phase in glass-crystallized and melt-crystallized samples of iPP, on increasing the rate of cooling of the melt [2,3].

### ***Effect of mesomorphic-to-monoclinic phase transition on crystal morphology***

The mesomorphic-to-monoclinic phase transition, at molecular level, involves the reorganization of randomly arranged left and right handed helices into an ordered array of helices. The process of reorganization may involve the melting of small disordered mesomorphic nodules followed by their re-crystallization into monoclinic lamellar crystals of reduced surface energy or it can occur at local scale within the existing domains without involving the complete melting, thereby, preserving the initial nodular morphology [117,124]. Most recent analysis of the phase transition in mesomorphic iPP by SAXS/WAXS suggests the phase transition to occur by the rearrangement of chains without a complete melting and re-crystallization process [125]. Previous reports also showed that the initially at fast melt-crystallization formed nodular morphology is preserved on heating, however, this conclusion was merely based on the observation of crystal morphology of annealed samples at ambient temperature. Therefore, a direct observation of the change of crystal morphology is required to analyze the effect of phase transition on the shape of crystals.

Figure 37 shows the change of apparent specific heat capacity of iPP (thick line), representative of a sample melt-crystallized at a cooling rate between  $10^2$  and  $10^3$  K s<sup>-1</sup>, with internal mesomorphic structure. Thin solid and dotted lines represent the heat capacities of a fully crystalline and a fully amorphous iPP, respectively, as listed in the ATHAS data bank [35]. The selected WAXS profiles are related to the labeled areas in the DSC curve and demonstrate the structure development on heating. Figure 38 shows a nodular morphology at ambient temperature (left) and during heating (left to right), representative of a sample melt-crystallized at a cooling rate between  $10^2$  and  $10^3$  K s<sup>-1</sup>. Real-time change of the crystal morphology is observed using the hot-stage coupled

atomic force microscopes from Quesant (top images) and from Digital Instruments (bottom images). Two different microscopes are employed in order to increase the reliability of data. The top series of AFM-images is obtained at temperatures of 298, 330, 363 and 396 K (left to right). The insets are soft zooms, which allow to closely monitor the change of crystal morphology on heating. The bottom series of AFM-images are soft zooms of a larger scan size of 1.5  $\mu\text{m}$  and were obtained at temperatures of 298, 353, 403 and 408 K (left to right). The arrows point to an identical location on the sample surface.

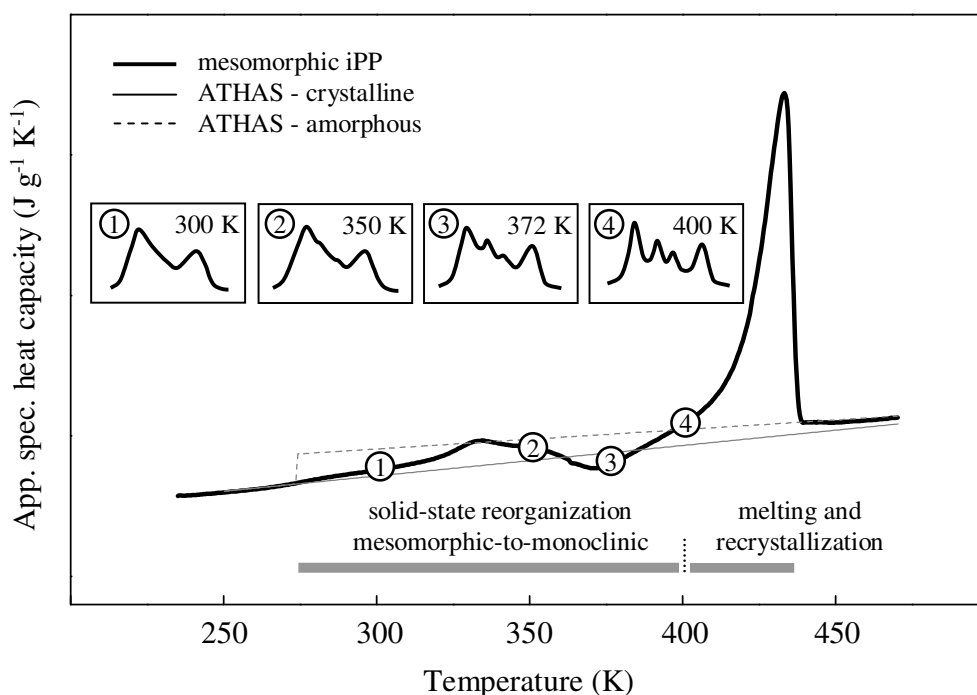


**Figure 37.** Apparent specific heat capacity of mesomorphic iPP, as a function of temperature. Thin solid and dotted lines represent the heat capacities of a fully crystalline and a fully amorphous iPP, respectively. The inserted WAXS profiles are related to labeled areas in the DSC curve.

The mesomorphic iPP at ambient temperature shows nodular domains of size of less than about 20 nm. AFM-images do not show a noticeable change of the crystal size and shape on heating to a temperature of about 350 K, where the characteristic peaks of monoclinic structure already start to appear. Further heating to a temperature of about 400 K reveals well developed X-ray peaks of a monoclinic structure and is connected to a

slight increase of the size of nodules. The preserved quasi-globular shape of domains clearly suggests that the phase transition occurs within the existing domains and is not connected to a complete melting and subsequent crystallization of nodules, i.e., the mesomorphic-to-monoclinic phase transition occurs globally, in solid-state, and changes the mesomorphic nodules into monoclinic nodules of nearly identical geometry. Furthermore, the presented AFM-images, unambiguously, show a complete absence of lamellar crystals both below and above the temperature of the phase transition.

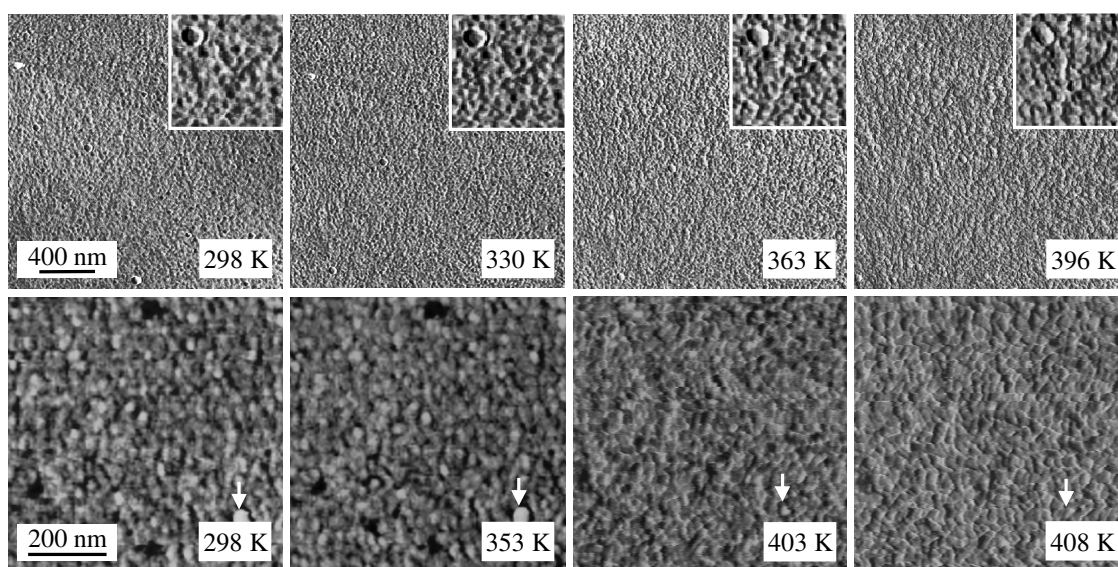


**Figure 38.** *In situ* AFM-images of the change of crystal morphology of initially mesomorphic iPP, with temperature. Images are obtained using atomic force microscopes from Quesant (top series) and from Digital Instruments (bottom series). The size of insets is  $30 \times 30 \text{ nm}^2$ . Arrows point to an identical location on the sample surface.

At molecular level, a mechanism involving the rewinding of helices is suggested, which allows the chains to readjust their handedness to obtain the symmetry of the monoclinic phase [74,77]. A similar mechanism was observed in case of poly(tetrafluoroethylene), where the number of helix reversal was found to be increased with temperature [126], i.e., the process of helix reversal is kinetically controlled. A similar mechanism of helix reversals is likely to occur in iPP, as the translational motion of a chain may not be possible at low temperatures due to the presence of methyl groups.

Therefore, the process of helix reversal must involve the cooperative mobility of the neighboring chain segments inside a nodule to change the random arrangement of left and right handed helices into an ordered monoclinic arrangement.

## 6.2. Reorganization of crystal morphology

### *Control of crystal size*

The crystal morphology of melt-crystallized samples can be further modified by the controlled conditions of subsequent annealing. Figure 39 shows phase-mode AFM-images of iPP melt-crystallized at  $0.1 \text{ K s}^{-1}$  (top) and  $22 \text{ K s}^{-1}$  (bottom) before annealing (left) and after annealing at 393 K (center) and 433 K (right), for a period of 60 minutes.

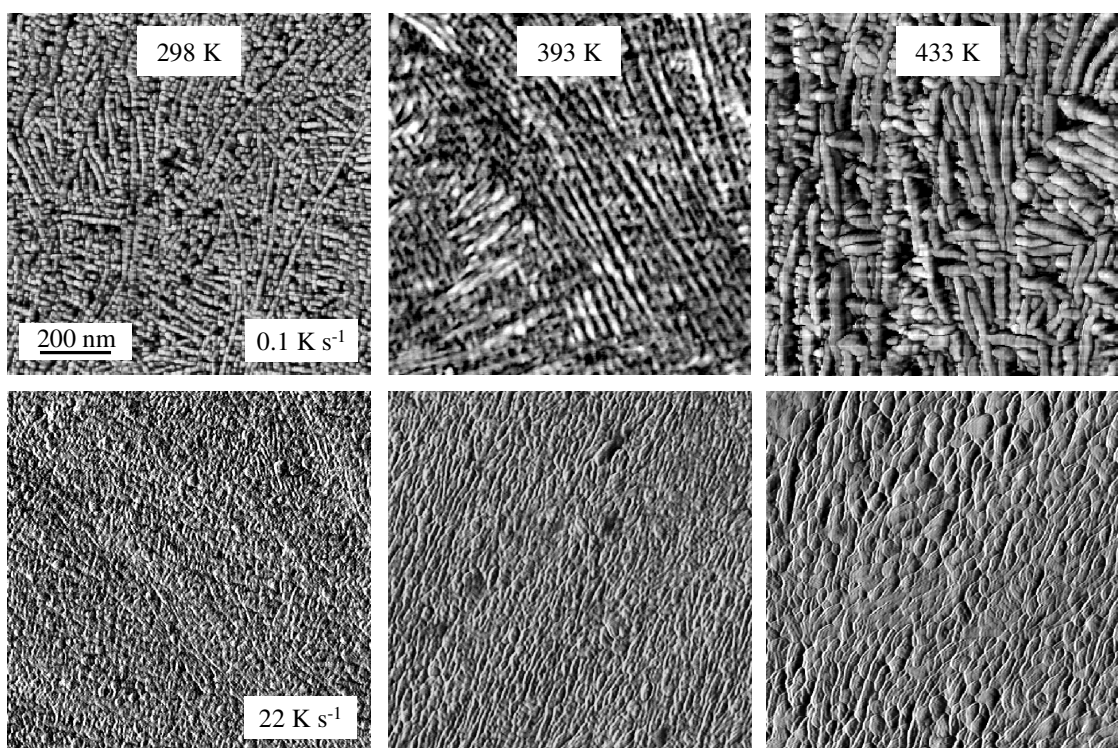


**Figure 39.** Phase-mode AFM-images of iPP melt-crystallized at a rate of  $0.1 \text{ K s}^{-1}$  (top) and  $22 \text{ K s}^{-1}$  (bottom) before annealing (left) and after annealing at 393 K (center) and 433 K (right), for a period of 60 minutes. The scale bar is applicable to all images.

The sample melt-crystallized at  $0.1 \text{ K s}^{-1}$  shows laterally extended cross-hatched lamellae of an initial thickness of about 12 nm. As a result of annealing, the growth of

lamellae primarily occurs in the thickness direction, i.e., in the chain direction. The thickness of lamellae increases to about 18 nm after annealing at 393 K for 60 minutes, and reaches a maximum value of about 26 nm after annealing for an identical period of time at 433 K. Melt-crystallization of iPP at  $22 \text{ K s}^{-1}$  shows a mixed morphology, comprising both lamellae and nodules in an amorphous phase. The size of lamellae and nodules at ambient temperature is about 9 and 20 nm, respectively. As a result of annealing at 433 K for 60 minutes, the size of lamellae and nodules increases to reach a maximum value of about 26 nm and 40 nm, respectively. A further increase of the size of crystals was possible by increasing the time of isothermal annealing. For instance, the thickness of lamellae and nodules was increased to about 31 and 50 nm after annealing for 840 minutes at 433 K. The initially at ambient temperature formed crystal morphology and spherulitic superstructure, in both preparations, were preserved after annealing at 433 K.

Figure 40 shows phase-mode AFM-images of iPP melt-crystallized at  $165 \text{ K s}^{-1}$  (top) and  $450 \text{ K s}^{-1}$  (bottom) before annealing (left) and after annealing at 403, 423 and 433 K (left to right). The images were collected at ambient temperature after annealing.

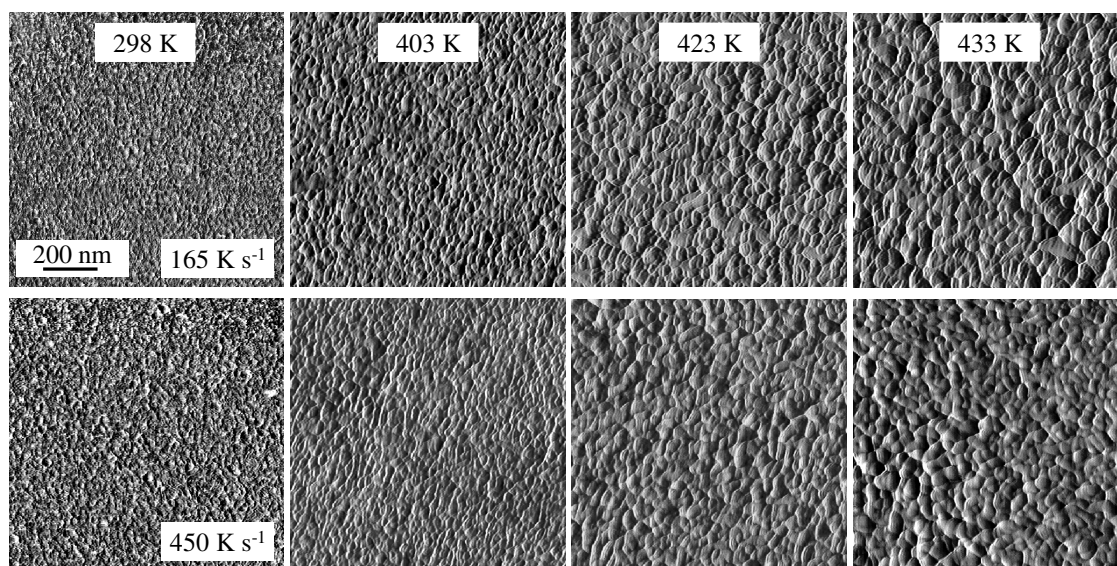


**Figure 40.** Phase-mode AFM-images of iPP melt-crystallized at  $165 \text{ K s}^{-1}$  (top) and  $450 \text{ K s}^{-1}$  (bottom) before annealing (left) and after annealing at 403, 423 and 433 K (left to right), for a period of 60 minutes. The scale bar is applicable to all images.

In both preparations, the size of nodules obtained at ambient temperature is less than about 20 nm. Isothermal annealing at elevated temperature stabilizes the nodular domains by their growth in chain direction and cross-chain direction, which in turn increases the size of crystals. For instance, the crystal size of about 40 nm is observed after annealing at 433 K for 60 minutes, for both preparations, whereas the initial quasi-globular shape was maintained. The increase of size of crystals is also connected to a decrease of the number of nodules per micrometer square. Nodule count was made manually, which shows an average decrease of the number of nodules from above about 1000 before annealing to below about 300, after annealing at 433 K for 60 minutes.

The size of lamellae (left) and nodules (right) of iPP of different history of crystallization, as a function of annealing temperature is shown in Figure 41.

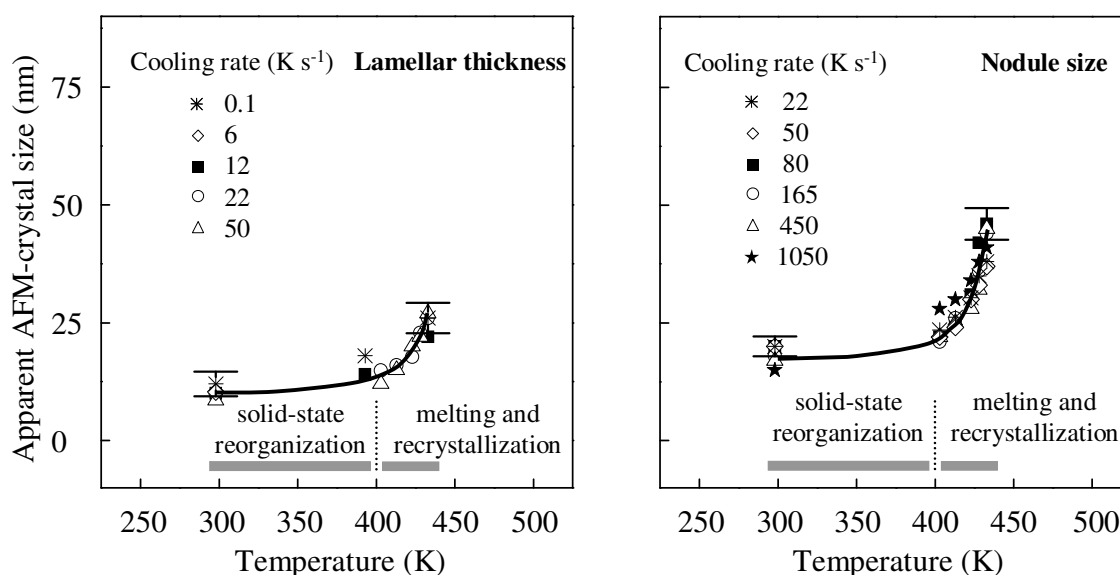


**Figure 41.** Size of lamellae (left) and nodules (right) as a function of annealing temperature for samples of different history of crystallization. Annealing time, for each annealing temperature, is 60 minutes.

Annealing at temperatures below about 400 K involves a solid-state reorganization and is connected to a slight increase of the size of crystals. A two-fold increase of the size of crystals is observed, at annealing temperatures above about 400 K, which involves a melting and re-crystallization process. Most importantly, the increase of the size of

initially at primary melt-crystallization formed lamellar and/or nodular crystals follows an identical non-linear path as a function of the temperature of annealing, independent of the history of melt-crystallization. Also, the initial differences between the lamellae of different thickness or the nodules of different size due to different history of crystallization are minimized after annealing at temperatures close to final melting.

### ***Mechanism of secondary crystallization***

The most striking difference of the growth of lamellae and nodules, as result of secondary crystallization on annealing, is that the lamellae grow primarily in the thickness direction and the nodules grow in all directions. In case of lamellae, the thickness increases from about 10 nm at ambient temperature to above 20 nm, after annealing at 433 K. As a major mechanism, diffusion of chain segments through the crystals and increased chain mobility in the amorphous phase, on annealing, assists the structural reorganization into thermodynamically more stable and thicker crystals [127]. The segmental mobility or diffusion of chain segments through the crystal can involve the motion of a point dislocation [128] or the motion of entire segments of a molecule along the chain direction within the lamellae [129] and the partial melting of the initial lamellae and re-crystallization into thicker lamellae [130], through a translational motion of polymer chains [131]. Primarily, the former mechanism is considered responsible for lamellae thickening, in case, the annealing temperature is well below the final melting temperature, as reported in case of annealing of poly(acrylonitrile), at temperatures below about 453 K [132]. The latter mechanism is activated on annealing in the temperature range of final melting that strongly increases the thickness of lamellae. This behavior is observed in many semicrystalline polymers [18], including iPP [48,133,134]. Additionally, the crystallization of amorphous phase can also occur on annealing, whose fraction decreases with increasing the annealing temperature and/or annealing time [135]. The observed morphological data of the present study shows that the lamellae thickening of iPP below an annealing temperature of about 400 K is the result of solid-state reorganization. The classical melting and re-crystallization starts above an annealing temperature of about 400 K, as is evident by the onset of melting in DSC analysis, which strongly increases the thickness of lamellae due to complete/partial melting and recrystallization of initially formed thin lamellae into stable and thicker lamellae.

Figures 42a and 42b schematically describe the formation of monoclinic nodules of increased size from the initially formed mesomorphic domains. Fast cooling from the melt produces the mesomorphic nodules of different size, at ambient temperature. A general assumption to explain the crystal thickening in chain direction would be the existence of molecular disorder within mesomorphic domains and at the crystal basal planes, providing a driving force for the structural reorganization. Growth in cross-chain direction is facilitated by the crystallization of chain segments, with a favorable conformation, at a lateral surface of nodules.

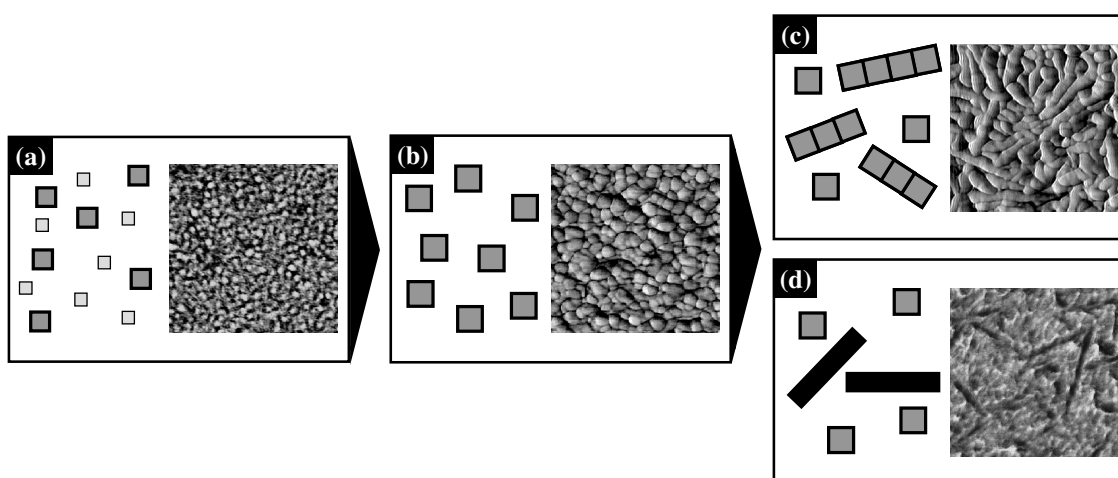


**Figure 42.** Schematic shows (a) the mesomorphic nodules (b) monoclinic nodules, obtained on subsequent annealing at 433 K, and the formation of lamellae by (c) the coalescence of nodules and by (d) a melting and re-crystallization process.

In the region of melting and recrystallization, the melting of unstable, smaller and more defective nodules, not stable at the temperature of annealing, can occur. This increases the amount of liquid, which can crystallize at the lateral surface of existing nodules, a crystallization path that involves lower energy barrier. Simultaneously, the translational motion of chains can occur at higher annealing temperature, which increases the crystal size in chain direction. The preservation of the quasi-globular shape of crystals, on annealing in the region of melting and re-crystallization, indicates a simultaneous growth in chain and cross-chain direction. The presented explanation is well supported by an in-depth X-ray analysis of initially quenched iPP, which allowed to

identify two ranges of annealing temperatures where the major structural reorganization processes are active. The first range of annealing temperatures identified was between 343 and 353 K, which mainly involved rearrangement in the chain direction and the second range of annealing temperatures was between 353 and 423 K, which involved the rearrangement in both chain direction and cross-chain direction [91].

The formation of lamellae of different types was only detected after annealing at a temperature of 433 K, as shown in Figures 42c and 42d. The formation of lamellae, which seem to be composed of aligned nodules, as shown in Figure 42c, is explained by the coalescence of mobile and stable nodules, for reduction of the surface free energy. Lamellae formed in this way are identified by their distinct blocky structure. The mobility of nodules, stable at 433 K, can increase as a result of melting of unstable nodules. The evidence of melting of unstable monoclinic nodules is provided by the onset of melting in the DSC analysis at a temperature of about 410 K. Melting increases the fraction of amorphous liquid and removes local stress within the liquid phase. This process may even include rotation of crystals or positioning of specific crystal faces, for reason of maximum decrease in surface energy, when getting in contact with a neighboring crystal. Lamellae formed in this way show an identical thickness as nodules. Occasionally, isolated lamellae were also observed, as shown in Figure 42d, formed as a result of annealing at identical temperature of 433 K and coexisting with large and non-aligned nodules. These isolated lamellae apparently do not show a blocky structure and are formed by regular crystallization from the melt, supported by former melting of unstable nodules. The thickness of lamellae, in this case, is smaller than the thickness of nodules.

### ***Comparison of crystal morphology by AFM and TEM***

Figure 43 show the crystal morphology of iPP, initially melt-crystallized at a cooling rate of  $750 \text{ K s}^{-1}$ , after annealing at 393 K (top images) and 433 K (bottom images), for a period of 60 minutes. Images in the first and second row were obtained at the surface of iPP films, by using AFM tips of radius of about 10 and 1 nm, respectively, whereas images in the third and fourth row were obtained at the center and near the surface of iPP films, respectively, by TEM, as described in the sketch [122,123]. The morphology of the specimen, before annealing, is nodular. After annealing at 393 K, AFM suggests a slight increase of the size of crystals from initially about 15 nm to about

20–25 nm, for an AFM tip of radius of about 10 nm, with the overall geometry/shape of domains almost unchanged. A similar observation is made for an AFM tip of radius of about 1 nm, however, quantitatively the size of crystals increases from initially about 6–8 nm to about 15 nm after annealing. The corresponding TEM-image support the preservation of the shape of crystals and reveals the crystal size, which is in good approximation with the size suggested by an AFM tip of about 1 nm radius. Though a quantitative analysis of TEM-crystal size is complicated, since crystals apparently are not isolated, however, the dimensions seem to be smaller than 20 nm.

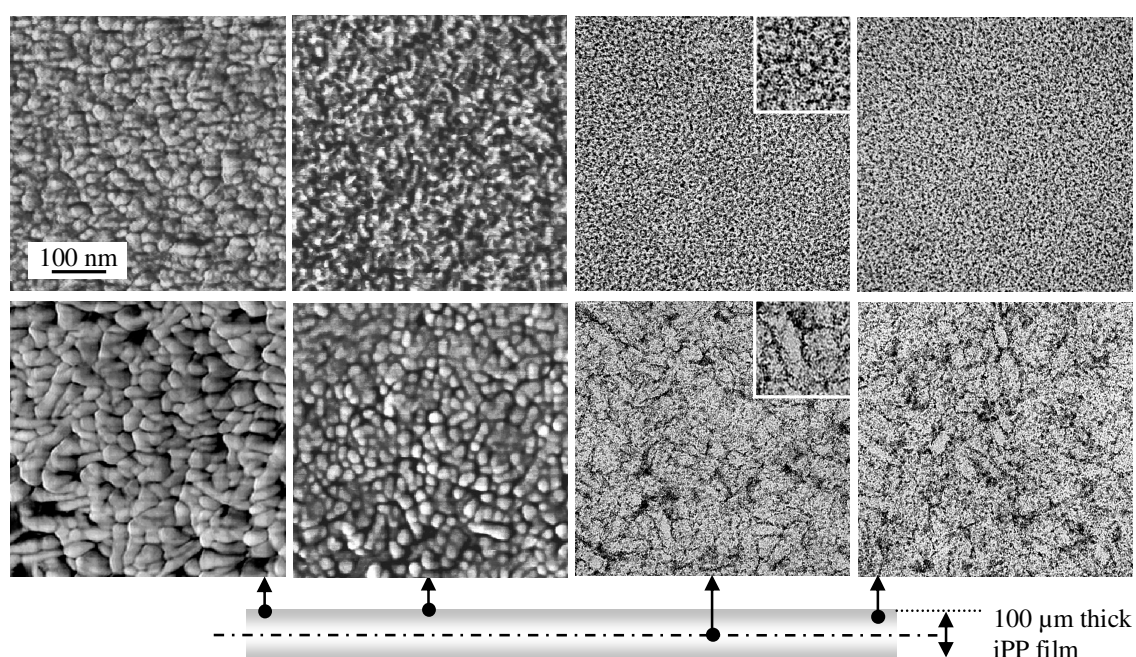


**Figure 43.** Crystal morphology of iPP, melt-crystallized at  $750 \text{ K s}^{-1}$ , after annealing at  $393 \text{ K}$  (top images) and  $433 \text{ K}$  (bottom images), for a period of 60 minutes. Images in the first and second row were obtained at the surface of iPP films, by using AFM tips of radius of about 10 and 1 nm, respectively, whereas images in the third and fourth row were obtained at the center and near the surface of iPP films, respectively, by TEM, as described in the sketch. Images and insets show an area of  $500 \times 500 \text{ nm}^2$  and  $30 \times 30 \text{ nm}^2$ , respectively.

Isothermal annealing at 433 K for 60 min (bottom row), reveals an increased aspect ratio and size of crystals in both AFM and TEM analysis. Isolated nodules and lamellae

composed of aligned nodules can be identified. The shorter dimension of crystals is about 30–35 nm in an AFM-image obtained by using a tip radius of about 10 nm. A smaller tip radius of about 1 nm yields the crystal size of about 25 nm, which is identical to the crystal size obtained by TEM [122,123].

### 6.3. Crystal morphology and phase fractions

Figure 44 shows the enthalpy-based crystallinity and the rigid amorphous fraction of iPP at room temperature, as a function of the rate of cooling on primary melt-crystallization. The fraction of different phases is calculated from temperature-dependent apparent-specific-heat-capacity data. Reference values of specific heat capacity of liquid and solid iPP, and of specific heat of fusion, were taken from the ATHAS data base [35].

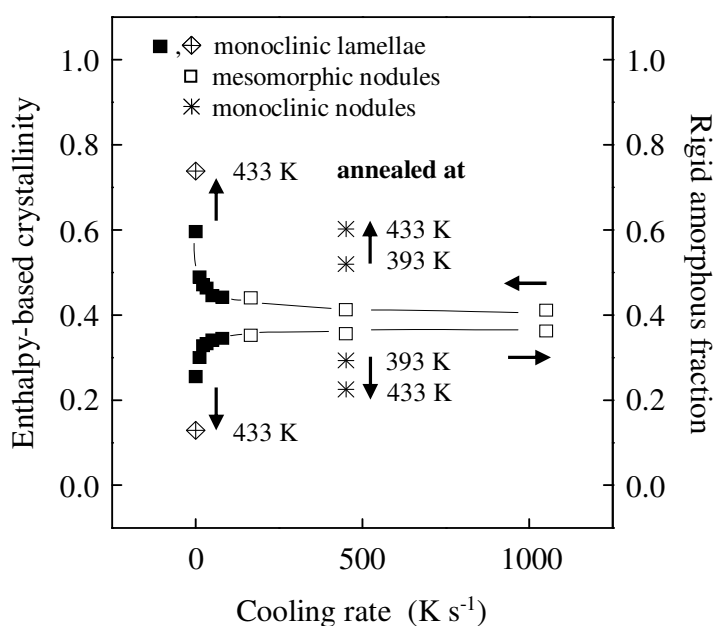


**Figure 44.** Enthalpy-based crystallinity and rigid amorphous fraction of iPP, as a function of cooling rate on primary melt-crystallization. The filled and open squares represent data of non-annealed samples containing lamellae and nodules, respectively. Cross-filled diamonds and stars represent the effect of annealing for selected samples.

The crystallinity decreases, as expected, with increasing cooling rate on melt-crystallization due to increasing kinetic restriction of the diffusion-controlled

crystallization process. Slow melt-crystallization at a rate of  $0.1 \text{ K s}^{-1}$  results in an enthalpy-based crystallinity of about 60 %. The crystallinity decreases to about 40 % on increasing the cooling rate to about  $10^2 \text{ K s}^{-1}$ . The decrease of crystallinity is connected to a simultaneous increase of rigid amorphous fraction. Sample melt-crystallized at  $0.1 \text{ K s}^{-1}$  represents a rigid amorphous fraction of about 25 %, which increases to about 36 % on increasing the cooling rate to about  $10^2 \text{ K s}^{-1}$ . A further increase of the cooling rate is connected with changes of (a) the crystal habit from lamellae to nodules, and (b) the superstructure from spherulitic to non-spherulitic. The enthalpy-based crystallinity and rigid amorphous fraction remain at constant values of about 40 % and 36 %, respectively, if the cooling rate is between about  $10^2$  and  $10^3 \text{ K s}^{-1}$ , which is paralleled by the observation of identical crystal morphology, i.e., nearly identical size and habit of nodules. Annealing at elevated temperature, results in an increase of crystallinity and a simultaneous decrease of rigid amorphous fraction, which is illustrated for selected samples in Figure 44, with the cross-filled diamonds and star-symbols. The crystallinity of iPP, which initially was crystallized on slow cooling at  $0.1 \text{ K s}^{-1}$  increases from 60 % to 70-75 %, by annealing at 433 K for a period of 60 min (cross-filled diamond). Consequently, the rigid amorphous fraction decreases to about 12 % after annealing at identical conditions. Annealing of a nodular preparation (open squares) at a temperature of 433 K for 60 minutes increases the crystallinity from an initially about 40 to 60 % (star symbols) and decreases the rigid amorphous fraction from about 36 to 22 % [136].

#### **6.4. Annealing kinetics – correlation of AFM and DSC data**

AFM-images of iPP, initially melt-crystallized at  $80 \text{ K s}^{-1}$  (top) and  $750 \text{ K s}^{-1}$  (bottom), obtained after isothermal annealing at a temperature of 393 K for 60, 440, 560, and 840 min (left to right), are shown in Figure 45. The size of nodules increases on isothermal annealing at 393 K and simultaneously is observed a decrease of number of nodules from about 1000 to about 400 nodules per micrometer square, on increasing the time of isothermal annealing from 60 to 840 minutes, respectively. AFM-images of the structure evolution of iPP, initially melt-crystallized at  $80 \text{ K s}^{-1}$  (top) and  $750 \text{ K s}^{-1}$  (bottom), obtained after isothermal annealing at a temperature of 433 K for 60, 440, 560, and 840 min (left to right), are shown in Figure 46. Considerably larger domains are formed on annealing at 433 K, in comparison to the annealing at 393 K.

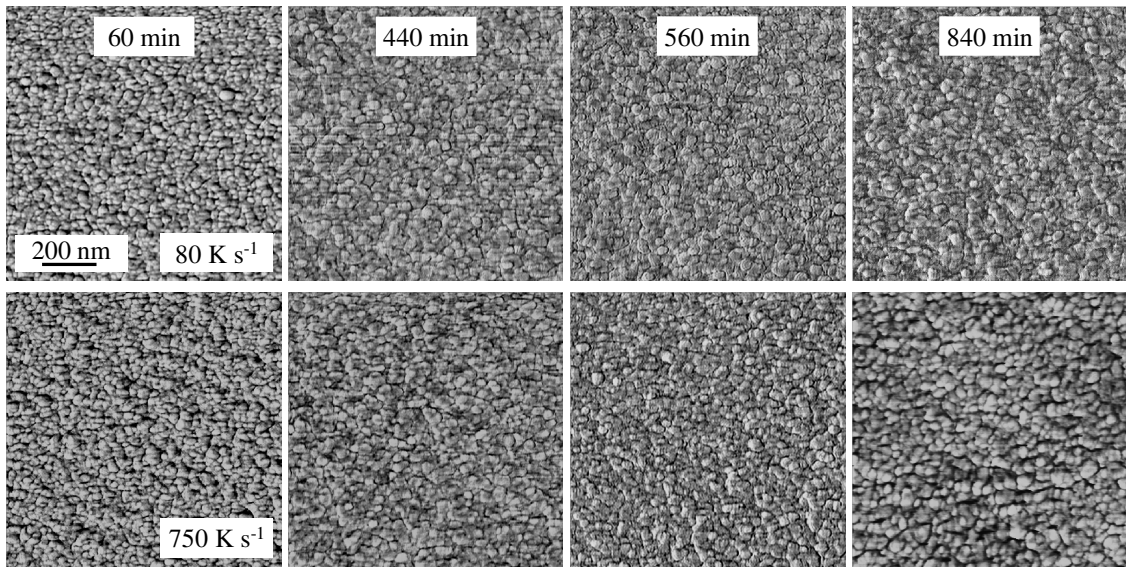


**Figure 45.** AFM-images of iPP, initially melt-crystallized at  $80 \text{ K s}^{-1}$  (top) and  $750 \text{ K s}^{-1}$  (bottom), obtained after isothermal annealing for 60, 440, 560, and 840 min (left to right), at a temperature of 393 K. The scale bar is applicable to all images.

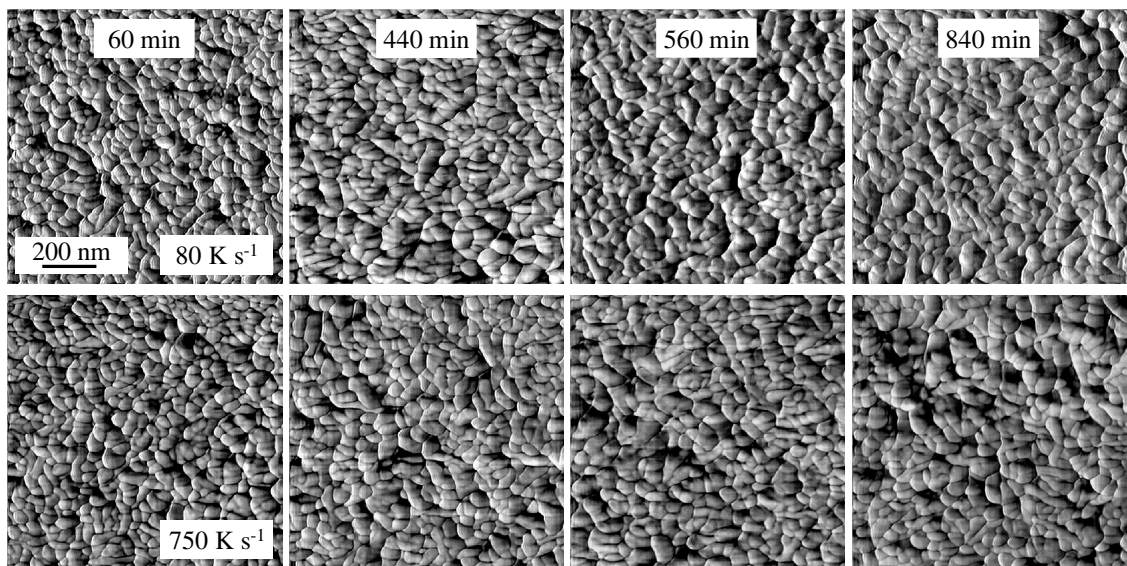


**Figure 46.** AFM-images of iPP, initially melt-crystallized at  $80 \text{ K s}^{-1}$  (top) and  $750 \text{ K s}^{-1}$  (bottom), obtained after isothermal annealing for 60, 440, 560, and 840 min (left to right), at a temperature of 433 K. The scale bar is applicable to all images.

As a result the number of crystals decrease from about 300 to about 200 nodules per micrometer square, after increasing the annealing time from 60 to 840 minutes, respectively. Furthermore, a slight change of the shape of crystals in lateral direction is observed. This minor change of the crystal habit goes along with tendency of aggregation of nodules to form larger objects, which eventually are considered as lamellae [137].

Analysis of AFM-images allows to determine the change of the size of nodules as a function of the time of isothermal annealing, as demonstrated in Figure 47 (left). The open and filled symbols are data obtained on the samples, which initially were melt-crystallized at  $80 \text{ K s}^{-1}$  and  $750 \text{ K s}^{-1}$ , respectively. The diamonds represent annealing at 393 K and squares represent annealing at 433 K. The lines are included to guide the eye.

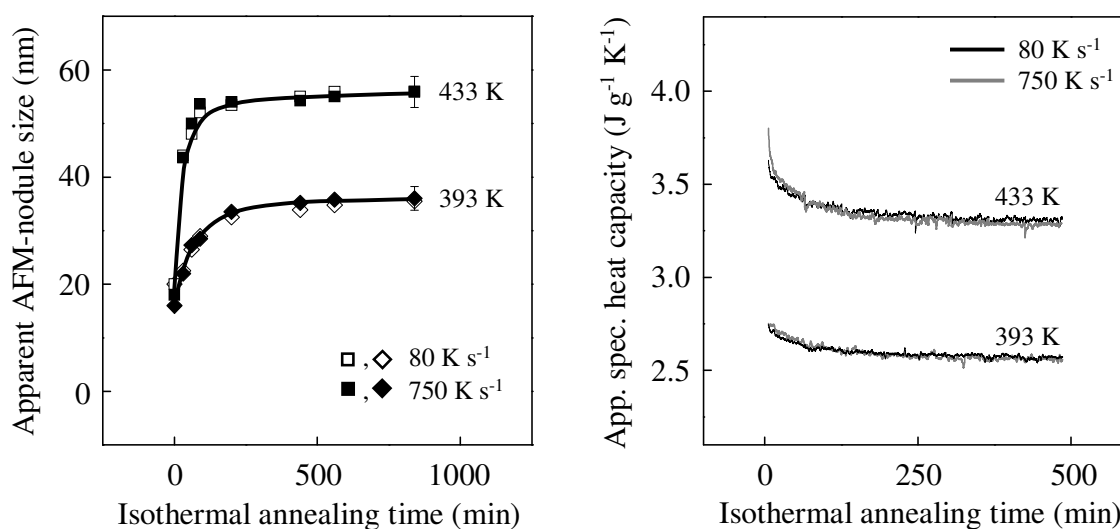


**Figure 47.** Size of nodules (left) and the apparent specific heat capacity (right) of iPP, initially melt-crystallized at  $80 \text{ K s}^{-1}$  and  $750 \text{ K s}^{-1}$ , as a function of the time of isothermal annealing at 393 and 433 K.

A nearly two-fold increase of the size of nodules is observed, as a result of annealing at 393 K, where the size of nodules increases from an initial value of about 20 nm at ambient temperature to a final value of about 35 nm, after annealing for a period of 840 minutes. In contrast, annealing at 433 K results in a nearly three-fold increase of the size of crystals, since a value of about 55 nm is observed, after annealing for an identical period of time. In both cases, the approach of the final structure is non-linear.

Furthermore, the conditions of primary melt-crystallization show no effect on the time-evolution of the size of nodules, on isothermal annealing. Therefore, the data obtained on the samples, which were cooled at  $80 \text{ K s}^{-1}$  (open symbols) and  $750 \text{ K s}^{-1}$  (filled symbols) fit a single curve. The change of the size of crystals shows that the largest changes of the nodular morphology are observed in the initial stage of the annealing process. A fast reorganization of the structure is followed by a considerably slower process, which leads only to a minor additional increase in the crystal dimensions [137]. Despite the general time dependence of the isothermal reorganization process of semicrystalline polymers, containing lamellar crystals, is known [138], qualitatively a similar time dependence of the isothermal annealing of the non-lamellar crystals of the present study is not expected, because of the different thermodynamic stability [139].

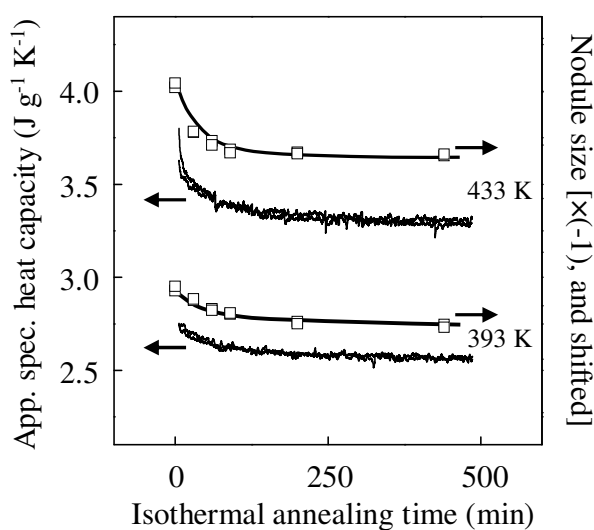
The presented model of structure reorganization includes, based on the experimental data, initial existence of crystals of low thermodynamic stability/melting temperature. These relatively unstable crystals melt on heating and recrystallize subsequently at the annealing temperature at surfaces of the existing crystals, which accounts for the initial strong increase in the crystal dimensions in the first minutes of the isothermal annealing procedure. The large number of domains/crystals, produced on initial melt-crystallization at about 300 K, leads to spatial restrictions and limits the lateral growth of crystals. Therefore, a minor but distinct change of the aspect ratio of crystals is observed, as is documented with the non-isotropic geometry of nodules after annealing at 433 K. Since the number of crystals, melted on prior heating, increases with temperature, the initial increase in the crystal size and change of the crystal shape is more distinct on annealing at 433 K. The process of fast re-crystallization of liquid is followed by minor and slow continuation of crystal growth. Most striking on long-term annealing is the observed aggregation of crystals.

Figure 47 (right) shows the apparent specific heat capacity of iPP as a function of the time of isothermal annealing at 393 and 433 K. The black and gray lines were observed for the samples, which initially were melt-crystallized at a rate of cooling of 80 and  $750 \text{ K s}^{-1}$ , respectively. The apparent specific heat capacity decreases during annealing as a function of time due to irreversible reorganization of the structure, to approach a final constant value after about 500 min. The data obtained on the two samples of different history of initial melt-crystallization are indifferent, similar as in the

case of analysis of the size of nodules, as shown in Figure 47 (left). Recording of the data started after an initial, internal calibration for a period of three modulation cycles, i.e., 6 minutes, requested by the instrument. Since the apparent specific heat capacity decreases continuously with increasing time of isothermal annealing, the initial values between 0 and 6 min are even larger than the first recorded data. Comparison of the data sets obtained on annealing at 393 and 433 K suggests that the amount of irreversible reorganization of the structure is larger at higher temperature, since the relative decrease in the apparent specific heat capacity is more distinct. The final apparent specific heat capacity after completed irreversible reorganization is larger in case of isothermal annealing at 433 K, if compared with the final value obtained after annealing at 393 K. The reason is two-fold. The vibrational heat capacity contribution to the apparent specific heat capacity increases with temperature, as it is documented in the ATHAS data base [35]. Furthermore, the final value of the apparent specific heat capacity is affected by reversible crystallization and melting [69,140]. The amount of reversible crystallization and melting during temperature modulation, at a given constant temperature, is proportional to the amount of preceding irreversible crystallization, melting, or reorganization at an identical temperature [141]. Since the amount of irreversible change of structure is larger at 433 K, as is concluded from the magnitude of prior decrease of apparent specific heat capacity during annealing, therefore, the degree of reversible crystallization and melting is also larger.

The time dependence of the increase of size of nodules and the decrease of apparent specific heat capacity show a strong correlation. In Figure 48, the data of Figure 47 are re-plotted such that a direct comparison is possible. The values of the size of nodule were multiplied by (-1), and subsequently shifted vertically for easy recognition. No distinction is made between the samples of different history of crystallization, as the evolution of the size of nodules and the decrease of apparent specific heat capacity is independent of the initial history of melt-crystallization. The decrease in apparent specific heat capacity goes parallel with the observed change of the size of nodules. This holds for the initial part as well as for the later stage of the annealing process. The initial decrease in the apparent specific heat capacity is considerably larger on annealing at 433 K, compared to the annealing at 393 K. The apparent specific heat capacity decreases within the analyzed range of time between 6 and 485 min by about  $0.2 \text{ J g}^{-1} \text{ K}^{-1}$  [ $\approx 2.75$  to  $2.56 \text{ J g}^{-1} \text{ K}^{-1}$ ]

during annealing at 393 K, and by about  $0.4 \text{ J g}^{-1} \text{ K}^{-1}$  [ $\approx 3.70$  to  $3.32 \text{ J g}^{-1} \text{ K}^{-1}$ ] during annealing at 433 K. The different final values of the apparent specific heat capacity of  $2.56$  and  $3.32 \text{ J g}^{-1} \text{ K}^{-1}$ , after annealing at 393 and 433 K, respectively, are due to, (a) the temperature dependence of the vibrational specific heat capacity [35], and (b) different amounts of reversible melting [69]. A major decrease of the apparent specific heat capacity is observed within the first 200 min, and then the curves go almost parallel.



**Figure 48.** Apparent specific heat capacity and nodule size, re-calculated as described in the text, as a function of the time of isothermal annealing at 393 and 433 K.

In a previous TMDSC study on the annealing process in polyethylene, the modulated heat-flow rate was analyzed in the time domain which led to the conclusion that at least in the initial part of the annealing process the increased apparent heat capacity is mainly due to exothermic heat flow [142]. Now, with the AFM observations of the present study it can be concluded that the exothermic heat flow is connected with an increase of crystal size. Annealing at 393 K produces less heat of crystallization than annealing at 433 K, as can directly be concluded from different offsets of the apparent specific heat capacity of about  $0.2$  and  $0.4 \text{ J g}^{-1} \text{ K}^{-1}$ , respectively, above the final value after extrapolating to infinite annealing time. This is in excellent agreement with the much reduced increase of the crystal size, after annealing at 393 K. The continued

decrease in the apparent specific heat capacity after about 200 min is difficult to link to a specific reorganization process, which may not be due to the process of aggregation, which is the major microscopic observation, at least on annealing at 433 K [137].

Furthermore, the decrease in the apparent specific heat capacity is also obtained on long-term annealing of laterally extended lamellae, which do not aggregate as nodules. The continued minor decrease in the apparent heat capacity may be caused by continued secondary crystallization, i.e., by continuation of the same process which is responsible for the initial strong decrease, or by crystal perfection that is not accessible by microscopy. Comparison of the annealing process of iPP, which contained either lamellar or nodular crystals, revealed that the kinetics is almost indifferent. The presented data confirm that annealing of nodular crystals is controlled by identical mechanisms, from calorimetric point of view [137].

### **6.5. Thermodynamic stability of nodular crystals**

The thermodynamic stability of crystals of iPP of largely different geometry is estimated by their temperature of melting. Samples, with lamellae or nodules, obtained on melt-crystallization at 6 or 750 K s<sup>-1</sup>, respectively, were heated to an annealing temperature of 433 K, isothermally annealed for a period of 60 min, cooled to 298 K at a rate of 20 K min<sup>-1</sup>, and finally melted at identical rate of temperature-change by heating to 473 K. The annealing temperature of 433 K was not chosen arbitrarily, rather was selected such that reorganization between the annealing temperature and final melting is minimized, or even completely suppressed. With this assumption, a direct relation between crystal morphology and melting temperature is established, in order to estimate the thermodynamic stability of crystals of different shape.

The upper two curves in Figure 49a show the approach of annealing temperature to 433 K, for samples with lamellae (black line) and nodules (gray line), respectively. The lower two curves show the final melting after annealing at 433 K, and cooling to 298 K. The sample which contains monoclinic lamellar crystals is characterized by the absence of phase transitions on heating to the annealing temperature of 433 K. The heating scan of the sample, which initially contains mesomorphic domains, indicates reorganization, including the phase transition from the mesomorphic structure to the monoclinic structure. The melting of the initial crystal starts at about 410-415 K, as indicated by the

arrow in Figure 49a, regardless the initial crystal structure and crystal morphology. After annealing, the samples were cooled to ambient temperature. It is not expected that cooling and reheating of the annealed samples, at least up to the temperature of annealing, cause further irreversible structural changes. Heating of the reorganized structures (lower two curves) proves close-to-identical temperatures of melting of about 446 K for both preparations, indicating a similar thermodynamic stability of crystals of largely different shape, formed along different thermodynamic pathways.

According to the Gibbs-Thomson equation, the melting temperature of a crystal,  $T_m$ , depends on the bulk specific heat of fusion,  $\Delta h_f$ , the crystal dimensions in lateral direction,  $a$  and  $b$ , and in longitudinal direction,  $l_c$ , the equilibrium melting temperature,  $T_m^o$ , and the surface free energies of the lateral surfaces and basal planes,  $\sigma$  and  $\sigma_e$ , respectively, as shown by equation below:

$$T_m = T_m^o \left[ 1 - \frac{2}{\Delta h_f} \left( \frac{\sigma}{a} + \frac{\sigma}{b} + \frac{\sigma_e}{l_c} \right) \right] \quad (9)$$

Equation 9 indicates that melting of an infinitely large crystal occurs at  $T_m^o$ . The melting point depression is caused by the increase of free enthalpy of crystals due to the presence of surfaces. The total surface free energy of a crystal depends on the area and corresponding specific surface free energies of all crystal faces. The bulk specific heat of fusion and the equilibrium melting temperature are considered as being identical for the lamellar and nodular structures. This assumption is justified, since the X-ray scans prove exclusive existence of monoclinic crystal structure, after annealing at 433 K. The structure and therefore the free energy of the lateral surfaces are suggested to be independent on the pathway of crystallization. In case of the basal planes, differences between the surface free energies cannot be excluded since it is proven that the path of crystallization affects the number of molecules, which enter or leave the crystal at this particular surface. An increased tendency of formation of folds in initially slowly melt-crystallized iPP is expected, whereas regular folding may not be possible on crystallization at fast cooling, i.e., at high supercooling. For further discussion of the

experimentally observed identical melting temperatures of lamellar and nodular crystals, model calculations are performed, using the Gibbs-Thomson equation.

Figure 49b shows the melting temperature of monoclinic iPP crystals of different thicknesses and surface structures, as a function of the crystal lateral size. The following values are used for the calculations:

$$T_m^o = 460.7 \text{ K [143,144]}, \Delta h_f = 207 \text{ J g}^{-1} \text{ [143]}, \sigma = 1.15 \times 10^{-6} \text{ J cm}^{-2}, \sigma_{e, \text{ fold}} = 7 \times 10^{-6} \text{ J cm}^{-2}, \sigma_{e, \text{ non-fold}} = 24.7 \times 10^{-6} \text{ J cm}^{-2} \text{ [145]}.$$

Lateral dimensions of the crystals are assumed to be identical, i.e.,  $a = b$ . The top and center curves are calculated for folded-chain crystals of thickness of about 40 nm (top) and 25 nm (center), and the bottom curve is calculated for a non-fold crystal of thickness of about 40 nm. With these curves it is possible to estimate the melting temperatures of the nodular and lamellar crystals, with geometry as was obtained after annealing at 433 K and cooling to room temperature, by AFM, as shown in Figures 49c and 49d. Crystals with a non-fold-surface are expected to melt at 427 K. In case of a regular fold-surface, the melting temperature increases almost to 448 K. The observed thickness of lamellar crystals, obtained by rather slow cooling of the melt to ambient temperature and subsequent annealing at 433 K, is close to 25 nm. With an assumed lateral dimension of 100 nm, a melting temperature of 446 K is estimated. The calculated melting temperatures for folded-chain crystals of size  $100 \times 100 \times 25 \text{ nm}^3$  and  $40 \times 40 \times 40 \text{ nm}^3$  agree remarkably with the experimentally observed temperature of 446 K. The data in Figure 49 suggest that at room temperature nodular crystals, after annealing at a temperature of 433 K, exhibit a fold-surface at the crystal top and bottom planes (Figure 49d). The melting point of crystals with a non-fold-surface is about 20 K lower than the observed melting temperature, regardless the lateral dimensions. Furthermore, the lateral size of the crystals, if exceeds a critical value of about 30 nm, does not largely affect the temperature of melting, since the nodules and lamellae of lateral dimension of about 40 and 100 nm, respectively, show nearly an identical temperature of melting.

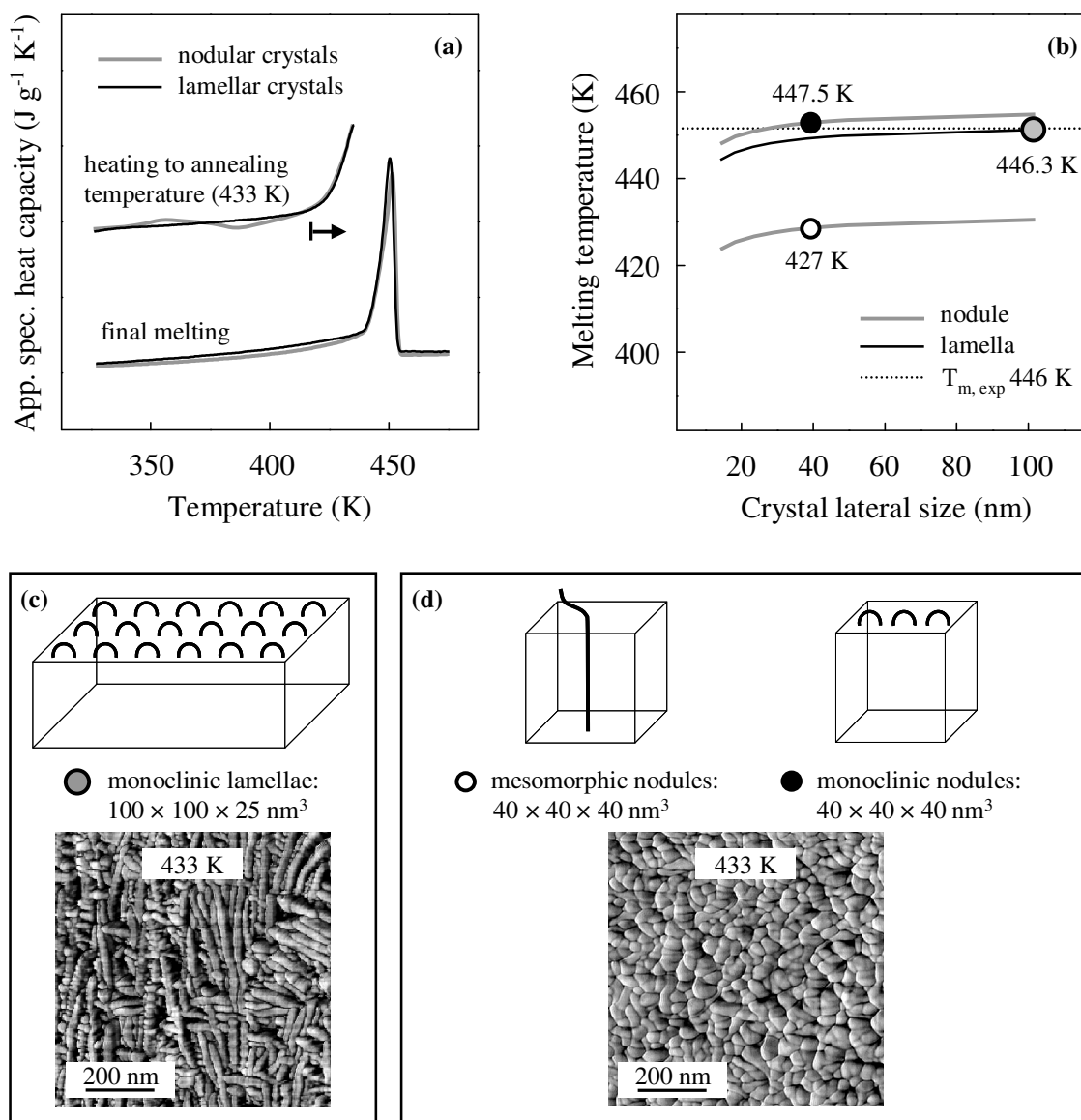


**Figure 49.** (a) Annealing approach and the final melting after annealing of lamellar and nodular crystals of iPP. (b) Melting temperature of fold-surface crystals of 25 nm (center curve) and 40 nm thickness (top curve), and non-fold-surface crystals of 40 nm thickness (bottom curve), as a function of the lateral crystal size. The melting temperatures of the sketched structures are indicated by the symbols. (c) Morphology and sketch of a folded-chain lamellar crystal of about 25 nm thickness. (d) Morphology and sketch of a non-folded and folded-chain nodule of size of about 40 nm.

## 7. Structure – property relations

### 7.1. Thermal and dynamic-mechanical properties

#### 7.1.1. Effect of crystallinity and crystal morphology on rigid amorphous fraction

##### *Effect of crystallinity on rigid amorphous fraction*

Figure 50 (left) shows the rigid amorphous fraction (RAF) of iPP of different history of crystallization as a function of the enthalpy-based crystallinity, with the meaning of symbols described in the figure. The diagonal indicates the total amorphous fraction, i.e.,  $1 - X_c$ . The two vertical arrows, labeled RAF and MAF, illustrate an option of easy reading of data in terms of phase fractions. The experimental data indicate that the absolute RAF decreases with increasing crystallinity, regardless the specific history of crystallization, habit of crystals, or presence/absence of higher-order structures. For instance, the RAF of iPP film, which was prepared by slow cooling at  $0.1 \text{ K s}^{-1}$  is identical to the RAF of iPP film, which initially was quenched at a rate of  $450 \text{ K s}^{-1}$  and subsequently annealed at 433 K for a period of 60 min. The shape of crystals in these specific preparations is largely different, i.e., lamellar for slowly cooled sample and nodular for rapidly cooled sample. The data points, which correspond to these preparations, are circled, for easy identification. An additional data-point at zero crystallinity is added, since it is assumed that the RAF is absent in completely amorphous samples. This assumption implies that the dependence of the RAF on the enthalpy based-crystallinity passes a maximum, which, however, falls into the region between 0 and about 40 % crystallinity, not accessed in the present work. The fraction of crystals, present in semicrystalline preparations, controls the total amount of RAF. For samples of low crystallinity, it is expected that the RAF increases linearly with increasing total surface area of the basal planes of crystals, i.e., with increasing crystallinity in case of predominant lateral crystal growth in the stage of primary crystallization. The incremental increase of RAF per increase of crystallinity, i.e.,  $\Delta\text{RAF}/\Delta X_c$ , in the stage of primary crystallization is affected by (a) the inherent flexibility of a macromolecule of specific chemical structure, being controlled by the number of possible micro-conformations and the energy barriers between them, and (b) the conditions of crystallization, which controls, within limits, the crystal surface structure/coupling of crystalline and amorphous phases. The data, obtained in a previous study on cold-crystallized PET, suggest a slope  $\Delta\text{RAF}/\Delta X_c$  of about 2–3 ( $\approx 0.4/0.15$ ), i.e., the increase

of the RAF is about two- to three-times the increase of crystallinity [6]. For iPP of the present study, only a lower limit of the ratio  $\Delta\text{RAF}/\Delta X_c$  of about unity ( $\approx 0.35/0.40$ ) is estimated from the experimental data. Preparation of iPP of low crystallinity is not possible, since samples with a crystallinity of below about 35 % may only exist as thermodynamically unstable, transient stage during primary crystallization. The initial increase of RAF with increasing crystallinity stops before complete immobilization of the amorphous phase. In other words, there is left a mobile amorphous fraction in iPP of different crystallinity, which can directly be deduced from the difference between RAF data-points and the diagonal.

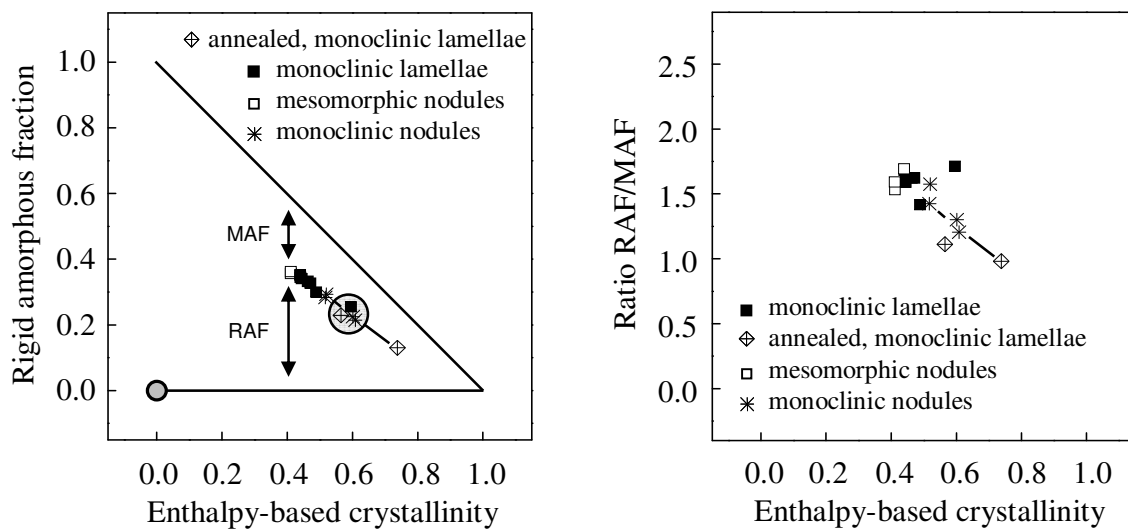


**Figure 50.** Rigid amorphous fraction (left) and the ratio between rigid amorphous fraction and mobile amorphous fraction (right) of iPP, as a function of enthalpy-based crystallinity. The diagonal shows the total amorphous fraction (RAF + MAF) (left).

The exact reason for this observation can be manifold. Initially, the MAF was related to amorphous structure in inter-spherulitic regions, since it was assumed that the amorphous phase within spherulites may completely be immobilized, or exhibits, at least, a reduced relaxation strength [146]. Later analysis of semicrystalline, space-filled spherulitic systems, using small-angle X-ray scattering and dielectric spectroscopy, lead to an assignment of the MAF to regions between stacks of lamellae [147]. Recently, a close proximity of the MAF and RAF was suggested for PA 6, i.e., MAF and RAF are

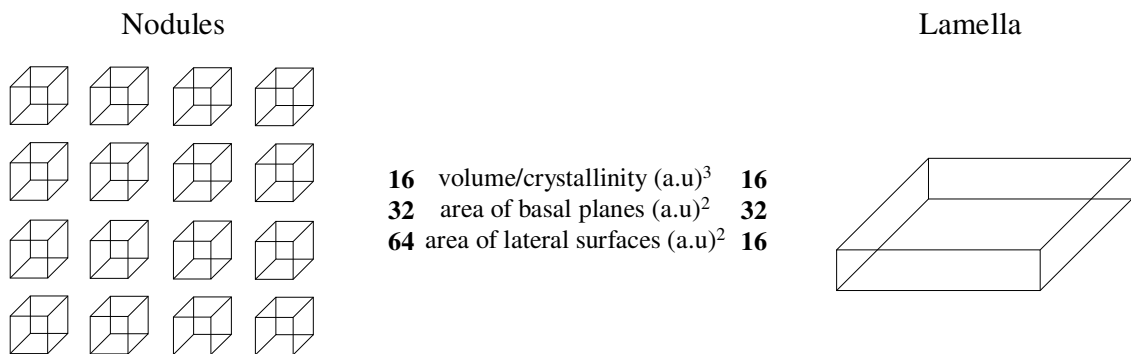
proposed to exist within stacks of lamellae [148]. Regardless the diversity of observations regarding the exact localization of RAF and MAF, full immobilization of the amorphous phase does not seem to be typical in semicrystalline polymers, independent of crystallinity, independent of spherulitic or non-spherulitic crystallization, and independent of the existence of stacks of lamellae or non-lamellar crystals. Note that preparations with nodules are of non-spherulitic superstructure, and preparations with lamellae are of space-filled spherulitic superstructure. Therefore the formation of RAF, at least for iPP, occurs at very local scale in close proximity of crystals only, and that the MAF must not necessarily be related to non-spherulitic regions, or amorphous structure outside of lamellar stacks.

Figure 50 (right) shows the relative ratio between RAF and MAF of iPP of different history of crystallization as a function of the enthalpy-based crystallinity. It decreases within the investigated range of crystallinities between 40 and 75 %. The ratio RAF/MAF is almost two in iPP of 40 % crystallinity, i.e., the RAF is two-times the MAF. The ratio decreases in iPP of high crystallinity to about unity. These data indicate that an increase of the crystallinity of iPP between 40 and 75 % is connected to an increase of the average mobility of amorphous phase, pointing to a reduction of the coupling between amorphous and crystalline phases. In addition to the detection of preservation of a mobile amorphous fraction, even a decrease of the ratio between RAF and MAF was observed with increasing crystallinity. Re-inspection of selected RAF data, available in the literature, confirms this observation that the immobilization of the amorphous phase is reduced in samples of relatively high crystallinity [136]. A straightforward conclusion from the data of Figure 50 (right) is the low degree of coupling of the crystalline and amorphous phases and therefore a relatively high mobility of the amorphous phase in samples of high crystallinity. As a general trend, crystallization at low supercooling or low rate of cooling, allows formation of thick crystals with surfaces of low free energy. This results in reduced covalent linkage between the crystalline and amorphous phases.

### ***Effect of crystal habit on rigid amorphous fraction***

The RAF data of Figures 50 do not allow to identify an influence of the crystal shape on the RAF. In other words, samples of identical crystallinity, independent whether

they contain nodules or lamellae, exhibit a similar RAF if the structure and therefore the surface free energy of the basal planes are identical. Generation of identical surface structures of nodules and lamellae was achieved by annealing at elevated temperature, and was evidenced by subsequent thermal analysis of the temperature of melting. Annealed samples, regardless whether they contain lamellae or nodules, exhibit an identical temperature of melting, which points, according to the Gibbs-Thomson equation, to presence of crystals of identical thermodynamic stability. Though it is expected that the lateral surfaces of crystals are not considered as a major source for immobilization of the amorphous phase, there is not yet provided experimental evidence in the literature. In fact, the data of the present study suggest that the lateral surfaces of crystals do not contribute to the formation of RAF. Figure 51 shows equi-axed nodules with a volume of  $1 \times 1 \times 1$  (a.u.)<sup>3</sup>, and a lamella with a volume of  $4 \times 4 \times 1$  (a.u.)<sup>3</sup>.



**Figure 51.** Schematic of nodules (left) and a lamella (right). The volume and the area of the basal planes of 16 nodules are identical to those of a single lamella. The total area of lateral surfaces of nodules is four-times the total area of lateral surfaces of lamella.

The only difference between the nodules and the lamella are the lateral dimensions. Identical volume of  $16$  (a.u.)<sup>3</sup>, i.e., identical crystallinity, and identical area of basal planes, is achieved if 16 nodules are present. The total area of the lateral surfaces of nodules in this particular case, however, is four-times the area of the lateral surfaces of the lamellae. If the lateral surfaces of crystals would significantly contribute to the immobilization of the amorphous phase, then samples with nodular crystals needed to

show a considerably larger RAF than samples which contain lamellae. This, however, is not observed and confirms the assignment of the RAF to the basal planes of crystals.

### 7.1.2. Effect of crystal morphology and phase fractions on the mobility of mobile amorphous fraction

Figure 52 shows the glass transition temperature of the mobile amorphous phase of iPP, as a function of the rate of cooling on primary melt-crystallization, obtained from the peak maximum of the loss factor at a heating rate of 2 K min<sup>-1</sup> using DMA (left) and from the heat capacity data obtained at a heating rate of 40 K min<sup>-1</sup> using DSC (right). The filled and open squares represent data, which were obtained on non-annealed samples containing lamellae and nodules, respectively. The effect of annealing on the glass transition temperature is illustrated for selected samples with the arrows and the diamond and star symbols. The DMA data, consistently, are about 20–25 K higher than the DSC data, due to largely different signals recorded by the instruments [149,150].

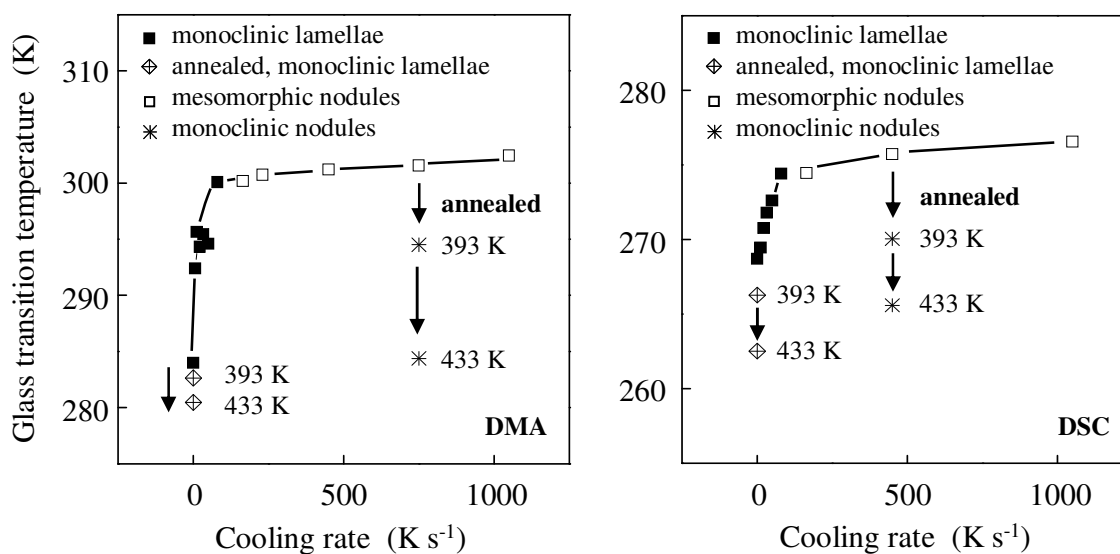


**Figure 52.** Glass transition temperature of the mobile amorphous phase of iPP as a function of the rate of cooling, obtained by using DMA (left) and DSC (right). The effect of annealing on the glass transition temperature is illustrated for selected samples.

The glass transition temperature of iPP, which was melt-crystallized at 0.1 K s<sup>-1</sup>, shows a DMA glass transition temperature of about 282 K that increases to about 300 K

for a sample melt-crystallized at about  $10^2 \text{ K s}^{-1}$ . A further increase of the cooling rate to  $10^3 \text{ K s}^{-1}$  is not connected with a major change of the glass transition temperature, despite the crystal shape changes from lamellae to nodules. This observation is paralleled by independence of the enthalpy-based crystallinity on the rate of cooling between  $10^2$  and  $10^3 \text{ K s}^{-1}$ . Annealing at elevated temperature, results in a decrease of the glass transition temperature, which is more distinct for samples of low crystallinity (star-symbols), and less pronounced for preparations of initially high crystallinity (cross-filled diamonds). The data suggest that a decrease of the glass transition temperature on annealing is proportional to a simultaneous increase of crystallinity.

Figure 53 (left) shows a correlation between the glass transition temperature of iPP of different history of crystallization and the enthalpy-based crystallinity.

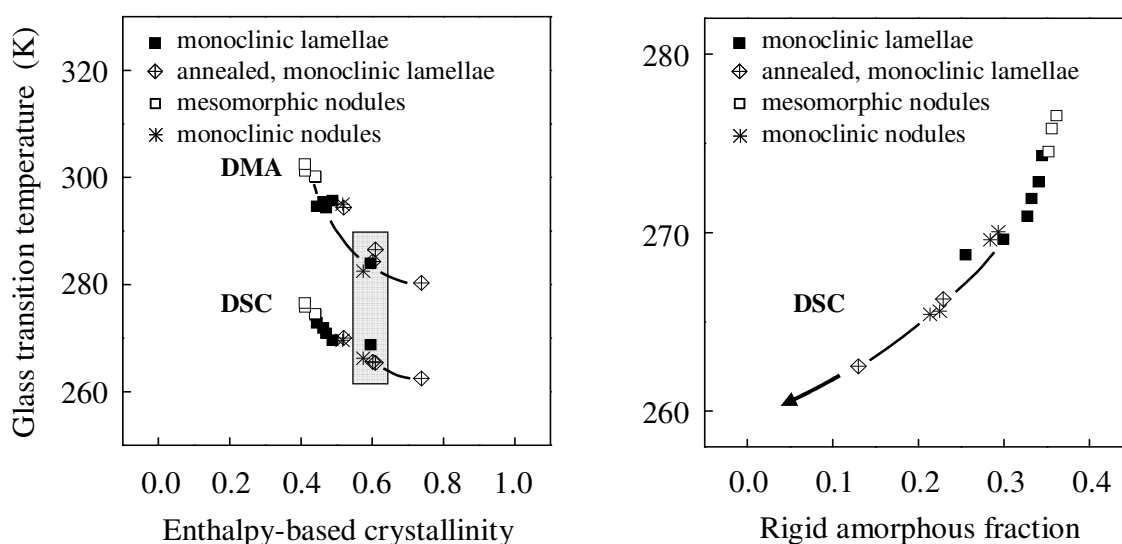


**Figure 53.** The glass transition temperature of iPP as a function of enthalpy-based crystallinity (left) and rigid amorphous fraction (right).

The glass transition temperature of the mobile amorphous fraction decreases non-linearly with increasing crystallinity. Most striking observation, regardless the exact pathway of crystallization and the shape of crystals, is the fitting of data to a single function. In other words, apparently, it does not matter whether a crystallinity of nearly 60 % was achieved by slow melt-crystallization at a rate of  $0.1 \text{ K s}^{-1}$ , or by fast cooling at a rate of  $450 \text{ K s}^{-1}$  and subsequent annealing at  $433 \text{ K}$ . The glass transition temperature,

in both cases, is almost identical, as is indicated by the gray-shaded rectangle, highlighting the data points obtained independently by DMA and DSC. The lower glass transition temperature in preparations of high crystallinity is paralleled by detection of a low amount of RAF. This implies that the glass transition temperature of the MAF may be controlled by the mobility and the amount of RAF. In order to confirm this assumption, the glass transition temperature of the MAF is plotted as a function of the RAF in Figure 53 (right). The data, unambiguously, reveal a correlation between the glass transition temperature of the MAF and the RAF, such that an increasing RAF causes an increase of the glass transition temperature. This correlation provides evidence for a distinct coupling of MAF and RAF. The mobility of the MAF, as is expressed by its glass transition temperature, decreases if large amount of RAF is evident due to presence of crystals with a rather imperfect structure of the basal planes. Extrapolation of the glass transition temperature of the MAF to zero RAF yields a value of 258–259 K. This value is within the range of glass transition temperature of a fully amorphous PP [2,64].

### **7.1.3. Effect of crystallinity and crystal morphology on dynamic-mechanical behavior**

The change of crystallinity as a function of the rate of primary melt-crystallization and on subsequent heating has a direct effect on the dynamic-mechanical behavior of iPP. Figure 54 shows the enthalpy-based crystallinity of iPP samples of different history of crystallization, as a function of temperature (left). A systematic decrease of crystallinity, at ambient temperature, can be recognized on moving from the top thick line to the bottom thick line due to an increase of cooling rate. The cooling rates change from the top thick line to the bottom thick line in the following order, 0.1, 12, 22, 33, 50, 80, 165, 450, 750, and 1050 K s<sup>-1</sup>. The data of samples melt-crystallized between 80 and 450 K s<sup>-1</sup> are nearly overlapping. In detail, a decrease of crystallinity is observed with an increase of temperature as well as the cooling rate on primary melt-crystallization. For instance, the sample initially melt-crystallized at 0.1 K s<sup>-1</sup> (top thick line) shows an enthalpy-based crystallinity of about 60 %. Subsequent heating to a temperature of about 400 K results in a decrease of crystallinity, from about 60 to 52 %. In contrast, an exclusive formation of mesomorphic structure of iPP, represented by a sample melt-crystallized at 1050 K s<sup>-1</sup> (bottom thick line), shows comparatively a lower crystallinity of about 40 %. During

heating, the crystallinity initially decreases from about 40 % to 38 % on reaching a temperature of about 350 K. On further heating to a temperature of about 400 K, an increase of crystallinity to about 42 % is observed. On continuous heating above a temperature of about 400 K, both preparations show a strong decrease of crystallinity due to the melting of crystals. The effect of subsequent annealing on the temperature dependent changes of the enthalpy-based crystallinity is demonstrated for selected iPP samples, which initially were melt-crystallized at  $0.1 \text{ K s}^{-1}$  (thin lines) and  $750 \text{ K s}^{-1}$  (thick lines), in Figure 54 (right). The crystallinity of both preparations, at ambient temperature, is increased as a result of annealing, which is indicated by curve 1 in case of sample melt-crystallized at  $750 \text{ K s}^{-1}$  before annealing and by curves 2 and 3 after annealing at 393 and 433 K, respectively. A higher crystallinity is observed for a sample initially melt-crystallized at  $0.1 \text{ K s}^{-1}$ , as a result of annealing at identical temperatures, as can clearly be recognized after annealing at 433 K (top thin line). As expected, the crystallinity strongly decreases above about 400 K to reach a value of zero above  $T_m$ .

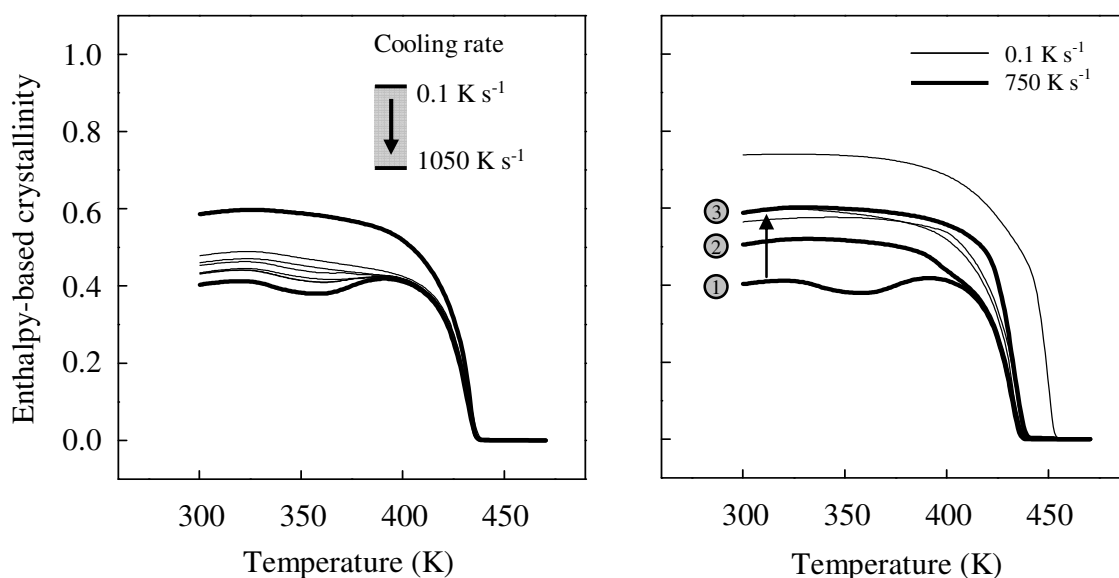


**Figure 54.** Enthalpy-based crystallinity of melt-crystallized (left) and subsequently at elevated temperature annealed (right) iPP, as a function of temperature, details in text.

Figure 55 shows the modulus of elasticity (left) and loss factor (right) of selected iPP samples, initially melt-crystallized at a rate of cooling between  $0.1$  and  $1050 \text{ K s}^{-1}$ , as a function of temperature. A systematic decrease of modulus of elasticity, at ambient

temperature, can be recognized on moving from the top thick line to the bottom thick line due to an increase of cooling rate. The cooling rates, in the left graph, change from the top thick line to the bottom thick line in the following order, 0.1, 6, 12, 22, 80, 165, 230, 750, and 1050 K s<sup>-1</sup>. Similarly, the cooling rates change from the bottom thick line to the top thick line in the following order, 0.1, 6, 12, 22, 450, and 1050 K s<sup>-1</sup>, in the right graph. In detail, the changes of the modulus of elasticity, on increasing the temperature as well as the cooling rate on primary melt-crystallization, go parallel with the simultaneously observed changes of crystallinity. For instance, the crystallinity values are larger for a sample melt-crystallized at 0.1 K s<sup>-1</sup> (top thick line), which accordingly result in the higher values of the modulus of elasticity, within the investigated range of temperature. In contrast, a sample melt-crystallized at 1050 K s<sup>-1</sup> (bottom thick line) shows lowest crystallinity, which results in smaller values of the modulus of elasticity, as a function of temperature. The variation of the modulus of elasticity of iPP of different crystallinity, as a function of temperature, is consistent with an earlier report [151].

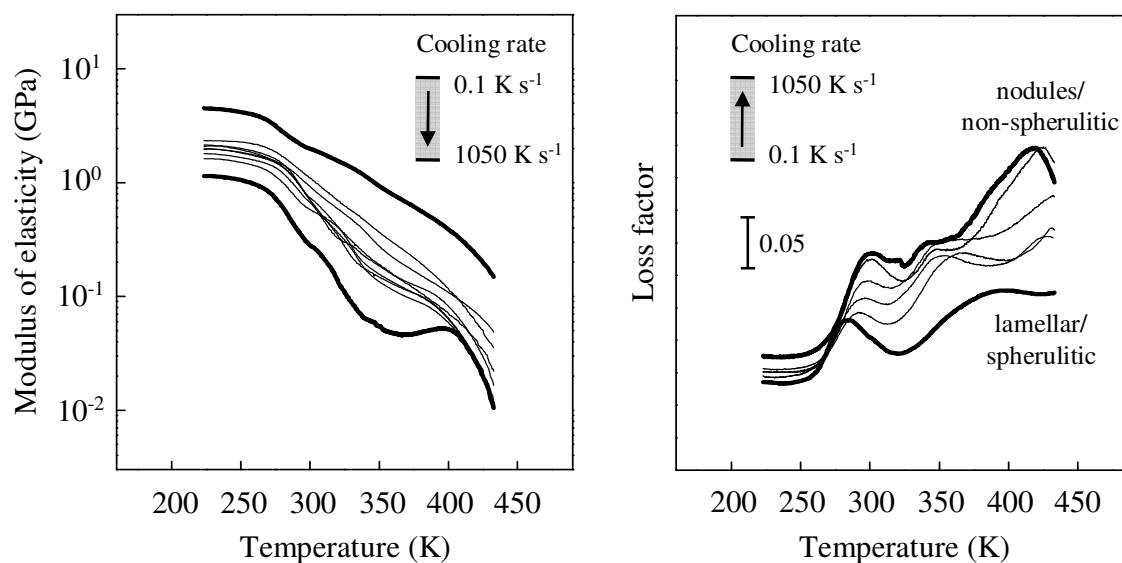


**Figure 55.** Modulus of elasticity (left) and loss factor (right) of iPP, initially melt-crystallized at different rates of cooling, as a function of temperature, details in text.

The change of modulus of elasticity as a function of temperature shows a step-like decrease at least at two different temperature ranges of between about 250-320 K and about 320-400 K. The first step-like change is identified as the glass transition

temperature, which appears like a peak in the loss factor curve [152]. This peak broadens and shifts to higher temperatures indicating a decrease of the mobility of MAF, which is due to an increase of RAF. The second step-like change corresponds to the second loss factor peak and is regarded as the  $\alpha$ -relaxation, particularly for the samples exclusively crystallized into monoclinic structure, consisting of lamellar crystals [76]. The  $\alpha$ -relaxation in iPP is ascribed to the diffusion of defects in the crystalline phase, which requires the cooperative mobility of the amorphous phase to conform to the changes in the crystalline phase, and is suggested to involve a limited number of helical jumps for the chain motion in the crystalline phase [76,153,154]. Investigation of the effect of morphology on dynamic-mechanical behavior of iPP showed a decrease of the  $\alpha$ -relaxation peak with a decrease of spherulites size and crystallinity, primarily due to an increase of the mobility of molecular segments within lamellae. In case of non-spherulitic preparations, obtained by glass-crystallization of iPP at different temperatures, two components of the  $\alpha$ -relaxation process were distinguished. A low temperature component, occurring at a temperature below about 350 K, was attributed to the relaxation of molecules at the irregular surface of crystallites and a high temperature component of the  $\alpha$ -relaxation process, occurring at a temperature above about 350 K, attributed to the viscous slip process of crystalline elements, which is enhanced by the presence of a smectic phase and by the decrease of the crystal size and crystallinity [151]. A similar trend is observed for the melt-crystallized samples of iPP used in this study, where a change from an initially monoclinic lamellae/spherulitic structure to mesomorphic nodules/non-spherulitic structure shifts the second loss factor peak temperature from about 398 to 342 K, respectively. This indicates an increase of chain mobility within the crystals. In case of mesomorphic iPP, the second loss factor peak can not be directly related to the  $\alpha$ -relaxation process, due to the reorganization process of mesomorphic nodules on heating. The study of the mesomorphic-to-monoclinic phase transition in an initially mesomorphic iPP, as observed by DSC and WAXS, and the study of the  $\alpha$ -relaxation process in an initially monoclinic iPP, as observed by DMA, shows that both processes initiate in a close range of temperatures. Since both processes primarily include the crystalline segmental motion in the chain direction, therefore, it is suggested that the onset of second loss factor peak, in case of mesomorphic iPP, is due to

a complex structural reorganization process resulting from the overlapping of the mesomorphic-to-monoclinic phase transition and the conventional  $\alpha$ -relaxation process.

Figure 56 shows the modulus of elasticity (a) and loss factor (b) of iPP, melt-crystallized at 0.1 (dotted lines) and 750 K s<sup>-1</sup> (solid lines), and subsequently annealed at temperatures of 393, 413 and 433 K, as a function of temperature. In both graphs, the curves corresponding to the annealing temperatures are labeled as 2, 3 and 4, respectively, for a sample initially melt-crystallized at 750 K s<sup>-1</sup>, whereas the curves labeled as 1 denote the non-annealed samples. The curve of a sample melt-crystallized at 0.1 K s<sup>-1</sup> are not labeled, since the changes are not distinct after annealing. As expected, the increase of the modulus of elasticity parallels the increase of crystallinity, being more distinct in samples of initially lower crystallinity. The loss factor of iPP melt-crystallized at 0.1 K s<sup>-1</sup> shows the glass transition temperature at about 284 K, which decreases to about 280 K after annealing at 433 K for 60 minutes. In contrast, sample initially melt-crystallized at 750 K s<sup>-1</sup>, shows a decrease of the glass transition temperature from about 300 to about 284 K, after annealing at identical conditions. The decrease of the glass transition temperature is linked to a decrease of RAF, which, in turn, increases the mobility of MAF. Furthermore, the increase of crystallinity shifts the second loss factor peak to higher temperatures, due to increase of crystal perfection [76,151,155,156].

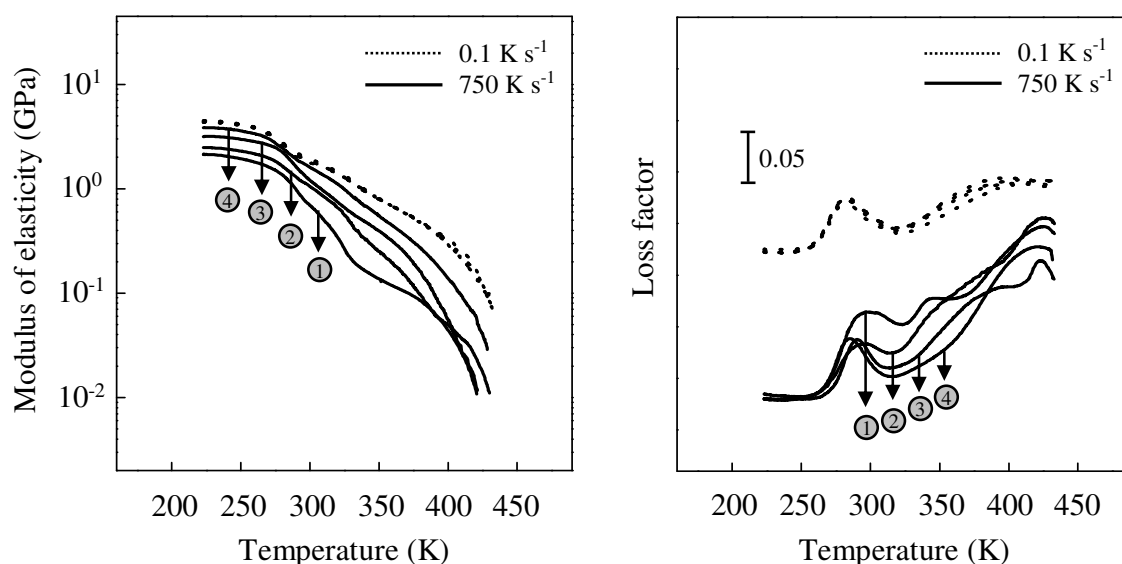


**Figure 56.** Modulus of elasticity (left) and loss factor (right) of melt-crystallized and subsequently annealed iPP, as a function of temperature, details in text.

## 7.2. Mechanical properties

### 7.2.1. Effect of crystal morphology and crystallinity on tensile deformation

The tensile deformation behavior is tightly connected to the mobility of polymer chain segments and is controlled by the crystallinity, crystal structure and morphology. Figure 57 shows the tensile-stress strain curves of selected iPP samples, initially melt-crystallized between the rates of cooling of  $10^{-1}$  to  $10^3$   $\text{K s}^{-1}$  (left). In all the preparations, yielding is observed. In detail, a sample with cross-hatched lamellae/spherulites, obtained at a cooling rate of  $0.1$   $\text{K s}^{-1}$ , shows a brittle behavior and breaks at a strain of only about 10 %. The post-yield region, where the formation of fibrils occurs, is absent in this sample. A change from a brittle to a ductile behavior is observed on increasing the cooling rate, which is indicated by a systematic increase of the strain at break. The structure-controlled brittle-to-ductile transition parallels a change of crystal morphology from cross-hatched monoclinic lamellae/spherulites to mesomorphic nodules/no spherulites. The increasing deformability, achieved by increasing the rate of cooling of the melt, reaches its limit in iPP samples with mesomorphic nodules/no spherulites, i.e., in samples melt-crystallized above the critical rate of cooling. In this case a maximum strain of more than about 500 % is recorded. Furthermore, no stress-whitening of the samples was observed.

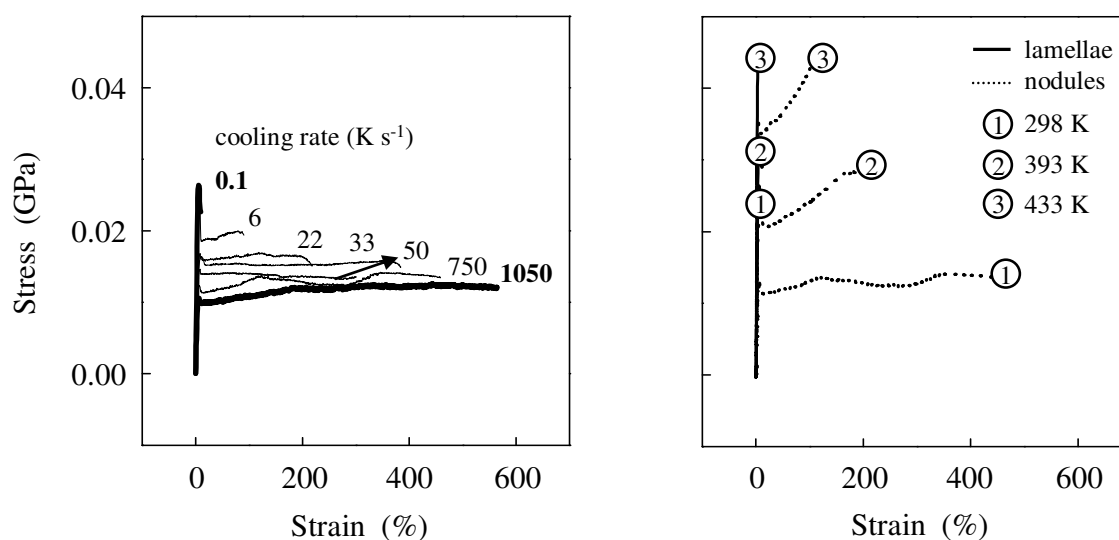


**Figure 57.** Stress-strain curves of melt-crystallized (left) and subsequently at elevated temperature annealed iPP (right).

The effect of annealing on the tensile-stress strain behavior of samples initially melt-crystallized at  $0.1 \text{ K s}^{-1}$  (solid lines) and  $750 \text{ K s}^{-1}$  (dotted lines) is shown in Figure 57 (right). The brittle behavior of iPP with cross-hatched lamellae/spherulites is maintained after annealing. In contrast, annealing of a structure initially consisting of mesomorphic nodules/no spherulites shows a considerable strain-hardening, i.e., increase of stress with strain, in the post-yield region. These preparations still preserve a ductile behavior, however, the strain at break decreases to about 150 % after annealing at 433 K. The strain-hardening of iPP with monoclinic nodules/no spherulites (dotted lines 2 and 3) results in an increase of stress at break, such that, the fracture occurs at a close-to-identical stress as observed for iPP with lamellar crystals/spherulites (solid lines 2 and 3). Importantly, the crystallinity of samples, with the tensile-stress strain curves represented by solid and dotted lines 3, is identical, however, the deformation in the post-yield region is largely different. The identical crystallinity obtained in both preparations can, advantageously, be used to explain the post-yield deformation behavior on the account of different crystal morphology/superstructure of these preparations [157].

### **7.2.2. In situ observation of the deformation behavior by AFM**

#### ***Deformation of cross-hatched lamellar morphology of iPP***

Figure 58 shows the selected AFM-images of iPP with initially cross-hatched lamellar morphology before (left) and after deformation of about 10 % (center and right), which corresponds to the strain at break. Images of the stretched samples showed a complete destruction of the film. The presented AFM-images, however, were collected after the failure of the sample, at a location close to the fracture. The center and right AFM-images, represent two different areas of the fractured sample, and show, as an example, the destruction of lamellae and a spherulite, respectively. The arrow shows the draw direction. AFM-images show the cracks at the film surface, formed and propagated mainly in a direction perpendicular to the applied stress, leading to the breakage of lamellar crystals (circled area, center image), which simultaneously result in destruction of spherulites (right image). The post-yield region, where the plastic deformation of crystals occurs, is absent, and there can hardly be observed any crystal reorientation and slip, confirming the macroscopically observed brittle behavior. The brittle behavior of cross-hatched lamellar preparations of iPP has been consistently observed [62,158], and

is attributed to the interlocking of amorphous chains between cross-hatched lamellar structure that hinders the deformation of amorphous phase. This argument is supported by the ability of  $\beta$ -spherulites of iPP, which can be deformed to large strain, due to the presence of only radially extended lamellae in an amorphous matrix [158].

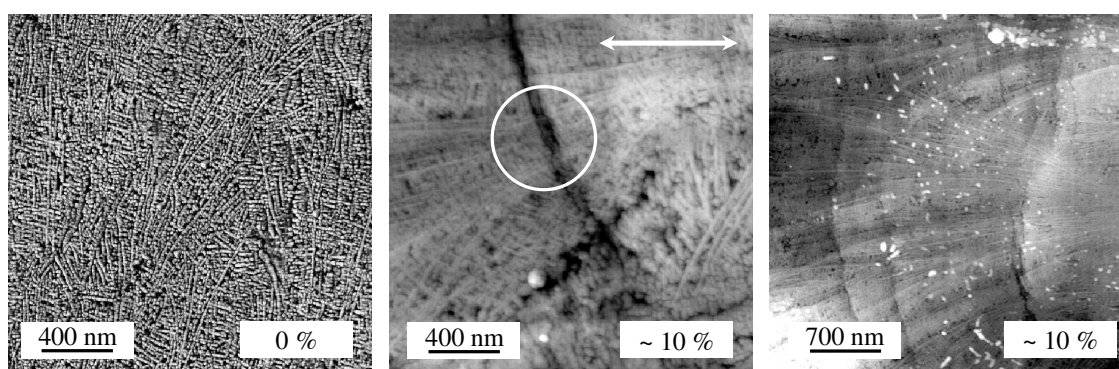


**Figure 58.** AFM-images of the cross-hatched structure of iPP, initially melt-crystallized at  $0.1 \text{ K s}^{-1}$ , before (left) and after deformation (center and right).

#### ***Deformation of nodular morphology of iPP***

Tensile deformation of semicrystalline polymers is explained by two different models. One model explains tensile deformation behavior as a continuous plastic deformation of the spherulitic structure followed by discontinuous transformation from the spherulitic structure to the fiber structure, and finally the plastic deformation of the fiber structure. This model involves the fragmentation of lamellar crystals into blocks, interconnected by the tie molecules, and their transformation into fibrillar structure [159]. The second model includes local melting and recrystallization of lamellae, leading to the formation of fibrillar structure [160]. These models, in the present study, are not applicable to explain the deformation behavior of samples with cross-hatched lamellar morphology, since the fragmentation and the fibril formation does not occur. However, these models can be useful to understand the deformation of iPP with nodular crystals.

It is clear that in an undeformed state, WAXS analysis of mesomorphic iPP shows no detectable molecular orientation. The chains become highly orientated, in both the crystalline and the amorphous phases, during tensile deformation [115,161], as a result of plastic flow at molecular level [98]. The deformation is suggested to occur via the slip

and dislocation movements, above the yield point [162]. The deformation of quenched, mesomorphic iPP, at ambient temperature, is connected to a transformation of mesomorphic structure into mesomorphic fibrils, without formation of a monoclinic structure [163]. The mesomorphic fibrils show an increased average inter-chain distance, as compared to an initially quenched, mesomorphic iPP. In a DSC analysis, iPP with mesomorphic fibrils does not show a mesomorphic-to-monoclinic phase transition, as is observed in the initially undeformed, mesomorphic iPP, however, the final melting, for both samples, occurs at a nearly identical temperature of above about 435 K [115].

A direct evidence of the formation of fibrillar structure is now provided by in situ AFM analysis of the deformation of nodular domains of iPP. Figure 59 shows in situ AFM-images of undeformed (left) and deformed iPP films (center and right), with initially non-annealed mesomorphic (top) and at 433 K annealed monoclinic nodules (bottom) [157]. Images are collected in stretched conditions. The arrows show the draw direction. The scheme of deformation of iPP with nodular domains appears identical, independent of the crystal structure and crystallinity. Figure 60 shows a simplified three-stage model of the deformation of iPP, with initially mesomorphic nodules. In an undeformed state, mesomorphic nodules are embedded in an amorphous matrix and exhibit a quasi-globular shape. The neighboring nodules are connected by tie-molecules through an amorphous region (stage 1). Deformation, below about 100 %, does not show a gross change of the crystal morphology. This allows to speculate that, primarily, deformation occurs in disordered amorphous regions, which results in orientation of chain segments in the draw direction. Simultaneously, the deformation of tie-molecules can transmit stress to the neighboring inter-connected nodules, resulting in their re-orientation in the draw direction. The globular shape of nodules, in comparison to the plate-like geometry of lamellae, is connected with less geometrical constraint regarding the mobility of chains in the amorphous regions and reorientation of nodular domains in draw direction. The nodules apparently move in the draw direction, with their quasi-globular shape maintained. The deformation is suggested to occur by the chain slip mechanism, activated by the applied stress, leading to the disintegration of nodules, which however is not directly observed. As the deformation process continues, orientation and alignment of chain segments within nodular domains and amorphous regions occur, initiating the formation of fibrillar structure. AFM-image obtained after a

deformation of about 200 %, clearly shows the nodules and the fiber structure aligned in the draw direction (stage 2).

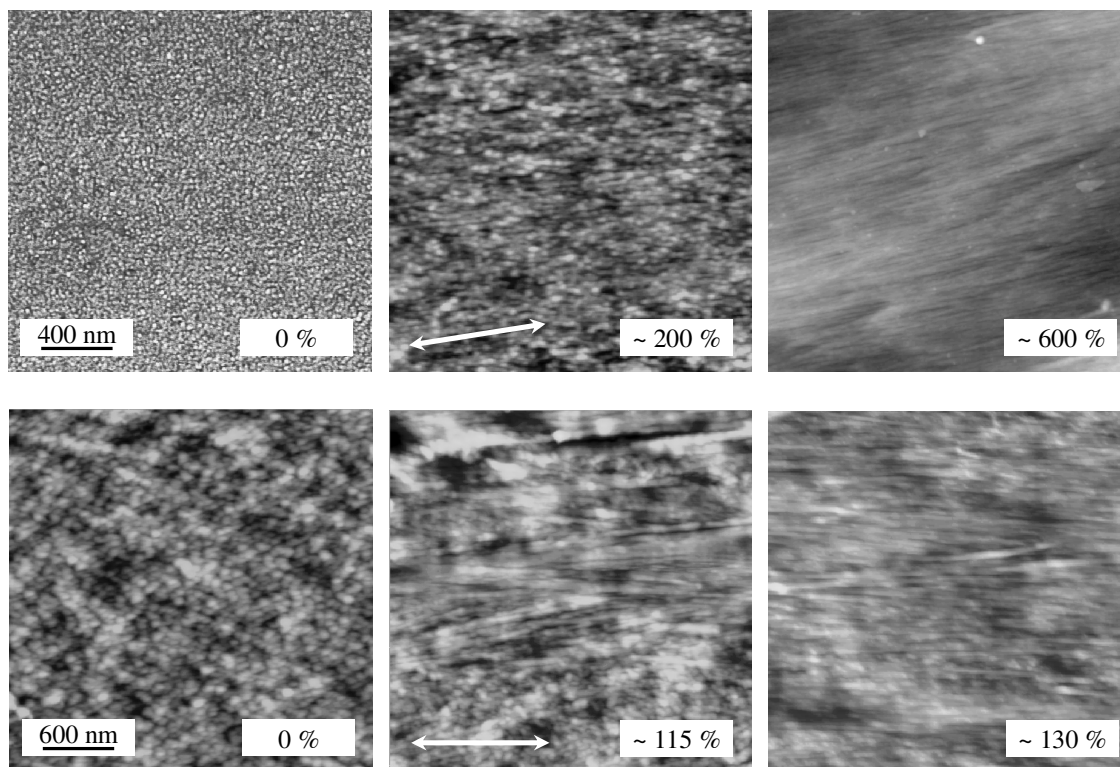


**Figure 59.** *In situ* AFM-images of deformed iPP films, with initially non-annealed, mesomorphic (top) and at 433 K annealed, monoclinic nodules (bottom).

The final morphology is identified, exclusively, as fibrillar. The deformation process completely transforms the nodular morphology into a fibrillar morphology, as shown in AFM-image of the sample deformed to a strain value of about 600 %. The deformation occurs irreversibly, i.e., the fibrillar morphology is preserved on unloading the sample. The thickness of fiber structure is close-to-identical as the initial size of nodules (stage 3). The deformation of iPP with monoclinic nodules shows a similar trend, as the deformation of iPP with mesomorphic nodules, as shown in Figure 59 (bottom). The major difference observed is the percentage deformation of these samples. In case of monoclinic nodules, the formation of fibrillar structure starts at low deformation of below about 70 %. AFM-images obtained after the deformation of about 115 % show nodules and fiber structure oriented in the draw direction. The final morphology is fibrillar, as

shown by an AFM-image obtained after a deformation of about 130 %. The thickness of fibrils is close-to-identical as the initial size of monoclinic nodules. The deformation occurs irreversibly and is suggested to involve identical mechanism as the deformation of initially mesomorphic iPP. Analysis of AFM-images reveals a strong effect of the crystal shape and crystallinity on the deformation behavior of iPP. For samples of identical crystal morphology, e.g., iPP with mesomorphic or monoclinic nodules, the degree of crystallinity limits the ultimate elongation. In contrast, if the crystallinity is identical, as observed in iPP with monoclinic cross-hatched lamellae and annealed monoclinic nodules, the deformation behavior is controlled by the crystal morphology.

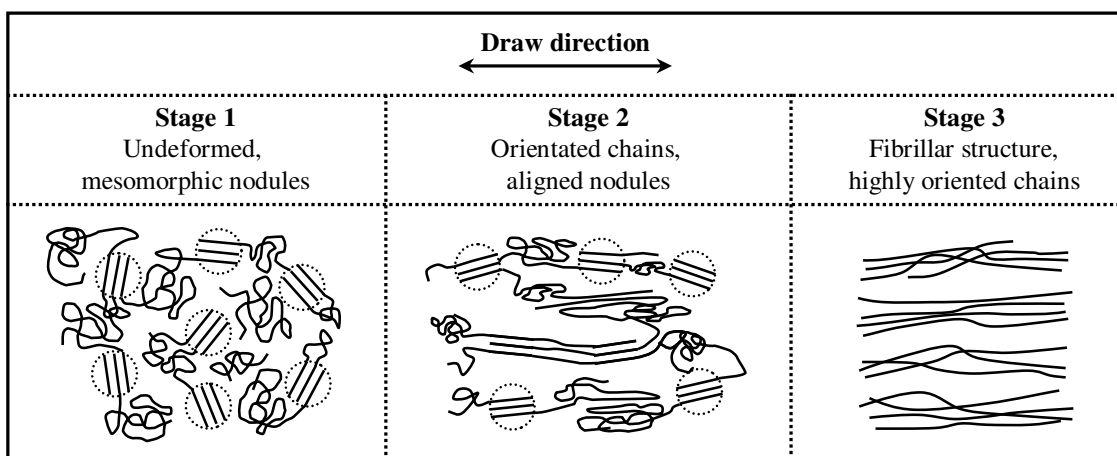


**Figure 60.** Schematic of the transition of nodular to fibrillar morphology in iPP.

### 7.2.3. Effect of crystal morphology and crystallinity on modulus of elasticity and yield stress

Figure 61 shows the modulus of elasticity of iPP of different history of crystallization as a function of the rate of cooling on primary melt-crystallization (left). The filled and open symbols represent data, which were obtained on samples with lamellar and nodular crystals, respectively. The cross-filled symbols show the effect of annealing on the modulus of elasticity of two selected samples, which initially were melt-crystallized at rates of cooling of 0.1 and 750 K s<sup>-1</sup>. The modulus of elasticity is measured on sinusoidal mechanical perturbation within the linear visco-elastic deformation-range (squares), and also on basis of classical tensile testing (diamonds). The comparison of

data obtained on different instruments, employing different perturbation, does not indicate instrumental, and analytical errors. The modulus of elasticity of samples which contain lamellae, decreases from about 1.5 GPa to about 0.5 GPa with increasing rate of cooling between  $10^{-1}$  to  $10^2$   $\text{K s}^{-1}$ , respectively. Melt-crystallization at a cooling rate larger than the critical rate of cooling, exclusively, is connected with the formation of mesomorphic nodules, and shows only a minor effect on the modulus of elasticity. It remains at low level of about 0.5 GPa. The observed decrease of the modulus of elasticity with increasing rate of cooling is likely due to the superimposed effects of a decrease of density/crystallinity, thickness of lamellae and the size of spherulites. In contrast, the formation of mesomorphic nodules, independent of the rate of cooling of the melt, yields a nearly identical density/crystallinity and the crystal morphology/superstructure, therefore, a constant low modulus of elasticity is observed.

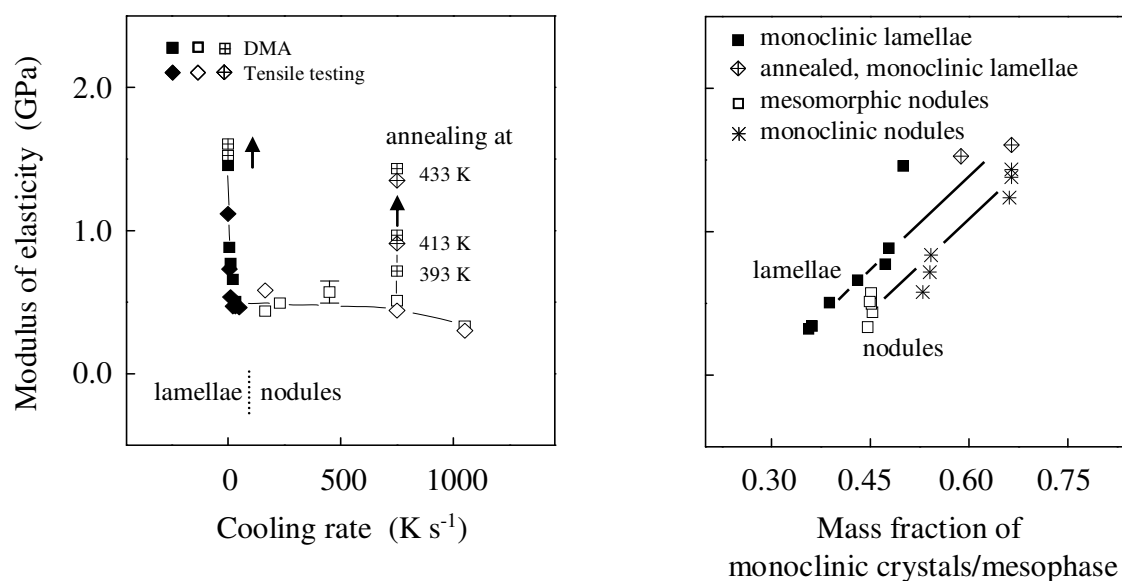


**Figure 61.** Modulus of elasticity as a function of the rate of cooling on primary melt-crystallization (left) and the mass fraction of monoclinic crystals/mesophase (right).

Annealing at elevated temperature causes a distinct increase of the modulus of elasticity. As a result, it is possible to adjust the identical values of the modulus of elasticity of samples of different crystal morphology. For instance, annealing of iPP with nodules, initially melt-crystallized at  $750$   $\text{K s}^{-1}$ , at  $433$  K, causes an increase of the

modulus of elasticity from initially 0.5 GPa to about 1.45 GPa. This value is identical in case of a sample initially melt-crystallized at  $0.1 \text{ K s}^{-1}$ . In other words, the modulus of elasticity of initially rapidly melt-crystallized and subsequently annealed iPP, which contains monoclinic nodules, is identical to the modulus of elasticity of an initially slowly melt-crystallized iPP, which contains lamellae. It is clear that in these preparations, the primary factor leading to an increase of the modulus of elasticity is crystallinity, since the initially formed habit of crystals or superstructure are maintained after annealing [157].

The modulus of elasticity of a semicrystalline sample, in general, can be described as a super-position of contributions from the amorphous and crystalline phases [164]. The insensitivity of the modulus data on morphology of a semicrystalline polymer allows to establish a relationship between the modulus of elasticity and density/crystallinity. Such a relationship results in an increase of the modulus of elasticity with an increase of density/crystallinity [70,165,166]. The modulus data obtained on PE, including low-density branched PE to high-density PE, revealed a lower modulus of elasticity for samples of lower density/crystallinity and a higher modulus of elasticity for samples of higher density/crystallinity [20]. However, the often reported scattering of modulus data of various other semicrystalline polymers show that the density/crystallinity alone is not sufficient to explain the observed changes of the modulus of elasticity [7,98]. In case of iPP, the formation of stable lamellar or nodular morphology, i.e., the habit of crystals does not largely change on heating, allows to produce samples of identical crystallinity and structure, in order to directly evaluate the effect of crystal morphology on tensile properties.

The correlation between the modulus of elasticity and the mass fraction of monoclinic crystals/mesophase, obtained from the density data, of iPP is shown in Figure 61 (right). The filled and open squares represent the data of samples with monoclinic lamellae or mesomorphic nodules, respectively. The cross-filled diamonds and star symbols represent the data of annealed monoclinic lamellae and monoclinic nodules, respectively. The data support the general expectation of an increase of the modulus of elasticity with an increase of crystallinity, with the expectation based on the commonly applied Reuss or Voigt approximation of superposition of properties of crystal and amorphous phases [167]. As such it is straightforward to explain the observed variation of the modulus of elasticity of different preparations with the change of crystallinity, i.e.,

a lower fraction of the ordered phase corresponds to a lower modulus and a higher fraction of the ordered phase corresponds to a higher modulus. Most importantly, a direct effect of the crystal morphology and/or superstructure on the modulus of elasticity can be identified, which, in general, is not possible in other semicrystalline polymers, since the preparation of samples of identical crystallinity but qualitatively different crystal morphology is not possible. It is clear that the samples containing nodules/no-spherulites exhibit slightly lower values of the modulus of elasticity than samples which contain cross-hatched lamellar crystals in a spherulitic superstructure, despite identical fraction of crystals [157].

Figure 62 shows the yield stress of iPP as a function of the rate of primary melt-crystallization (left) and the mass fraction of monoclinic crystals/mesophase (right). The filled and open symbols represent data which were obtained on samples with monoclinic lamellae and mesomorphic nodules, respectively. The cross-filled diamonds and star symbols represent annealed samples with monoclinic nodules and lamellae, respectively.

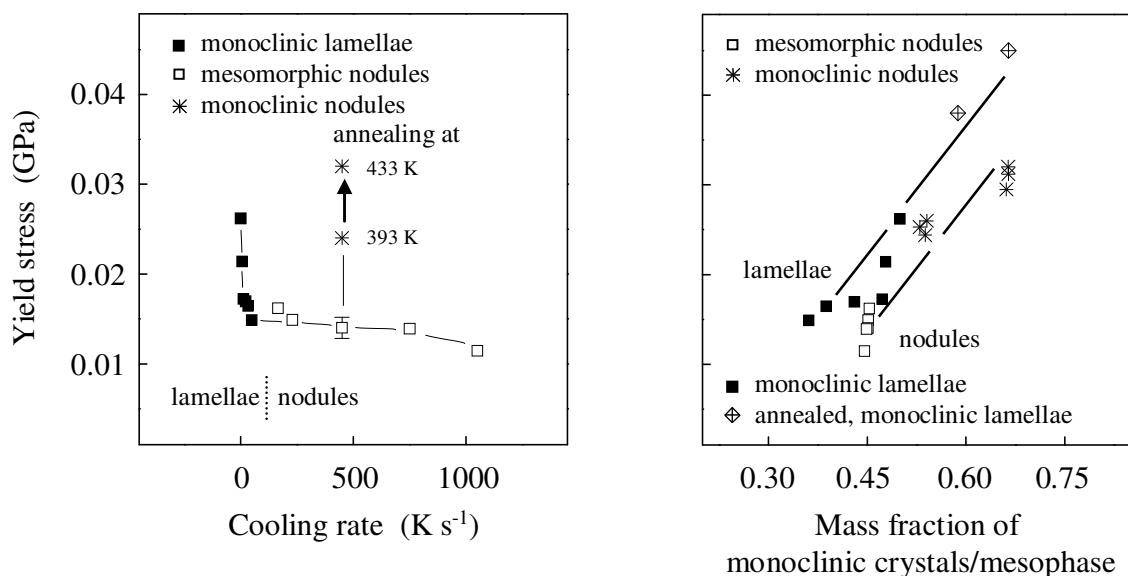


**Figure 62.** Yield stress of iPP as a function of the rate of cooling on primary melt-crystallization (left) and the mass fraction of monoclinic crystals/mesophase (right).

The yield stress data show a similar trend as the modulus of elasticity. It decreases with an increase of cooling rate, in the region where lamellae are present, and remains at

low level if lamellae are replaced by nodules. In the region, where lamellae are present, a decrease of the yield stress from about 0.026 GPa to less than about 0.015 GPa is observed on increasing the cooling rate from  $10^{-1}$  to  $10^2$  K s<sup>-1</sup>, due to a decrease of crystallinity and the size of spherulites. Above a critical rate of cooling, the yield stress remains at a low level of about 0.013 GPa. This observation parallels the independence of crystal morphology and crystallinity on the rate of primary melt-crystallization, above the critical rate of cooling rate. An increase of the yield stress is observed with an increase of annealing temperature, which is connected to an increase of density/crystallinity. A correlation between the yield stress and the mass fraction of monoclinic crystals/mesophase is shown in Figure 62 (right). Similarly, like the modulus of elasticity, the yield stress increases with an increase of the fraction of the ordered phase, with an exception that the presence of nodules in samples of iPP shows a smaller value of the yield stress, in comparison to a lamellar preparation of iPP, despite identical fraction of crystals [157].

The data of Figures 61 (right) and 62 (right) clearly show that the crystallinity alone is not primarily responsible for the observed variation of the modulus of elasticity and yield stress. The observations of the macroscopic tensile test and in situ AFM deformation behavior allow to introduce the crystal habit, i.e., laterally extended lamellae or nearly equi-axed nodules, as an additional parameter controlling these quantities, since the crystallinity and internal structure are identical (cross-filled diamonds and star symbols). In case of cross-hatched lamellae, the mobility of chains is restricted in both the crystalline phase, due to a dense chain packing leading to a stronger intermolecular forces, and the amorphous phase, due to the entrapment between the cross-hatched lamellar structure, restricting an overall deformation of the sample and leading to a higher modulus of elasticity and yield stress. On the contrary, the minimal restriction of quasi-globular shape of nodules to the mobility of amorphous chains makes the bulk deformation of the sample easy, which contributes to a lower modulus of elasticity and yield stress. Figure 63 shows a correlation between the modulus of elasticity and yield stress, confirming the reliability of the tensile test data and its relation to the structure and morphology of iPP. Yield stress and modulus of elasticity are linearly related to each other (yield stress = 0.0225×modulus of elasticity) with the observed proportionality constant of 0.0225 [157], being close to the value of about 0.025 reported in the literature

for a larger number of polymers [168]. A sample with a lower modulus of elasticity shows a lower yield stress and vice versa. Interestingly, data of samples of different history of crystallization fit a single line, indicating that identical structural parameters, i.e., primarily the crystallinity and crystal morphology, control the modulus of elasticity and yield stress of iPP, and, in general, the deformation behavior of iPP.

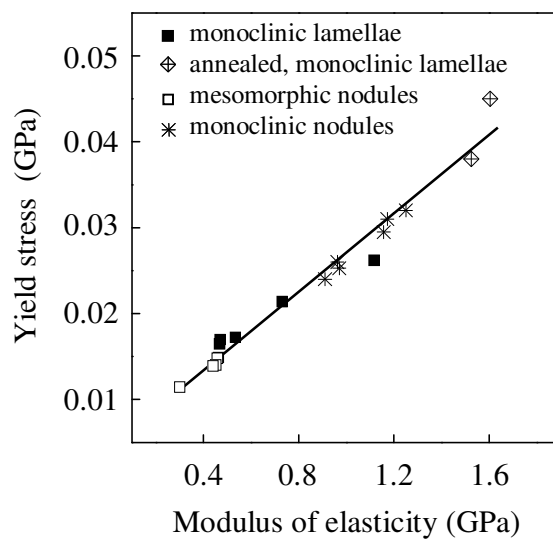


**Figure 63.** A correlation between the yield stress and modulus of elasticity of iPP samples of different structure and morphology.

### 7.3. Effect of structure at micrometer and nanometer scale on light transmission

Figure 64 (left) shows the light transmission of iPP of different history of crystallization, as a function of the wavelength. The light transmission spectrum shifts systematically to higher transmission values, apparently, due to a decrease of crystallinity, in combination with a simultaneous change from a spherulitic to a non-spherulitic superstructure. Additionally, a decrease of transparency is observed on decreasing the wavelength of light, being more evident in presence of spherulites. In detail, a spherulitic preparation (bottom thick line) of crystallinity of about 60 % shows a transparency of between about 40 %, at a wavelength of 380 nm, and about 60 %, at a wavelength of 750 nm. In contrast, a non-spherulitic preparation (top thick line) of crystallinity of about 40 % shows a transparency of about 91 %, at a wavelength of 380 nm, and about 93 %, at a wavelength of 750 nm. Since, a spherulitic preparation is

connected with the formation of monoclinic lamellae and a non-spherulitic preparation is connected with the formation of mesomorphic nodules, therefore, the shift of light transmission spectrum to higher transmission values, can apparently be due to a change from monoclinic to mesomorphic structure, from lamellar to nodular morphology, from spherulitic to non-spherulitic superstructure, and additionally due to a decrease of crystallinity. These parameters may also result in an increased scattering of light waves of smaller wavelength, thereby, decreasing the light transmission of iPP. In order to characterize a more precise influence of these parameters on the light transmission of iPP, annealing of selected preparations was performed, which rather allows to independently control these parameters [169].

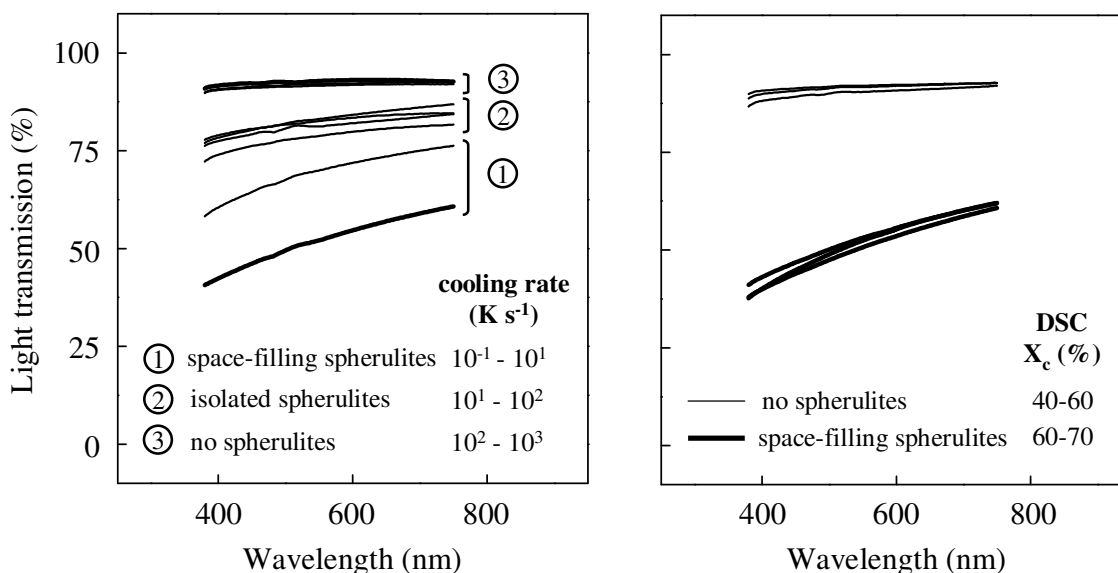


**Figure 64.** Light transmission of melt-crystallized (left) and annealed (right) films of iPP, as a function of wavelength, details in text. Information about the enthalpy-based crystallinity and the spherulitic superstructure is included.

Figure 64 (right) shows the light transmission spectra of initially spherulitic (thick bottom lines) and non-spherulitic (thin top lines) preparations of iPP, before and after annealing at 393 and 433 K. The annealing time was 60 minutes. The spectra of non-spherulitic and spherulitic preparations before and after annealing are not distinguished, since the change of light transmission after annealing is below about 3 %, which is

considered within the limit of experimental error. In detail, a non-spherulitic film, after annealing, is characterized by an increase of crystallinity from about 40-60 %, a change from mesomorphic nodules to monoclinic nodules of increased size, the preservation of non-spherulitic superstructure, and an unchanged light transmission of about 90-91 %. The spherulitic preparation, after annealing, also shows an increase of crystallinity from about 60-70 %, the increase of the size of monoclinic lamellae, preservation of spherulitic superstructure, and nearly identical light transmission of between about 40-60 %, within the investigated range of the wavelength of light. The data of Figure 64 (right) demonstrates an independence of transparency on the structure, since the light transmission of iPP with mesomorphic and monoclinic nodules is identical, and also on an increase or decrease of crystallinity, which is true at least in the visible light wavelength range. This observation allows the simplification of data to a direct dependence of the light transmission of iPP on the crystal morphology and the size of spherulite.

Recently, analysis of the light transmission of iPP and its random copolymers with 1-butene was performed, between the wavelength of about 200–800 nm. It was observed that a non-spherulitic preparation, obtained by quenching the melt, results in a transparency of about 90 %. In contrast, the light transmission was decreased to about 50-60 %, on slow melt-crystallization, due to the presence of spherulites. The variation of crystallinity and the size of crystals were suggested to have no influence on the light transmission of iPP and its random copolymers with 1-butene [170]. In general, the effect of the presence of spherulites on light transmission has been investigated for a number of semicrystalline polymers, with a conclusion that a bigger spherulite will result in a larger scattering of the visible light. The scattering of light can also result from the disordered orientation of crystals within the spherulites. This conclusion was drawn, since a quenched-rolled PE film appeared transparent due to the absence of spherulites and due to the presence of oriented and aligned lamellar structure, which is optically less heterogeneous [103,171-173]. In this context, it is considered that the nodules, embedded in an isotropic amorphous matrix, form an optically homogenous structure, since the globular shape of nodules do not result in an orientational disorder of crystals. This leads to a minor loss of transparency, with a decrease of the wavelength of light. A more distinct loss of light transmission of a spherulitic preparation, with a decrease of the wavelength, is due to the disordered orientation of lamellar crystals within spherulites,

which results in an optically heterogeneous structure. These observations hold for the investigated range of light wavelength. A continuous decrease of wavelength, i.e., the wavelength approaching the size of crystals, can result in a distinct loss of transparency, due to scattering at molecular level.

In order to analyze the effect of the size of spherulites on transparency, additional samples were prepared by isothermal melt-crystallization, in order to obtain a large range of the size of spherulites. Figure 65 shows the polarizing optical micrographs of 100  $\mu\text{m}$  thick iPP films, isothermally melt-crystallized at (a) 413 K, (b) 398 K, (c) 383 K, and (d) 348 K (top series), and non-isothermally melt-crystallized at (e) 0.1  $\text{K s}^{-1}$ , (f) 6  $\text{K s}^{-1}$ , (g) 12  $\text{K s}^{-1}$ , and (h) 450  $\text{K s}^{-1}$ . The size of spherulites decreases on decreasing the temperature of isothermal melt-crystallization, as well as, on increasing the rate of cooling from the melt, which is equivalent to a decrease of crystallization temperature.

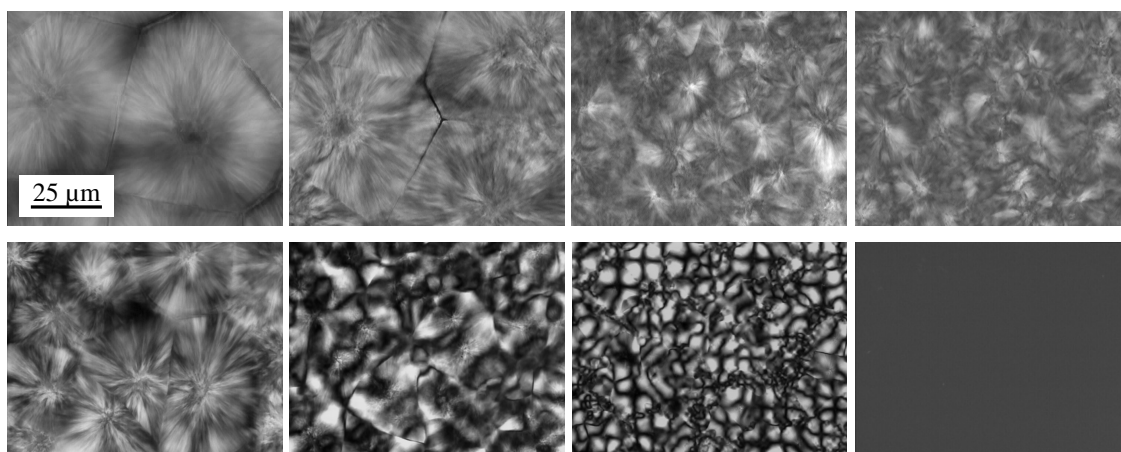


**Figure 65.** Polarizing optical micrographs of isothermally (top series) and non-isothermally melt-crystallized iPP (bottom series), details in text. The scale bar is applicable to all images.

Figure 66 shows the transparency of iPP films, at a wavelength of 500 nm, as a function of the size of spherulites. The open and filled squares represent data which were obtained on non-isothermally and isothermally melt-crystallized samples, respectively, and the stars represent data obtained on annealed preparations. Encircling of data points is intended to illustrate absent effect of annealing, i.e., of absent effect of changes of the structure at the nanometer scale on the light transmission, since annealing leads to an

increase of crystal size without affecting the superstructure. A minimum transparency of about 25 % is observed for an iPP film with an average spherulite size of about 100  $\mu\text{m}$ . The transparency increases to about 75 %, if the size of spherulites decreases to about 20  $\mu\text{m}$ . The data obtained on spherulitic samples of different history of crystallization fit an almost linear relationship, indicating independence of transparency on the exact method of film preparation. In addition, extrapolation to zero spherulite size (dotted line) yields the value which is experimentally obtained on the non-spherulitic preparations. The data of Figure 66 clearly shows that the transparency of iPP films is primarily controlled by the size of spherulites, where the loss of transparency due to light interaction with the internal structure of spherulites can not be neglected.

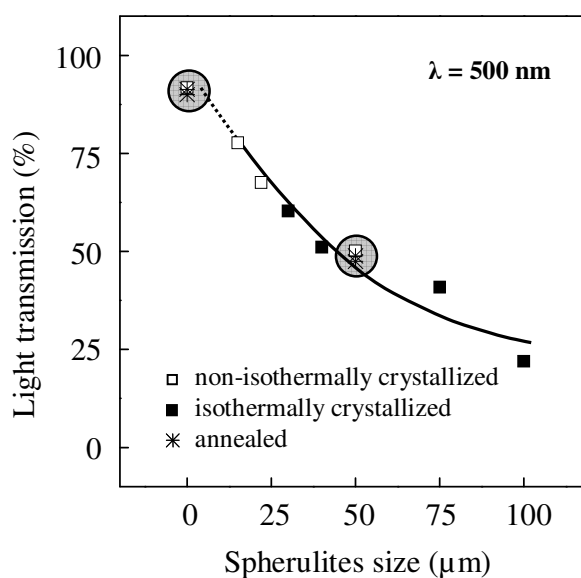


**Figure 66.** Transparency of 100  $\mu\text{m}$  thick films of iPP, at a wavelength of 500 nm, as a function of the size of spherulites, details in text.

A direct evidence of higher transparency of non-spherulitic preparations is demonstrated in Figure 67, which shows the see-through clarity and the spherulitic superstructure of iPP films, initially melt-crystallized at 0.1  $\text{K s}^{-1}$  (top images) and 450  $\text{K s}^{-1}$  (bottom images) before (left) and after (right) annealing at 433 K. The annealing time was 60 minutes. Rectangles are drawn in Figure 67 for a better identification of iPP films. It is evident that the formation of a spherulitic superstructure results in a major loss

of transparency, whereas a high see-through clarity is observed in absence of spherulites. Since the see-through clarity of iPP films do not change on annealing, this can advantageously be used to adjust the crystallinity, thus the properties of iPP, in a wide range. For instance highly transparent and tough films of iPP are obtained by fast cooling of the melt, without the addition of nucleating agents.

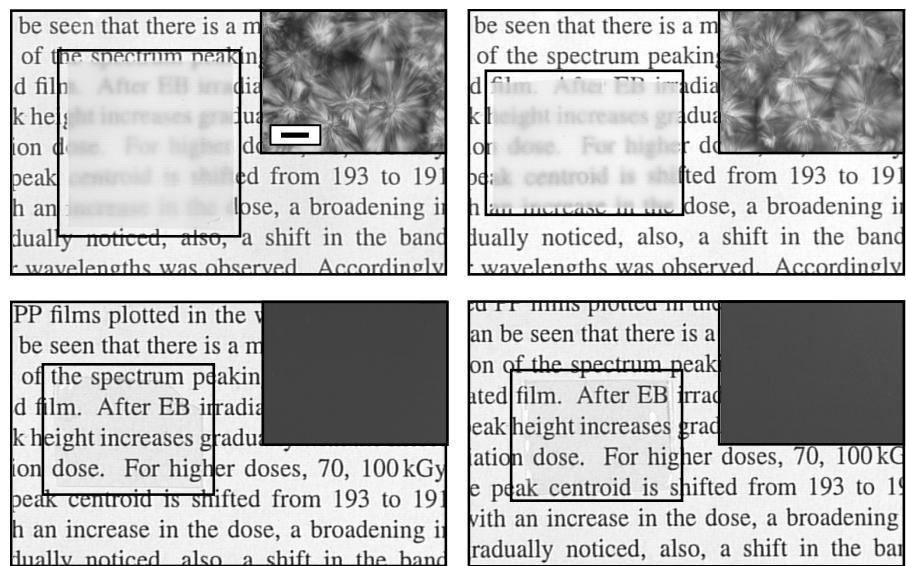


**Figure 67.** See-through clarity and spherulitic superstructure of iPP films, initially melt-crystallized at  $0.1 \text{ K s}^{-1}$  (top) and  $450 \text{ K s}^{-1}$  (bottom) before (left) and after (right) annealing at  $433 \text{ K}$ , for 60 minutes, details in text. The scale bar represents  $20 \mu\text{m}$  for all images.

## 8. Nodular morphology – A general phenomenon in semicrystalline polymers

The results presented in this thesis, unambiguously, show that a nodular morphology of iPP offers unique properties, which, otherwise, are not possible if lamellae are present. This observation strongly motivates to investigate other semicrystalline polymers, in order to obtain a non-lamellar crystal morphology and to identify its effect on properties, to find new areas of application.

### *Materials*

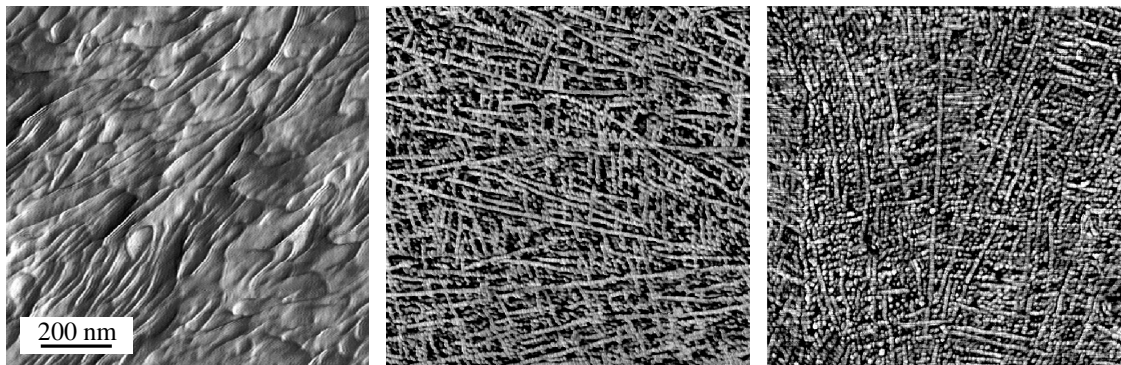
Semicrystalline polymers used were PET (Polyscience), and two random copolymers of iPP with 6 mol-% of 1-butene (Sigma Aldrich), and 6.8 mol-% of ethylene (Borealis). These polymers are named as iPP-bu6 and iPP-eth6.8, respectively. Film thickness was 100  $\mu\text{m}$ . PET films were prepared, in absence of air, either by slow cooling of the melt at 1  $\text{K min}^{-1}$  or by quenching in ice-water. Subsequent annealing was performed at 373 K. Films of iPP with 1-butene and ethylene were melt-crystallized at 0.1  $\text{K s}^{-1}$  and above about 750  $\text{K s}^{-1}$ , in a nitrogen atmosphere using the cooling device. Annealing of iPP-bu6 and iPP-eth6.8 films was performed at 408 and 398 K, respectively, for 60 minutes.

### *Crystal morphology*

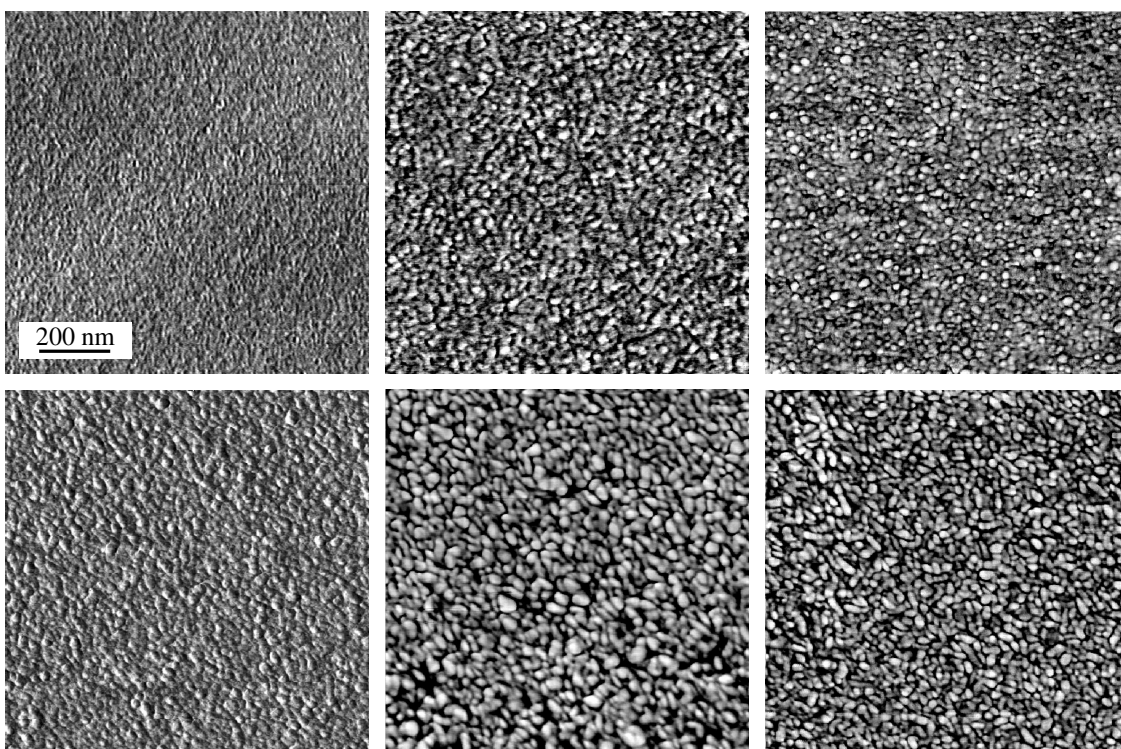
Figure 68 shows phase-mode AFM-images of melt-crystallized PET (left), iPP-bu6 (center) and iPP-eth6.8 (left). The rate of melt-crystallization, in case of PET, was 1  $\text{K min}^{-1}$ , whereas the copolymers of iPP were melt-crystallized at 0.1  $\text{K s}^{-1}$ . All the investigated polymers show a lamellar crystal morphology, on slow cooling of the melt. The lamellae of PET adopted both edge-on and flat-on orientations, which makes the thickness determination difficult, however, the estimated thickness of the edge-on lamellae is about 12 nm. Films of random copolymers of iPP reveal a cross-hatched lamellar morphology, similar to what is observed in case of iPP homopolymer. The thickness of lamellae is about 10 nm.

Figure 69 shows phase-mode AFM-images of rapidly cooled films of PET (left), iPP-bu6 (center) and iPP-eth6.8 (left), before (top series) and after annealing (bottom series). PET film was quenched in ice-water, whereas the copolymers of iPP with 1-butene and ethylene were melt-crystallized at 750 and 880  $\text{K sec}^{-1}$ , respectively. The

temperatures of isothermal annealing for PET, iPP-bu6, and iPP-eth6.8 were 373, 408, and 398 K, respectively, and the annealing time was 60 minutes.



**Figure 68.** Phase-mode AFM-images of slowly melt-crystallized PET (left ), iPP-bu6 (center) and iPP-eth6.8 (left), details in text.



**Figure 69.** Phase-mode AFM-images of rapidly cooled films of PET (left), iPP-bu6 (center) and iPP-eth6.8 (left), before (top series) and after annealing (bottom series), details in text. The scale bar is applicable to all images.

AFM-images show an exclusively nodular morphology, before and after annealing, for all the investigated polymers. The size of nodules in quenched films of PET is below about 10 nm, which increases to about 13 nm after annealing. Similarly, the size of nodules in rapidly cooled films of iPP-bu6 and iPP-eth6.8 is about 13 nm. As a result of annealing, the size of nodules increases to above about 20 nm. AFM-images clearly show that the size of nodules obtained at ambient temperature can be adjusted by the conditions of annealing. As a result, properties different from the lamellar preparations of these polymers are expected. From the results presented in this thesis work and the analysis of published literature, it became clear that the nodular morphology exists in a number of semicrystalline polymers and the formation of nodules can be considered as a general phenomenon in rapidly cooled semicrystalline polymers.

## 9. Summary

The aim of this work was to investigate the formation of the structure and morphology as well as the thermodynamic stability of nodular nano-domains of iPP, in order to establish structure/morphology and properties relations. The idea was to reveal the differences of selected but identical properties of iPP in presence of either lamellae or nodules in an amorphous structure. As a result, it was possible to identify the advantages of preparing iPP films with nodular nano-domains in an amorphous structure. In a first step, films of 100  $\mu\text{m}$  thickness were melt-crystallized in a large range of cooling rates between  $10^{-1}$  to  $10^3$   $\text{K s}^{-1}$ . The film thickness was kept low, in order to obtain a uniform structure and morphology across the film thickness. As expected, iPP samples containing lamellae or nodules in an amorphous structure were obtained, which, in the next step, were further modified by the conditions of subsequent annealing. Finally, the effect of phase structure, crystal size and shape, and superstructure was evaluated on selected properties of iPP. The main results of this thesis are summarized below:

A spherulitic morphology with cross-hatched monoclinic lamellae or a non-spherulitic morphology with mesomorphic nodules is obtained on melt-crystallization at a rate of cooling below about 10 or above about 100  $\text{K s}^{-1}$ , respectively. Simultaneous formation of both monoclinic lamellae and mesomorphic nodules is possible on melt-crystallization at a rate of cooling between 10 and 100  $\text{K s}^{-1}$ .

Temperature-resolved AFM reveals that the mesomorphic-to-monoclinic phase transition, initiating at a temperature of about 350 K, occurs at a local scale within existing domains, without a change of their size or habit. It is also noticed that the initially formed habit of crystals and the presence or absence of spherulites are maintained up to an annealing temperature of about 433 K. The thickness of crystals, independent of the crystal habit, increases non-linearly with an increase of annealing temperature and/or annealing time.

A comparison of melt-crystallized and subsequently annealed films of iPP by AFM and TEM yields, qualitatively and quantitatively, a nearly identical crystal morphology at the surface and in the bulk, respectively.

Analysis of the annealing processes, in time domain, at different temperatures yields proportionality between the increase of crystal size and the irreversible reduction of the apparent specific heat capacity. The initial strong decrease of the apparent specific

heat capacity of iPP with nodular nano-domains is proportional to the temperature of isothermal annealing and is linked to an irreversible reorganization of the structure, i.e., an increase of crystallinity and crystal size. The final value of apparent specific heat capacity is larger at 433 K than at 393 K and continues to decrease gradually, involving an identical process of structural reorganization, which results in an initial decrease of the apparent specific heat capacity.

Study of the melting temperature, using Gibbs-Thomson equation, reveals that nodules, stabilized by annealing at high temperature, exhibit a similar fold-surface as lamellar crystals. The lateral dimension of nodules, if exceeds a critical value of above about 30 nm, do not show a remarkable effect on the temperature of final melting.

Glass transition of the amorphous phase of iPP proves co-existence of rigid amorphous and mobile amorphous structures. An iPP sample with mesomorphic nodules represents lowest crystallinity and highest rigid amorphous fraction. The rigid amorphous fraction decreases with increasing crystallinity due to a reduced covalent coupling of crystals and amorphous phases, which, simultaneously, decreases the glass transition temperature. Extrapolation of the glass transition temperature to a zero rigid amorphous fraction yields a value identical to the glass transition temperature of an amorphous polypropylene. Analysis of the effect of crystal habit allows to identify the structure at the basal planes of crystals as a major source of the immobilization of the amorphous phase, whereas the crystal lateral surfaces do not contribute to this effect.

Tensile-stress strain behavior reveals that the structure-controlled brittle-to-ductile transition goes parallel with a change of crystal morphology from cross-hatched monoclinic lamellae organized in spherulites to mesomorphic nodules forming no spherulites, respectively. The ductile behavior of iPP with nodular nano-domains is maintained between the crystallinity values of 40–60%. Samples of iPP of identical crystallinity and crystal structure but, qualitatively, of different crystal morphology, reveal that a decreased lateral length of crystals offers a less restriction to the mobility of amorphous chains. The deformation process includes the reorientation of nodules, interconnected by tie-molecules, and of the amorphous chains, in the draw direction. As a result, a transition from nodular to fibrillar morphology is observed by in situ AFM. The modulus of elasticity and yield stress increase almost linearly with an increase of

crystallinity. Quantitatively, these properties are lower in iPP samples containing nodular nano-domains in an amorphous structure, revealing a direct effect of the crystal habit.

The light transmission of iPP films, in the visible light wavelength range, is primarily controlled by the size of spherulites, whereas the variation of crystallinity and the size and structure of crystals do not affect the light transmission. This characteristic allows to prepare highly transparent, highly crystalline and tough films of iPP in presence of nodular nano-domains in an amorphous structure, without the addition of special nucleating agents.

The results found in this work show that the formation of nodular nano-domains is not unique to iPP, rather it is observed as a general phenomenon in semicrystalline polymers. In case of iPP, the formation of nodules in an amorphous structure, unambiguously, demonstrates the advantages of obtaining a combination of properties, which for a lamellar preparation of iPP are not possible. Additionally, the presented results are helpful in understanding the cooling rate controlled formation of morphology, i.e., skin-core morphology, and the effect of morphology on properties of industrially processed products of iPP. These results back up a strong motivation of the investigation of other semicrystalline polymers, in order to produce nodular morphology and to identify its effect on properties.

## Symbols and abbreviations

$\alpha_{\text{thermal}}$	<i>thermal expansion coefficient</i>
$\alpha$	<i>monoclinic structure of isotactic polypropylene</i>
$\beta$	<i>hexagonal structure of isotactic polypropylene</i>
$\gamma$	<i>triclinic structure of isotactic polypropylene</i>
$\Theta$	<i>scattering angle</i>
$\rho$	<i>density</i>
$\sigma$	<i>free energy of the lateral surface of a crystal</i>
$\sigma_e$	<i>free energy of the basal plane of a crystal</i>
$C_p$	<i>specific heat capacity</i>
$\Delta h_f$	<i>specific heat of fusion</i>
$I_o$	<i>intensity of incident light</i>
$I_t$	<i>intensity of transmitted light</i>
$l_c$	<i>crystal thickness</i>
$t$	<i>time</i>
$T$	<i>temperature</i>
$\Delta T$	<i>temperature difference</i>
$T_c$	<i>crystallization temperature</i>
$T_m^o$	<i>equilibrium melting temperature</i>
$\Delta T_u$	<i>temperature difference between <math>T_m^o</math> and <math>T_c</math></i>
$T_g$	<i>glass transition temperature</i>
$X_c$	<i>degree of crystallinity</i>
$Cu$	<i>copper</i>
$Be$	<i>beryllium</i>
$AFM$	<i>atomic force microscopy</i>
$DMA$	<i>dynamic-mechanical analysis</i>
$DSC$	<i>differential scanning calorimetry</i>
$iPB$	<i>isotactic polybutene</i>
$iPMMA$	<i>isotactic poly(methyl methacrylate)</i>
$iPP$	<i>isotactic polypropylene</i>
$MAF$	<i>mobile amorphous fraction</i>
$PA$	<i>polyamide</i>
$PBT$	<i>poly(butylene terephthalate)</i>
$PE$	<i>polyethylene</i>
$PET$	<i>poly(ethylene terephthalate)</i>
$PLA$	<i>polylactic acid</i>
$PVDF$	<i>poly(vinylidene fluoride)</i>
$RAF$	<i>rigid amorphous fraction</i>
$SAXS$	<i>small angle X-ray scattering</i>
$TEM$	<i>transmission electron microscopy</i>
$WAXS$	<i>wide angle X-ray scattering</i>

## References

1. V. Graves, Polypropylene: A commodity plastic reaches record highs in 1994 production, *Modern Plastics Encyclopedia 1996*, McGraw Hill, New York, 1995.
2. C.C. Hsu, P.H. Geil, H. Miyaji, K. Asai, Structure and properties of polypropylene crystallized from the glassy state, *J. Polym. Sci. Polym. Phys.* 2379, 24, 1986.
3. F. DeSantis, S. Adamovsky, G. Titomanlio, C. Schick, Scanning nanocalorimetry at high cooling rate of isotactic polypropylene, *Macromolecules* 2562, 39, 2006.
4. C. Maier, T. Calafut, *Polypropylene: The definitive user's guide and data book*, *Plastics Design Library*, New York, 1998.
5. R. Rastogi, W.P. Vellinga, S. Rastogi, C. Schick, H.E.H. Meijer, The three-phase structure and mechanical properties of poly(ethylene terephthalate), *J. Polym. Sci. Polym. Phys.* 2092, 42, 2004.
6. R. Androsch, B. Wunderlich, The link between rigid amorphous fraction and crystal perfection in cold-crystallized poly(ethylene terephthalate), *Polymer* 12556, 46, 2005.
7. M.L. DiLorenzo, M.C. Righetti, The three-phase structure of isotactic poly(1-butene), *Polymer* 1323, 49, 2008.
8. B. Wunderlich, *Thermal analysis of polymeric materials*, Springer, Berlin, 2005.
9. G. Strobl, *The physics of polymers*, Springer, Berlin, 1997.
10. J.M. Schultz, *Polymer crystallization: The development of crystalline order in the thermoplastic polymers*, Oxford University Press, New York, 2001.
11. B. Wunderlich, *Macromolecular physics: Crystal nucleation, growth, annealing*, Vol. 2, Academic Press, New York, 1973.
12. J.R. Fried, *Polymer science and technology*, Prentice Hall, New Jersey, 1995.
13. J.A. Brydson, *Plastics materials*, 7th edition, Butterworth-Heinemann, Oxford, 1999.
14. A. Sharples, *Introduction to polymers crystallization*, Edward-Arnold, London, 1966.
15. L. Yan, Q. Zhu, Direct observation of the fringed micelles structure of cellulose molecules solvated in dimethylacetamide/LiCl system, *Polym. Int.* 738, 51, 2002.

16. B. Wunderlich, *Macromolecular physics: Crystal structure, morphology, defects*, Vol. 1, Academic Press, New York, 1973.
17. F.W. Billmeyer, *Textbook of polymer science*, 3rd edition, Wiley Interscience, New York, 1984.
18. P.H. Geil, *Polymer single crystals*, Wiley Interscience, New York, 1963.
19. D.T. Grubb, A. Keller, Lamellar morphology of polyethylene: Electron microscopy of a melt-crystallized sharp fraction, *J. Polym. Sci. Polym. Phys.* 207, 18, 1980.
20. H.F. Mark, N.G. Gaylord, N.M. Bikales, *Encyclopedia of polymer science and technology*, Vols. 8-9, Wiley Interscience, New York, 1968.
21. D.R. Uhlmann, Electron microscopy and SAXS studies of amorphous polymers, *Faraday Disc. Chem. Soc.* 87, 68, 1979.
22. T. Ogawa, H. Miyaji, K. Asai, Nodular morphology of quenched polypropylene, *J. Phys. Soc. Jpn.* 3668, 54, 1985.
23. H. Miyaji, P.H. Geil, Annealing of nodular linear polyethylene crystallized from the glass, *Polymer* 701, 22, 1981.
24. C.C. Hsu, P.H. Geil, H. Miyaji, K. Asai, Structure and properties of polybutylene crystallized from the glassy state. II. Electron microscopy, *J. Macromol. Sci. Phys.* 467, 25, 1986.
25. C.C. Hsu, P.H. Geil, Morphology and crystal structure of poly(vinylidene fluoride), *Polym. Commun.* 27, 105, 1986.
26. G.S.Y. Yeh, P.H. Geil, Crystallization of poly(ethylene terephthalate) from the glassy amorphous state, *J. Macromol. Sci. Phys.* 235, 1, 1967.
27. J.J. Klement, P.H. Geil, Deformation and annealing behavior. III. Thin films of polycarbonate, isotactic polymethyl methacrylate, and isotactic polystyrene, *J. Macromol. Sci. Phys.* 31, 6, 1972.
28. M. Imai, K. Kaji, Polymer crystallization from the metastable melt: The formation mechanism of spherulites, *Polymer* 5544, 47, 2006.
29. M. Pluta, A. Galeski, Crystalline and supermolecular structure of polylactide in relation to the crystallization method, *J. App. Polym. Sci.* 1386, 86, 2002.
30. S.Z.D. Cheng, R. Pan, B. Wunderlich, Thermal analysis of poly(butylene terephthalate) for heat capacity, rigid amorphous content and transition behavior, *Makromol. Chemie* 2443, 189, 1988.

31. R. Androsch, B. Wunderlich, Scanning calorimetry, in: K. Matyjaszewski, Y. Gnanou, L. Leibler (Eds.), *Macromolecular engineering: Precise synthesis, materials properties, applications*, Vol. 3, Wiley-VCH, Weinheim, 2007.
32. B. Wunderlich, Reversible crystallization and the rigid amorphous phase in semicrystalline macromolecules, *Prog. Polym. Sci.* 383, 28, 2003.
33. B. Wunderlich, Evidence for coupling and decoupling of parts of macromolecules by temperature-modulated calorimetry, *J. Polym. Sci. Polym. Phys.* 1275, 42, 2004.
34. B. Wunderlich, Effect of decoupling of molecular segments, microscopic stress-transfer and confinement of the nanophases in semicrystalline polymers, *Macromol. Rapid Commun.* 1521, 26, 2005.
35. B. Wunderlich, The ATHAS database on heat capacities of polymers, *Pure Appl. Chem.* 1019, 67, 1995. ATHAS data bank, <http://athas.prz.edu.pl/>, M. Pyda (Ed.), 2009.
36. J. Varga, Review: Supermolecular structure of isotactic polypropylene, *J. Mat. Sci.* 2557, 27, 1992.
37. J. Karger-Kocsis, *Polypropylene: An A-Z Reference*, Academic-Publishers, London, 1999.
38. G. Natta, P. Corradini, Structure and properties of isotactic polypropylene, *Nuovo Cimento Suppl.* 40, 15, 1960.
39. S. Brückner, S.V. Meille, I.V. Petraccone, B. Pirozzi, Polymorphism in isotactic polypropylene, *Prog. Polym. Sci.* 361, 16, 1991.
40. B. Lotz, S. Kopp, D.C.R. Dorset, Original crystal structure of polymers with ternary helices, *Acad. Sci.* 187, 319, 1994.
41. S.V. Meille, D.R. Ferro, S. Brückner, A.J. Lovinger, F.J. Padden, Structure of  $\gamma$ -isotactic polypropylene: A long-standing structural puzzle, *Macromolecules* 2615, 27, 1994.
42. B. Lotz, J.C. Wittmann, A.J. Lovinger, Structure and morphology of poly(propylenes): A molecular analysis, *Polymer* 4979, 37, 1996.
43. M.A. Gomez, H. Tanaka, E. Tonelli, High-resolution solid-state  $^{13}\text{C}$  nuclear magnetic resonance study of isotactic polypropylene polymorphs, *Polymer* 2227, 28, 1987.

44. S. Brückner, S.V. Meille, Non-parallel chains in crystalline  $\gamma$ -isotactic polypropylene, *Nature* 455, 340, 1989.
45. Y. Nozue, Y. Shinohara, Y. Ogawa, T. Sakurai, H. Hori, T. Kasahara, N. Yamaguchi, N. Yagi, Y. Amemiya, Deformation behavior of isotactic polypropylene spherulite during hot drawing investigated by simultaneous microbeam SAXS-WAXS and POM measurement, *Macromolecules* 2036, 40, 2007.
46. A. Turner-Jones, J.M. Aizlewood, D.R. Becket, Crystalline forms of isotactic polypropylene, *Macromol. Chem.* 134, 75, 1964.
47. B. Lotz, J.C. Wittmann, The molecular origin of lamellar branching in the  $\alpha$ -monoclinic form of isotactic polypropylene, *J. Polym. Sci. Polym. Phys.* 1541, 24, 1986.
48. P. Maiti, M. Hikosaka, K. Yamada, A. Toda, F. Gu, Lamellar thickening in isotactic polypropylene with high tacticity crystallized at high temperature, *Macromolecules* 9069, 33, 2000.
49. J. Karger-Kocsis, Structure and morphology in polypropylene: Structure, blends and composites, Vol.1, Chapman and Hall, London, 1995.
50. D.R. Norton, A. Keller, The spherulitic and lamellar morphology of melt-crystallized isotactic polypropylene, *Polymer* 704, 26, 1985.
51. F.J. Padden, H.D. Keith, Spherulitic crystallization in polypropylene, *J. Appl. Phys.* 1479, 30, 1959.
52. J.X. Li, W.L. Cheung, RuO<sub>4</sub> staining and lamellar structure of  $\alpha$ - and  $\beta$ -PP, *J. Appl. Polym. Sci.* 1529, 72, 1999.
53. W. Stocker, S.N. Magonov, H.J. Cantow, J.C. Wittmann, B. Lotz, Contact faces of epitaxially crystallized  $\alpha$ - and  $\gamma$ -phase isotactic polypropylene observed by atomic force microscopy, *Macromolecules* 5915, 26, 1993.
54. J. Varga,  $\beta$ -modification of polypropylene and its two-component system, *J. Thermal Analysis* 1891, 35, 1989.
55. J. Varga,  $\beta$ -modification of isotactic polypropylene: Preparation, structure, processing, properties, and application, *J. Macromol. Sci. Phys.* 1121, 41, 2002.
56. E.P. Moore, Polypropylene handbook, Hanser Publishers, Munich, 1996.

57. K. Mezghani, P.J. Phillips, The  $\gamma$ -phase of high molecular weight isotactic polypropylene. II: The morphology of the  $\gamma$ -form crystallized at 200 MPa, *Polymer* 5725, 38, 1997.
58. B. Lotz, S. Graff, C. Straupé, J.C. Wittmann, Single crystals of  $\gamma$ -phase isotactic polypropylene, combined diffraction and morphological support for a structure with non-parallel chains, *Polymer* 2902, 32, 1991.
59. P. Corradini, V. Petraccone, C. De-Rosa, G. Guerra, On the structure of the quenched mesomorphic phase of isotactic polypropylene, *Macromolecules* 2699, 19, 1986.
60. R.L. Miller, On the existence of near-range order in isotactic polypropylenes, *Polymer*, 135, 1, 1960.
61. J. Grebowicz, S.F. Lau, B. Wunderlich, The thermal properties of polypropylene, *J. Polym. Sci. Polym. Symp.* 19, 71, 1984.
62. D.M. Gezovich, P.H. Geil, Morphology of quenched polypropylene, *Polym. Eng. Sci.* 202, 8, 1968.
63. G. Bodor, M. Grell, A. Kallo, Determination of the crystallinity of polypropylene, *Faserforsch Textiltechnik* 527, 15, 1964.
64. V. Caldas, G.R. Brown, R.S. Nohr, J.G. MacDonald, L.E. Raboin, The structure of the mesomorphic phase of quenched isotactic polypropylene, *Polymer* 899, 35, 1994.
65. I. Coccorullo, R. Pantani, G. Titomanlio, Crystallization kinetics and solidified structure in iPP under high cooling rates, *Polymer* 307, 44, 2003.
66. P.B. McAllister, T.J. Carter, R.M. Hinde, Structure of the quenched form of polypropylene, *J. Polym. Sci. Polym. Phys.* 49, 16, 1978.
67. D.T. Grubb, D.Y. Yoon, Morphology of quenched and annealed isotactic polypropylene, *Polym. Commun.* 84, 27, 1986.
68. M. Pluta, M. Kryszeński, Influence of thermal treatment on the crystalline and supermolecular structure of isotactic polypropylene, *Acta Polymerica* 726, 37, 1986.
69. R. Androsch, B. Wunderlich, Reversible crystallization and melting at the lateral surface of isotactic polypropylene crystals, *Macromolecules* 5950, 34, 2001.

70. D. Ferrer-Balas, M.L. MasPOCH, A.B. Martinez, O.O. Santana, Influence of annealing on the microstructural, tensile and fracture properties of polypropylene films, *Polymer* 1697, 42, 2001.
71. Z.G. Wang, B.S. Hsaio, S. Srinivas, G.M. Brown, A.H. Tsou, S.Z.D. Cheng, R.S. Stein, Phase transformation in quenched mesomorphic isotactic polypropylene, *Polymer* 7561, 42, 2001.
72. R. Seguela, E. Staniek, B. Escaig, B. Fillon, Plastic deformation of polypropylene in relation to crystalline structure, *J. Appl. Polym. Sci.* 1873, 71, 1999.
73. V. Vittoria, Effect of annealing on the structure of quenched isotactic polypropylene, *J. Macromol. Sci. Phys.* 489, 28, 1989.
74. R. Zannetti, G. Celotti, A. Fichera, R. Francesconi, Structural effects of annealing time and temperature on the paracrystal-crystal transition in isotactic polypropylene, *Makromol. Chem.* 137, 128, 1969.
75. D. Dudić, D. Kostoski, V. Djoković, M.D. Dramićanin, Formation and behavior of low-temperature melting peak of quenched and annealed isotactic polypropylene, *Polym. Int.* 111, 51, 2001.
76. C. Jourdan, J.Y. Cavaille, J. Perez, Mechanical relaxations in polypropylene: A new experimental and theoretical approach, *J. Polym. Sci. Polym. Phys.* 2361, 27, 1989.
77. A. Fichera, R. Zannetti, Thermal properties of isotactic polypropylene quenched from the melt and annealed, *Makromol. Chemie* 1885, 176, 1975.
78. V. La-Carrubba, V. Brucato, S. Piccarolo, Influence of “Controlled Processing Conditions” on the solidification of iPP, PET and PA 6, *Macromol. Symp.* 43, 180, 2002.
79. D. Tranchida, Z. Kiflie, S. Piccarolo, Mechanical properties of the nanometer scale precrystalline order of a poly(ethylene terephthalate)/poly(ethylene naphthalate) blend, *Macromol. Rapid Commun.* 1584, 27, 2006.
80. V. Brucato, S. Piccarolo, V. La-Carrubba, An experimental methodology to study polymer crystallization under processing conditions. The influence of high cooling rates, *Chem. Engg. Sci.* 4129, 57, 2002.
81. S. Piccarolo, V. Brucato, Z. Kiflie, Non-isothermal crystallization kinetics of PET, *Polymer Engg. Sci.* 1263, 40, 2000.

82. D. Scharnowski, Characterization of the influence of cooling rates on structure and properties of dynamic vulcanizates, Ph.D. Thesis, Martin-Luther-University, Halle-Wittenberg, Germany, 2005.
83. D.A. Ivanov, Z. Amalou, S.N. Magonov, Real-time evolution of the lamellar organization of poly(ethyleneterephthalate) during crystallization from the melt: High-temperature atomic force microscopy study, *Macromolecules* 8944, 34, 2001.
84. H.G. Haubruge, R. Daussin, A.M. Jonas, R. Legras, Morphological study of melt-crystallized poly(ethylene terephthalate): B. Thin films, *Polymer* 8053, 44, 2003.
85. S. Lee, H. Miyaji, P.H. Geil, Morphology of amorphous poly(ethylene terephthalate), *J. Macromol. Sci. Phys.* 489, 22, 1983.
86. J.A. Gailey, R.H. Ralston, The quenched state of polypropylene, *Polym. Engg. Sci.* 29, 4, 1964.
87. S. Piccarolo, S. Alessi, V. Brucato, G. Titomanlio, Crystallization behavior at high cooling rates of two polypropylenes: In *Crystallization of Polymers*, Academic-Publishers, Dordrecht, 1993.
88. A. Martorana, S. Piccarolo, F. Scichilone, The X-ray determination of the amounts of the phases in samples of isotactic polypropylene quenched from the melt at different cooling rates, *Makromol. Chem. Phys.* 597, 198, 1997.
89. N. Alberola, M. Fugier, D. Petit, B. Fillon, Microstructure of quenched and annealed films of isotactic polypropylene. Part I, *J. Mat. Sci.* 1187, 30, 1995.
90. T. Koch, S. Seidler, E. Halwax, S. Bernstorff, Microhardness of quenched and annealed isotactic polypropylene, *J. Mater. Sci.* 5318, 42, 2007.
91. A. Ferrero, E. Ferracini, A. Mazzavillani, V. Malta, A new X-ray study of the quenched isotactic polypropylene transition by annealing, *J. Macromol. Sci. Phys.* 109, 39, 2000.
92. S.Z.D. Cheng, M.Y. Cao, B. Wunderlich, Glass transition and melting behavior of poly(oxy -1, 4 - phenyleneoxy - 1, 4 - phenylenecarbonyl - 1, 4 - phenylene), *Macromolecules* 1868, 19, 1986.
93. S.Z.D. Cheng, B. Wunderlich, Glass Transition and Melting Behavior of Poly(ethylene-2,6-naphthalenedicarboxylate), *Macromolecules* 789, 21, 1988.
94. S. Fakirov, D. Stahl, Structure and properties of poly(ethylene terephthalate) crystallized by annealing in the highly oriented state, *Angew. Makromol. Chemie* 117, 102, 1982.

95. S. Nishimoto, T. Kagiya, Y. Watanabe, M. Kato, Material design of radiation resistant polypropylene: Part II-Importance of the smectic structure produced by quenching treatment, *Polym. Degrad. Stabil.* 199, 14, 1986.
96. F. De-Candia, R. Russo, V. Vittoria, Mechanical behavior of quenched isotactic polypropylene crystallized by thermal and solvent treatments, *J. Appl. Polym. Sci.* 689, 34, 1987.
97. S. Piccarolo, Ageing of isotactic polypropylene due to morphology evolution, experimental limitations of realtime density measurements with a gradient column, *Polymer* 5610, 47, 2006.
98. A. Galeski, Strength and toughness of crystalline polymer systems, *Prog. Polym. Sci.* 1643, 28, 2003.
99. J.T. Graham, R.G. Alamo, L. Mandelkern, The effect of molecular weight and crystalline structure on yielding in ethylene copolymers, *J. Polym. Sci. Polym. Phys.* 213, 35, 1997.
100. G.M. Wallner, K. Resch, C. Teichert, M. Gahleitner, W. Binder, Effect of material structure and additives on the optical properties of PP cast films, *Monatshefte für Chemie* 887, 137, 2006.
101. R. Pritchard, The transparency of crystalline polymers, *Polym. Engg. Sci.* 66, 4, 1964.
102. F.H. Norris, R.S. Stein, Scattering of light from thin polymer films. IV. Scattering from oriented polymers, *J. Polym. Sci.* 87, 27, 1958.
103. R.E. Prud'homme, D. Yoon, R.S. Stein, Scattering of light from spherulitic polymers: Effect of internal structure, *J. Polym. Sci. Polym. Phys.* 1047, 11, 1973.
104. J. Wang, Q. Dou, Crystallization behavior and optical and mechanical properties of isotactic polypropylene nucleated with rosin-based nucleating agents, *Polym. Int.* 233, 57, 2008.
105. A. Romankiewicz, T. Sterzynski, W. Brostow, Structural characterization of  $\alpha$ - and  $\beta$ -nucleated isotactic polypropylene, *Polym. Int.* 2086, 53, 2004.
106. M. Blomenhofer, S. Ganzleben, D. Hanft, H.W. Schmidt, M. Kristiansen, P. Smith, K. Stoll, D. Malder, K. Hoffmann, "Designer" Nucleating agents for polypropylene, *Macromolecules* 3688, 38, 2005.
107. M. Tenma, M. Yamaguchi, Structure and properties of injection-molded polypropylene with sorbitol-based clarifier, *Polym. Engg. Sci.* 1441, 47, 2007.

108. H. Wang, C.C. Li, D. Zhang, Z.Y. Li, Effects of rosin-type co-crystal nucleating agents on the crystallization process and the properties of polypropylene, *J. Appl. Polym. Sci.* 2137, 89, 2003.
109. S. Piccarolo, Morphological changes in isotactic polypropylene as a function of cooling rate, *J. Macromol. Sci. Phys.* 501, 31, 1992.
110. J. Brandrup, E.H. Immergut, E.A. Grulke, *Polymer handbook*, Vol. 1, Wiley Interscience, New York, 1999.
111. J.K. Hobbs, Following crystallization in polymers using AFM, in: J.U. Sommer, G. Reiter, *Polymer crystallization: Observations, concepts and interpretations*, Springer, Berlin, 2003.
112. D. Montezinos, B.G. Wells, J.L. Burns, The use of ruthenium in hypochlorite as a stain for polymeric materials, *J. Polym. Sci. Polym. Lett.* 421, 23, 1985.
113. R. Androsch, I. Moon, S. Kreitmeier, B. Wunderlich, Determination of heat capacity with a sawtooth-type, power-compensated temperature-modulated DSC, *Thermochim. Acta* 357, 267, 2000.
114. R. Androsch, B. Wunderlich, Temperature-modulated DSC using higher harmonics of the Fourier transform, *Thermochim. Acta* 333, 27, 1999.
115. J. Qiu, Z. Wang, L. Yang, J. Zhao, Y. Niu, B.S. Hsiao, Deformation-induced highly oriented and stable mesomorphic phase in quenched isotactic polypropylene, *Polymer* 6934, 48, 2007.
116. J.H. Bheda, J.E. Spruiell, The effect of process and polymer variables on the light transmission properties of polypropylene tubular blown films, *Polym. Engg. Sci.* 736, 26, 1986.
117. Q. Zia, R. Androsch, H.-J. Radusch, S. Piccarolo, Morphology, reorganization and stability of mesomorphic nanocrystals in isotactic polypropylene, *Polymer* 8163, 47, 2006.
118. J.A. Koutsky, A.G. Walton, E. Bear, Nucleation of polymer droplets, *J. Appl. Phys.* 1832, 38, 1967.
119. C. Silvestre, S. Cimmino, D. Duraccio, C. Schick, Isothermal crystallization of isotactic polypropylene studied by superfast calorimetry, *Macromol. Rapid Commun.* 875, 28, 2007.
120. A.I. Isayev, B.F. Catignani, Crystallization and microstructure in quenched slabs of various molecular weight polypropylenes, *Polym. Engg. Sci.* 1526, 37, 1997.

121. C.C. Hsu, P.H. Geil, Morphology-structure-property relationship in ultraquenched poly(vinylidene fluoride), *J. Appl. Phys.* 2404, 56, 1984.
122. Q. Zia, R. Androsch, H.-J. Radusch, E. Ingolič, Crystal morphology of rapidly cooled isotactic polypropylene: A comparative study by TEM and AFM, *Polym. Bull.* 791, 60, 2008.
123. Q. Zia, R. Androsch, Effect of atomic force microscopy (AFM) tip geometry on the evaluation of the crystal size of semicrystalline polymers, *Meas. Sci. Tech.* 097003, 20, 2009.
124. R. Androsch, In situ atomic force microscopy of the mesomorphic-monoclinic phase transition in isotactic polypropylene, *Macromolecules* 533, 41, 2008.
125. C. Marega, V. Causin, A. Marigo, A SAXS-WAXD study on the mesomorphic- $\alpha$  transition of isotactic polypropylene, *J. Appl. Polym. Sci.* 32, 109, 2008.
126. C. De-Rosa, G. Guerra, V. Petraccone, R. Centore, P. Corradini, Temperature dependence of the intramolecular disorder in the high-temperature phase of poly(tetrafluoroethylene) (Phase I), *Macromolecules* 1174, 21, 1988.
127. I.C. Sanchez, J.P. Colson, R.K. Egly, Theory and observations of polymer crystal thickening, *J. Appl. Phys.* 4332, 44, 1973.
128. D.H. Reneker, Point dislocations in crystals of high polymers, *J. Polym. Sci.* S39, 59, 1962.
129. A. Peterlin, Molecular weight dependence of isothermal long period growth of polyethylene single crystals, *Polymer* 25, 6, 1965.
130. E.W. Fischer, G.F. Schmidt, The long period in stretched polyethylene, *Angew. Chemie* 551, 74, 1962.
131. A. Ferrero, E. Ferracini, R. Hosemann, Small-angle scattering of microparacrystal-bundles in cold-drawn and annealed isotactic polypropylene, *Polymer* 1747, 25, 1984.
132. D. Sawai, M. Miyamoto, T. Kanamoto, M. Ito, Lamellar thickening in nascent poly(acrylonitrile) upon annealing, *J. Polym. Sci. Polym. Phys.* 2571, 38, 2000.
133. A. Martorana, S. Piccarolo, D. Sapoundjieva, SAXS/WAXS study of the annealing process in quenched samples of isotactic polypropylene, *Macromol. Chem. Phys.* 531, 200, 1999.
134. L. Poussin, Y.A. Bertin, J. Parisot, C. Brassy, Influence of thermal treatment on the structure of an isotactic polypropylene, *Polymer* 4261, 39, 1998.

135. C. Hedesiu, D.E. Demco, R. Kleppinger, G.V. Poel, W. Gijsbers, B. Blumich, K. Remerie, V.M. Litvinov, Effect of temperature and annealing on the phase composition, molecular mobility, and the thickness of domains in isotactic polypropylene studied by proton solid-state NMR, SAXS, and DSC, *Macromolecules* 3977, 40, 2007.
136. Q. Zia, D. Mileva, R. Androsch, The rigid amorphous fraction in isotactic polypropylene, *Macromolecules* 8095, 41, 2008.
137. Q. Zia, H.-J. Radusch, R. Androsch, Direct analysis of annealing of nodular crystals in isotactic polypropylene by atomic force microscopy, and its correlation with calorimetric data, *Polymer* 3504, 48, 2007.
138. E.W. Fischer, Relations between colloidal structure of crystalline high polymers and their melting and recrystallization behavior, *Kolloid Z. Z. Polym.* 458, 231, 1969.
139. B. Crist, Equilibrium aspects of folded chain polymer crystals, *Macromolecules* 1971, 39, 2006.
140. R. Androsch, B. Wunderlich, Heat of fusion of the local equilibrium of melting of isotactic polypropylene, *Macromolecules* 8384, 34, 2001.
141. R. Androsch, B. Wunderlich, Specific reversible melting of polymer, *J. Polym. Sci. Polym. Phys.* 2039, 41, 2003.
142. R. Androsch, B. Wunderlich, A study of annealing of poly(ethylene-co-octene) by temperature-modulated and standard differential scanning calorimetry, *Macromolecules* 7238, 32, 1999.
143. H.S. Bu, S.Z.D. Cheng, B. Wunderlich, Addendum to the thermal properties of polypropylene, *Makromol. Chemie Rapid Commun.* 75, 9, 1988.
144. B. Wunderlich, *Macromolecular physics: Crystal melting*, Vol. 3, Academic Press, New York, 1980.
145. S.Z.D. Cheng, J.J. Janimak, A. Zhang, H.N. Cheng, Regime transitions in fractions of isotactic polypropylene, *Macromolecules* 298, 23, 1990.
146. H. Suzuki, J. Grebowicz, B. Wunderlich, Glass transition of poly(oxymethylene), *Brit. Pol. J.* 1, 17, 1985.
147. B.B. Sauer, B. Hsiao, Effect of the heterogeneous distribution of lamellar stacks on amorphous relaxations in semicrystalline polymers, *Polymer* 2553, 36, 1995.

148. H. Chen, P. Cebe, Investigation of the rigid amorphous fraction in nylon 6, *J. Therm. Anal. Cal.* 417, 89, 2007.
149. E. Donth, *The glass transition, relaxation dynamics in liquids and disordered materials*, Vol. 48, Springer, Berlin, 2001.
150. J.C. Duncan, J.G. Velde, R.E. Wetton, Comparison of glass transitions determined by DMTA and DSC, *Kautschuk und Gummi Kunststoffe* 768, 44, 1991.
151. M. Pluta, M. Kryszewski, Studies of  $\alpha$ -relaxation process in spherulitic and non-spherulitic samples of isotactic polypropylene with different molecular ordering, *Acta Polymerica* 42, 38, 1987.
152. R.H. Boyd, The modulus of the amorphous component in polyethylene, *Polym. Engg. Sci.* 1010, 19, 1979.
153. D. Schaeffer, H.W. Spiess, U.V. Suter, W.W. Flemming, Two-dimensional solid-state NMR studies of ultraslow chain motion: Glass transition in atactic polypropylene versus helical jumps in isotactic polypropylene, *Macromolecules* 3431, 23, 1990.
154. J.A. Sauer, R.A. Wall, N. Fuschillo, A.E. Woodward, Segmental motion in polypropylene, *J. Appl. Phys.* 1385, 29, 1958.
155. H.A. Flocke, Mechanisches Relaxationsverhalten von Polyäthylen, Polypropylen und Mischpolymerisaten, *Kolloid Z. Z. Polym.* 118, 180, 1962.
156. N.G. McCrum, Density-independent relaxations in polypropylene, *J. Polym. Sci. Polym. Lett.* 495, 2, 1964.
157. Q. Zia, H.-J. Radusch, R. Androsch, Deformation behavior of isotactic polypropylene crystallized via a mesophase, *J. Appl. Polym. Sci.* 755, 63, 2009.
158. M. Aboulfaraj, C. G'Sell, B. Ulrich, A. Dahoun, In situ observation of the plastic deformation of polypropylene spherulites under uniaxial tension and simple shear in the scanning electron microscope, *Polymer* 731, 36, 1995.
159. A. Peterlin, Molecular model of drawing polyethylene and polypropylene, *J. Mat. Sci.* 490, 6, 1971.
160. P.J. Flory, D.Y. Yoon, Molecular morphology in semicrystalline polymers, *Nature* 226, 272, 1978.
161. Y. Song, K. Nitta, N. Nemoto, Deformation mechanisms of polymer thin films by simultaneous kinetic measurement of microscopic infrared dichroism and

- macroscopic stress. 2. Molecular orientation during necking process of isotactic polypropylene, *Macromolecules* 1955, 36, 2003.
162. G. Parthasarthy, M. Sevegney, R.M. Kannan, Rheo-optical Fourier transform infrared spectroscopy of the deformation behavior in quenched and slow-cooled isotactic polypropylene films, *J. Polym. Sci. Polym. Phys.* 2539, 40, 2002.
  163. R. Russo, V. Vittoria, Deformation of intrinsic birefringence of smectic phase in isotactic polypropylene, *J. Appl. Polym. Sci.* 955, 60, 1996.
  164. I.M. Ward, D.W. Hadley, *An introduction to the mechanical properties of solid polymers*, Chichester, United Kingdom, 1993.
  165. A.J. Peacock, L. Mandelkern, The mechanical properties of random copolymers of ethylene: Force-elongation relations, *J. Polym. Sci. Polym. Phys.* 1917, 28, 1990.
  166. W.J. O'kane, R.J. Young, A.J. Ryan, The effect of annealing on the structure and properties of isotactic polypropylene films, *J. Macromol. Sci. Phys.* 427, 34, 1995.
  167. S. McGee, R.L. McCullough, Combining rules for predicting the thermoelastic properties of particulate filled polymers, polyblends, and foams, *Polym. Comp.* 149, 2, 1981.
  168. J.T. Seitz, The estimation of mechanical properties of polymer from molecular structure, *J. Appl. Polym. Sci.* 1331, 49, 1993.
  169. Q. Zia, R. Androsch, H.-J. Radusch, Effect of structure at the micrometer and nanometer scale on the light transmission of isotactic polypropylene, *J. Appl. Polym. Sci.* submitted, 2009.
  170. D. Mileva, R. Androsch, H.-J. Radusch, Effect of structure on light transmission in isotactic polypropylene and random propylene-1-butene copolymers, *Polym. Bull.* 561, 62, 2009.
  171. T.T. Wang, H.S. Chen, T.K. Kwei, A tough and transparent polyethylene, *J. Polym. Sci. Polym. Lett.* 505, 8, 1970.
  172. R. Stein, R. Prud'homme, Origin of polyethylene transparency, *J. Polym. Sci. Polym. Lett.* 595, 9, 1971.
  173. M. Shibayama, K.I. Imamura, K. Katoh, S. Nomura, Transparency of recycled polypropylene films, *J. Appl. Polym. Sci.* 1451, 42, 1991.

## **Declaration**

I hereby solemnly declare that the submitted dissertation is completed by myself and no other. All the sources of information have been duly identified and referenced.

Halle (Saale), on 23.07.2009

Qamer Zia

## Curriculum Vitae

### Personal information

*Name* Qamer Zia  
*Birth* 10.12.1978 in Dera Ghazi Khan–Pakistan  
*Marital Status* Married with Naheed Bashir since 2004  
Daughter Aliya Qamer (born on 29.04.2009)

### Academic profile

1983–1997 *Elementary and college education*

1998–2002 *B.Sc. Metallurgical Engineering and Materials Science  
University of Engineering and Technology, Lahore–Pakistan*

2003–2005 *M.Sc. in Applied Polymer Science  
Martin-Luther University, Halle-Wittenberg–Germany*

2005–2009 *Ph.D. at Centre of Engineering Sciences  
Martin-Luther University, Halle-Wittenberg–Germany  
Title: Structure, morphology, thermodynamic stability and  
properties of isotactic polypropylene with nodular nano-domains*

### Publications in journals

1. *Effect of atomic force microscopy (AFM) tip geometry on the evaluation of the crystal size of semicrystalline polymers*  
Qamer Zia and René Androsch  
*Measurement Science and Technology*, 097003, 20, 2009
2. *Deformation behavior of isotactic polypropylene crystallized via a mesophase*  
Qamer Zia, Hans-Joachim Radusch and René Androsch  
*Journal of Applied Polymer Science*, 755, 63, 2009
3. *Effect of structure at the micrometer and nanometer scale on the light transmission of isotactic polypropylene*  
Qamer Zia, René Androsch and Hans-Joachim Radusch  
*Journal of Applied Polymer Science*, in print–2009
4. *Crystal morphology of rapidly cooled isotactic polypropylene: A comparative study by TEM and AFM*  
Qamer Zia, René Androsch, Hans-Joachim Radusch and Elisabeth Ingolič  
*Polymer Bulletin*, 791, 60, 2008

5. *The rigid amorphous fraction in isotactic polypropylene*  
Qamer Zia, Daniela Mileva and René Androsch  
*Macromolecules*, 8095, 41, 2008
6. *Direct analysis of annealing of nodular crystals in isotactic polypropylene by atomic force microscopy and its correlation with calorimetric data*  
Qamer Zia, René Androsch and Hans-Joachim Radsch  
*Polymer*, 48, 3504, 2007
7. *Morphology, reorganization and stability of mesomorphic nanocrystals in iPP*  
Qamer Zia, René Androsch, Hans-Joachim Radsch and Stefano Piccarolo  
*Polymer*, 47, 8163, 2006

### **Conference talks**

1. *Imaging of polymer crystals using standard and high-resolution AFM-tips*  
Qamer Zia, René Androsch, Hans-Joachim Radsch and Elisabeth Ingolič  
*Euro AFM Forum*, July–2009, Munich–Germany
2. *Effect of crystal morphology on tensile-stress strain behavior of isotactic polypropylene*  
Qamer Zia, René Androsch and Hans-Joachim Radsch  
*12. Problemseminar: Deformation und Bruchverhalten von Kunststoffen, Book of abstracts*, Juni–2009, Merseburg–Germany
3. *Structure-property relation in isotactic polypropylene with non-lamellar crystals*  
Qamer Zia, René Androsch and Hans-Joachim Radsch  
*24<sup>th</sup> Annual PPS meeting, Book of abstracts p.II-178*, June–2008, Salerno–Italy
4. *Structure, morphology and reorganization of nanocrystals in isotactic polypropylene*  
Qamer Zia, René Androsch and Hans-Joachim Radsch  
*23<sup>rd</sup> Annual PPS meeting, Book of abstracts p.89*, May–2007, Salvador–Brazil
5. *Transition from mesomorphic nodular nano-crystals to monoclinic lamellae in iPP*  
Qamer Zia, René Androsch, Stefano Piccarolo and Hans-Joachim Radsch  
*Polymerwerkstoffe, SL-C4 Book of abstracts p.80*, September–2006, Halle–Germany
6. *Tailoring the morphology and stability of nano-crystals in iPP by the condition of primary melt-crystallization and subsequent annealing at elevated temperature*  
Qamer Zia, René Androsch, Hans-Joachim Radsch and Stefano Piccarolo  
*Proceedings NATAS*, August–2006, Kentucky–United States